THÈSE

présentée à

L'UNIVERSITÉ PAUL SABATIER

en vue de l'obtention du

DOCTORAT DE L'UNIVERSITÉ PAUL SABATIER DE TOULOUSE

Spécialité Instrumentation Astrophysique

par

Antje Kohnle

A GAMMA-RAY LENS FOR NUCLEAR ASTROPHYSICS

UN TÉLESCOPE À LENTILLE DE LAUE POUR L'ASTROPHYSIQUE NUCLÉAIRE

Soutenue le 2 juin 1998 devant le jury composé de :

G. VEDRENNE	Professeur à l'UPS, Toulouse	Président
P. BASTIE	Directeur de Recherche, Lab. de Spectrométrie Physique	Rapporteur
P. SIFFERT	Directeur de Recherche, Lab. PHASE	Rapporteur
G. SKINNER	Directeur de Recherche, Univ. of Birmingham	Rapporteur
M. JOUBERT	Ingenieur au CNES, Toulouse	Examinatrice
J.-P. ROQUES	Chargé de Recherche, CESR Toulouse	Examinateur
R. SMITHER	Directeur de Recherche, Argonne National Lab.	Examinateur
P. VON BALLMOOS	Professeur à l'UPS, Toulouse	Examinateur

Résumé

Cette thèse est consacrée à un télescope à lentille de Laue, un nouveau type d'instrument d'observation pour l'astronomie gamma spatiale dans le domaine d'énergie du keV au MeV.

Le travail présenté dans cette thèse se compose de trois parties. Dans la première, la théorie de diffraction des cristaux mosaïques est utilisée pour optimiser la configuration du télescope et simuler la performance d'une lentille de Laue dans l'espace. Le potentiel scientifique de cet instrument est discuté dans le cadre de ces simulations. Une sensibilité de $2 \cdot 10^{-7}$ ph/(cm^2 s) à $1 \cdot 10^{-6}$ ph/(cm^2 s) pour des raies fines semble possible avec une lentille de taille moderée, rendant cet instrument précieux pour la détection des raies gamma provenant de la radioactivité et de l'annihilation de particules. La cartographie de l'intensité des sources faiblement étendues est possible grâce à une résolution angulaire encore jamais atteinte de moins d'une minute d'arc.

Dans la deuxieme partie, un anneau d'un prototype de lentille réglable a été réalisé en utilisant des picomoteurs et des capteurs pour orienter les cristaux avec une précision inférieure à la seconde d'arc. La capacité de cet anneau pour focaliser une gamme en énergie a été montrée en changeant l'orientation des cristaux pour focaliser des raies à 276, 303, 356, 383, et 662 keV venant d'une source de ^{137}Cs et d'une source de ^{133}Ba. La stabilité de la calibration des capteurs ainsi que la stabilité du système ont également été démontrées.

Dans la troisième partie, les efficacités de diffraction de cristaux avec une mosaïcité de quelques secondes d'arc ont été mesurées de 200 keV à 500 keV en utilisant le rayonnement synchrotron. A une énergie fixée, l'efficacité maximale et l'efficacité intégrale ont été mesurées pour une grande gamme de mosaïcité. Les résultats sont en bon accord avec le modèle de Darwin utilisé dans les simulations du télescope.

Abstract

This thesis is concerned with a focusing crystal lens telescope, a novel type of telescope for space-based gamma-ray astronomy working in the keV to MeV energy range.

The work presented in this thesis can be divided into three parts. In the first part, the theory of diffraction of mosaic crystals is used to optimize the crystal lens design and to simulate the performance of a crystal lens telescope in space. Based on these calculations, the scientific potential of such an instrument is discussed. Narrow line sensitivities of $2 \cdot 10^{-7}$ ph/(cm^2 s) to $1 \cdot 10^{-6}$ ph/(cm^2 s) over the energy range of 200 keV to 1300 keV seem achievable with a lens of moderate size, making the instrument a valuable tool for the detection of gamma-ray lines from radioactivity and annihilation radiation. The unprecedented angular resolution of less than one arc minute enables the intensity mapping of slightly-extended sources.

In the second part, one ring of a prototype tunable lens was realized using picomotors and non-contact eddy-current sensors to orient crystals with sub arc second precision. The capability to focus a range of energies was demonstrated by changing the orientation of all the crystals to focus gamma-ray lines at 276, 303, 356, 383, and 662 keV using a ^{137}Cs and a ^{133}Ba source. The stability of the sensor calibration and the system stability were verified.

In the third part, diffraction efficiencies of crystals with a mosaic width of a few arc seconds were measured at energies ranging from 200 keV to 500 keV using synchrotron radiation. At fixed energy, the peak and the integral efficiency were measured over a large range of mosaic width. The results were compared with the Darwin model used in the simulations of the crystal lens telescope, and were in reaonably good agreement with the model.

Contents

1 Introduction **11**
1.1 Outline of the Thesis . . . 14

2 Gamma-Ray Line Astronomy **15**
2.1 Potential of Gamma-Ray Line Astronomy . . . 15
2.2 Annihilation Radiation . . . 15
2.3 Gamma-Ray Lines from Radioactive Decays . . . 16
2.4 Gamma-Ray Lines from Nuclear Deexcitation . . . 16
2.5 Neutron Capture Reactions . . . 16
2.6 Cyclotron Lines . . . 17
2.7 Overview of Gamma-Ray Line Observations . . . 18

3 Instrumentation in Hard X-Ray and Gamma-Ray Astronomy **23**
3.1 Grazing Incidence Telescopes . . . 23
3.2 Hard X-ray Telescopes . . . 24
3.3 Coded Aperture Telescopes . . . 25
3.4 Compton Telescopes . . . 28
3.5 High Energy Gamma-Ray Detectors . . . 30

4 A Crystal Lens Telescope **31**
4.1 Crystal Structure, the Bragg Relation . . . 31
4.2 Functioning Principle, Characteristics . . . 33
4.3 Design Considerations . . . 34
4.3.1 Perfect vs. Mosaic Crystals: The Darwin Mosaic Model . . . 34
4.3.2 Crystal Material . . . 38
4.3.3 Mosaic Width and Energy Bandwidth . . . 40
4.3.4 Crystal Thickness and Working Energy Range . . . 43
4.3.5 Number of Crystal Rings . . . 44
4.3.6 Detector Design . . . 46
4.4 Description of the Ground-Based Prototype, Test Results . . . 47
4.5 Imaging Properties, Calculation of the Telescope Performance . . . 51
4.5.1 Off-Axis and Off-Energy Efficiency . . . 51
4.5.2 Response to Extended Emission . . . 52
4.5.3 Angular Resolution . . . 54
4.5.4 Focal Plane Image . . . 55
4.5.5 Calculation of the Line Sensitivity . . . 58
4.6 Broadband Concentrators . . . 58

5 Potential of a Crystal Lens Telescope **61**
5.1 Sensitivity . . . 61

5.2 Imaging . . . 65
5.3 Spectroscopy . . . 68
5.4 Polarimetry . . . 68

6 Simulations of a Spaceborne Crystal Lens Telescope 71
6.1 A Balloon-Borne Crystal Lens Telescope . . . 71
6.1.1 Configuration . . . 71
6.1.2 Candidate Sources . . . 72
6.1.3 Simulation of the Observation of the Crab Nebula and Pulsar . . . 73
6.1.4 Simulation of the Observation of 1E1740-294 at 511 keV . . . 78
6.2 A Satellite-Based Crystal Lens Telescope . . . 81
6.2.1 Comparison Criteria . . . 81
6.2.2 Comparison of Possible Configurations . . . 81

7 Realization of One Ring of a Prototype Tunable Crystal Lens 87
7.1 Range and Resolution Requirements . . . 87
7.2 Picomotor and Eddy-Current Sensor Performance Tests with Autocollimation . . . 89
7.3 Buildup of the Tunable Crystal Lens . . . 92
7.4 Test Setup . . . 95
7.5 Description of Scans . . . 98
7.6 Alignment of the Source, Lens and Detector . . . 98
7.7 Tuning the Lens to the First Energy . . . 98
7.8 Calibration of the Sensors and Picomotors . . . 99
7.9 Crystal Plate Tests . . . 100
7.10 Measurements and Results . . . 102
7.11 Conclusions . . . 106

8 Measurement of Crystal Diffraction Efficiencies using Synchrotron Radiation 109
8.1 Introduction . . . 109
8.2 Experimental Setup . . . 110
8.3 Diffraction Efficiency Measurement . . . 112
8.3.1 Ge (111) and Ge (220) . . . 113
8.3.2 Ge (333) and Ge (440) . . . 115
8.3.3 Dependence of the Diffraction Efficiency on the Mosaic Width . . . 117
8.3.4 Effect of Surface Damage on the Diffraction Efficiency . . . 119
8.3.5 Increase of the Diffraction Efficiency for a Source at Finite Distance due to Crystal Wedging . . . 120
8.4 Conclusions . . . 122

9 Summary 125
9.1 Simulations of the Performance of a Crystal Lens Telescope . . . 125
9.2 Realization of One Ring of a Prototype Tunable Lens . . . 126

9.3 Diffraction Efficiency Measurements 128

10 Bibliography **131**

11 Acknowledgements **137**

1 Introduction

This thesis is concerned with a novel type of telescope for space-based gamma-ray astronomy, working in the keV to MeV energy range.

At these energies, the atmosphere is opaque to gamma-rays. At 100 keV, the absorption coefficient in air is μ=0.15 cm^2/g, meaning that the detector needs be transported to a height of $\mu x/\cos(z) < 1$ or $x < 4.5$ g/cm^2, which corresponds to about 40 km. Here, z is the mean zenith angle of the observation, and was set to 45 degrees. Thus, detectors need to be flown on balloons or on satellites.

Typical gamma-ray fluxes in this energy region are low: the strongest steady source, the Crab, has a flux of $4.5 \cdot 10^{-4}$ photons cm^{-2} s^{-1} keV^{-1} at 100 keV and a flux of $3.1 \cdot 10^{-6}$ photons cm^{-2} s^{-1} keV^{-1} at 1000 keV. For a typical effective gamma-ray detection area of 500 cm^2 for a satellite-based detector, this implies a detected flux of 0.25 photons s^{-1} keV^{-1} at 100 keV, and a detected flux of 0.0016 photons s^{-1} keV^{-1} at 1000 keV.

The problem of few source counts is aggravated by a high background consisting of photons and charged particles within the angular acceptance of the instrument and penetrating the anticoincidence shield, as well as secondary radioactivity induced by charged particles reacting with the detector and the surrounding material. For a detector with 500 cm^2 effective area for gamma-rays, a typical background rate would be 0.5 counts s^{-1} keV^{-1}. Thus, the signal-to-noise ratio for the observation of the Crab decreases from about 0.5 at 100 keV to 0.003 at 1000 keV. Typical continuum sensitivities for a 10^6 s observation time lie in the few milli-Crab region. With this sensitivity, only a handful of persistant sources can be detected.

In order to increase the sensitivity, one could try to increase the effective detection area for gamma-rays by making the detector more efficient or larger, but this is generally not possible due to weight constraints. One could try to reduce the number of background counts seen in the detector by optimizing the shielding and the anticoincidence system as well as the detector material. Much progress has been made in reducing background in the last years, but there are intrinsic limits to the background reduction due to the flux passing through the aperture of the instrument and the necessity to have material surrounding the detector.

The instrument described in this thesis, a focusing crystal lens telescope, tries to overcome the sensitivity impasse by drastically reducing the effective background volume by concentrating the gamma-rays onto a small detector.

How does one concentrate gamma-rays? In radio telescopes, the incoming waves are focused using a spherical mirror. In the optical domain, convex lenses as well as focusing mirrors are used. In the X-ray region, focusing telescopes are built using grazing incidence mirrors. These are based on the total reflection of X-rays below some critical angle due to the index of refraction in air being less than unity.

For gamma-rays, Bragg reflection on crystals can be used to concentrate incoming photons. An incident photon with wavelength λ and making an angle θ with the crystalline planes is deflected by an angle of 2θ if the Bragg relation $2dsin\theta = n\lambda$ holds. Here, d is the crystalline plane spacing and n is an integer. The deflection of 2θ can be used to concentrate gamma-rays. By arranging crystals in a ringlike pattern, a common focus point can be achieved for many crystals, making a

large gamma-ray detection area possible.

There are however some differences between a "crystal lens" for gamma-rays and a lens for optical photons: the Bragg relation is essentially monochromatic, meaning that a single crystal will only focus a narrow band of energies. Broad bandpass concentrators can be conceived, where the lens consists of many crystals each oriented to focus a slightly different energy. This however leads to only a fraction of the lens area being efficient at any one energy, and thus compromises the dramatic increase of the signal-to-noise ratio and the sensitivity which is the major advantage of such an instrument. The instrument described in this thesis orients all crystals to focus the same energy. This limits the energy bandpass of the instrument, but maximizes the sensitivity. Increases in sensitivity of a factor of 100 compared with existing gamma-ray instruments and a factor of 10 compared with next-generation detectors seem possible.

The Bragg reflections for perfect crystals are very narrow, which would lead to an extremely narrow energy bandpass. The energy bandpass can be increased using so-called mosaic crystals, which are characterized by the mosaic width. The diffracted flux increases with increasing mosaic width of the crystal. The mosaic width of the crystals govern the flux throughput, the angular resolution and the energy bandpass of the crystal lens.

A crystal lens telescope consists of the crystal lens made up of several hundred crystals, and a detector in the focal plane. Characteristics of a crystal lens telescope are an angular resolution of 10 to 20 arc seconds, an effective gamma-ray detection area of 200 to 1000 cm^2, a background-inducing volume of 100 cm^3, an energy bandpass for on-axis gamma-rays of 3 to 8 keV at 500 keV increasing to 20 to 54 keV at 1300 keV. The working energy range would be 200 keV to 1300 keV, extending the energy range up to 2300 keV may be possible. The field-of-view is in principle only limited by the detector size, but the efficiency of the lens decreases quickly with off-axis angle. In practice, this limits the field of view to less than 1 arc minute. Sensitivities of several 10^{-7} photons cm^{-2} s^{-1} over the energy bandpass of the instrument seem achievable.

In summary, a crystal lens telescope achieves an unprecedented sensitivity and an unprecedented angular resolution, but only in both a limited field of view and a limited energy window. Is there a scientific potential for such an instrument?

The limited field of view implies the observation of point sources or sources with less than a few degree extent. It is perhaps noteworthy that small fields of view are commonplace in radio, optical, and X-ray astronomy. CCD images typically comprise a field of less than 1 arc minute, and X-ray Wolter telescopes have fields of view of less than one degree. Even though the energy bandpass of the instrument is only a few keV to 50 keV, it is important to note that the energy that the lens focuses can be changed, and that the instrument can be designed in a way that two or three energies are focused at the same time. Sweeps in energy can be performed. Furthermore, by slightly offsetting the crystal orientations from the nominal position, it is possible to increase the energy bandpass, however at the cost of peak efficiency. One of the aims of the work described in this thesis was to demonstrate that a "tunable" lens can be built, making it possible to change the energy that the lens focuses.

The narrow energy bandpass of the instrument is ideally suited to the observation of gamma-ray lines. Gamma-ray lines are produced by nuclear de-excitation, by electron-positron annihilation,

by radioactive decay, and by Landau transitions of electrons in strong $\vec{B}$ fields. Nuclear de-excitation lines have been observed in solar flares and in the Orion complex of giant molecular clouds. Cyclotron lines have been observed in the spectra of several pulsars, and perhaps in gamma-ray bursts. Electron-positron annihilation has been observed as diffuse emission arising from our Galaxy. Transient features interpreted as broad redshifted annihilation radiation have been reported from the X-ray nova Nova Musca and from the galactic microquasar 1E1740-294. Radioactive decay lines arising from explosive nucleosynthesis have been detected from the type II supernova SN 1987 A, from two young supernova remnants (Vela and Cas A), and perhaps from the type Ia supernova SN 1991 T.

The sensitivity of a crystal lens telescope to the ^{56}Co lines implies the capability of detection of about 3 supernovae type Ia per year, and of the detection of gamma-rays from 0.4 supernovae of type Ib/c per year. Gamma-rays from a type II supernova within the Local Group of galaxies could be detected, but such an event is improbable during a mission lifetime. As stated above, there has to date only been one marginal detection of gamma-ray lines from a type Ia supernova, namely the ^{56}Co lines seen by COMPTEL from SN 1991 T. ^{56}Co lines from type Ib/c supernovae have not yet been detected.

According to current nova models, a crystal lens telescope can see a CO-nova out to 2.0 to 2.7 kpc in the 478 keV line of the ^{7}Be decay, and a ONe-nova out to 1.6 to 2.0 kpc in the 1275 keV line of the ^{22}Na decay. This implies a detection of gamma-ray lines from 0.5 to 1.2 novae per year using the estimated Galactic nova rate of 35 yr^{-1}. Up to now, gamma-ray lines from novae have not been detected.

The 10 to 20 arc second angular resolution of a crystal lens telescope enables mapping of the ^{44}Ti emission seen in the young supernova remnant Cas A. By slightly "detuning" the lens crystals to increase the field-of-view, a mapping of the ^{26}Al emission from the Vela supernova remnant can be performed. A crystal lens telescope can clarify if the galactic microquasar 1E1740-294 is a source of annihilation radiation. In the case of a positive detection, an intensity mapping of the emission can be compared with the jets seen at radio wavelengths and the molecular cloud seen in the infrared.

The realization of a space-borne crystal lens telescope presents several technological challenges: it is necessary to individually motorize several hundred crystals with a precision of a few arc seconds over a range of 0.5° to 1.5° to be able to change the crystalline plane orientation to incoming photons. The stability of the crystal positioning is decisive for the crystal lens response, and thus an independent method for verifying the positioning is mandatory. Due to the fact that the Bragg angle is energy dependent, the focal length, i.e., the lens-detector distance, is different for each energy, and scales linearly with the energy that the crystal lens focuses. At keV to MeV energies, the Bragg angles are at most a few degrees, leading to very long focal lengths. For the laboratory prototype, the focal length is 8.3 m at 511 keV, and 21.1 m at 1300 keV. For a spaceborne instrument, focal lengths twice this long would be desirable. If the working energy range of the instrument were extended to include the 1809 keV line from radioactive ^{26}Al and the neutron capture line at 2223 keV, the focal length would need to be even longer.

Finally, it is important to note that though achieving a major breakthrough in sensitivity, the

gamma-ray detection area for such an instrument is similar to existing and next-generation instruments. Thus, the total number of source counts is small, with typically several hundred photons comprising the 3σ detection at the sensitivity limit. The intensity measurement is limited by the number of source photons. Increasing the number of detected photons would imply an increase in detection area, which is difficult to realize within weight constraints of space-based astronomy.

1.1 Outline of the Thesis

This thesis is organized as follows. As the main scientific objective of the crystal lens telescope is the observation of gamma-ray lines, Chapter 2 gives a brief summary of gamma-ray line astronomy, summarizing the production mechanisms as well as the observational results. Chapter 3 tries to put the crystal lens telescope into the context of existing and next-generation gamma-ray instrumentation by summarizing detection techniques as well as existing and proposed telescopes. The functioning principle and general characteristics of a crystal lens telescope are described in Chapter 4. Design criteria of a crystal lens telescope are discussed in the context of the Darwin mosaic model. This chapter also summarized work on the crystal lens telescope prior to this thesis, namely the buildup of the first prototype crystal lens telescope realized in 1992 to 1995. Using the configuration of the prototype, the imaging properties of a crystal lens telescope are discussed. The scientific potential of a crystal lens telescope is outlined in Chapter 5, with emphasis on the sensitivity increase and the intensity mapping capabilities of such an instrument. Chapter 6 describes simulations of the performance of a spaceborne instrument. A balloon-flight observation of the Crab nebula and pulsar as well as the Galactic black hole candidate 1E1740-294 are simulated. The sensitivity of several configurations of a satellite-based crystal lens are compared. Chapter 7 describes the realisation of one ring of a prototype tunable crystal lens. Preliminary tests with the picomotors and non-contact sensors used to orient the crystals, the buildup of the lens, as well as the system tests are described. Chapter 8 describes measurements carried out at the Advanced Photon Source synchrotron at Argonne National Laboratory (Illinois, USA) to measure crystal diffraction efficiencies and other crystal characteristics. Finally, Chapter 9 summarizes the results of this thesis.

2 Gamma-Ray Line Astronomy

2.1 Potential of Gamma-Ray Line Astronomy

Gamma-ray lines are produced by e^+e^- annihilation, radioactive decay, inelastic collisions of energetic particles with ambient matter, neutron capture reactions, and by Landau transitions of electrons in strong fields. In this chapter, each of these production mechanisms is described. Also, the status of gamma-ray line observations is reviewed.

The detection of gamma-ray lines provides information on nucleosynthesis, compact objects, and particle acceleration. From the line intensity, isotopic abundances and nucleosynthesis yields can be derived. The line centroid provides information on the motion of the object (Doppler shift), on the compactness (gravitational redshift) and on the distance (cosmological redshift). The line width determines the variability of the magnetic field along the line of sight (cyclotron features), the velocity of ejecta (supernovae, novae), and the presence of dust (interaction of cosmic rays with the interstellar medium). Physical parameters of the emission region, such as density, optical thickness, and temperature, can be derived from the line profile. The spatial distribution of the line intensity can be used to determine the production sites (the galactic distribution of annihilation radiation and of radioactive ^{26}Al), and to test supernova and nova models. Finally, there is the temporal information: the intensity of cyclotron lines can vary with the rotation phase of the pulsar, the intensity of lines in supernova ejecta can deviate from the exponential decay law due to variations in the opacity of the ejecta.

The observation of the ^{56}Co lines from SN1987A led to revisions of supernova explosion models. The fact that the detection came 6 months earlier than expected as well as the line profiles as measured by various experiments can only be explained in terms of substantial mixing, fragmentation due to instabilities, and "clumpiness" of the envelope, i.e., regions of optically-thick and optically-thin material.

The detection of both ^{57}Co and ^{56}Co from SN1987A allowed a direct determination of the ratio of the abundances of the daughter isotopes ^{57}Fe/^{56}Fe, which can then be compared with the solar ratio.

The detection of cyclotron lines provides direct evidence for the high surface magnetic field of neutron stars, and is a direct measure of the field close to the surface.

2.2 Annihilation Radiation

Positron annihilation can occur either directly or via the formation of positronium, the bound state of an electron and a positron. Positronium is created by charge exchange with a gas atom or molecule, or by radiative recombination with free electrons. Due to the number of quantum states, the singlet state $^1S_0$ is created 25 % of the time, and the triplet state $^3S_1$ 75 % of the time. The singlet state decays via the production of two 511 keV gamma rays, whereas the triplet state decays via the emission of three gamma-rays, giving rise to a continuum between 0 and 511 keV.

The positronium fraction, i.e., the fraction of incident positrons that decay via the formation of positronium, can be determined from observational data by fitting the 511 keV line and the three-

photon continuum [1]. Both the line width and the positronium fraction depend on the annihilation environment, e.g. temperature, degree of ionisation, presence of dust, etc.
The positrons are created by the β^+-decays of unstable nuclei and by the decay of pions, $\pi^+ \longrightarrow \mu^+ + \nu_\mu$ and $\mu^+ \longrightarrow e^+ + \nu_e + \overline{\nu}_\mu$. Pions are created in proton-proton or nucleus-nucleus reactions, β^+-unstable nuclides are produced in supernova nucleosynthesis. The ^{44}Sc $\longrightarrow$ ^{44}Ca decay emitting a positron 95 % of the time, the ^{56}Co $\longrightarrow$ ^{56}Fe decay emitting a positron 19 % of the time, as well as the ^{26}Al $\longrightarrow$ ^{26}Mg decay emitting a positron 82 % of the time, could provide prodigious amounts of positrons [17]. The detection of the 1809 keV gamma-ray line from the ^{26}Al $\longrightarrow$ ^{26}Mg decay by COMPTEL is direct evidence for the production of positrons.

2.3 Gamma-Ray Lines from Radioactive Decays

The detection of gamma-ray lines from radioactivity is related to the question of the origin of the elements and the isotopic abundances.
Large yields of heavy elements are expected from regions of high pressure and high density, such as the interiors of evolved stars. In novae and supernovae explosions, it is possible to directly see the result of explosive nuclear burning via the detection of gamma-ray lines from short-lived isotopes. Table 1 lists important gamma-ray lines resulting from radioactive decays. For novae and supernovae production sites, the gamma-ray line radiation is only observable if the decay lifetime is long enough for the expanding envelope to become optically thin to gamma-rays.

2.4 Gamma-Ray Lines from Nuclear Deexcitation

The interaction of energetic nuclei with ambient matter can lead to gamma-ray line emission from excited nuclei.
Inelastic collisions of cosmic rays with the interstellar medium can produce narrow or broadened lines. Broad lines are produced by accelerated C and heavier nuclei interacting with ambient H and He. Narrow lines are produced by accelerated protons and α-particles interacting with ambient He and heavier nuclei. Very narrow lines result from excited nuclei which have come to rest before emitting gamma-rays, e.g. deexcitation of heavy nuclei embedded in dust grains.
In solar flares, inelastic collisions of accelerated protons and heavier nuclei interacting with the solar atmosphere can lead to gamma-ray line emission.

2.5 Neutron Capture Reactions

Thermal neutron capture is important in high-density environments such as in solar flares or accretion disks, where collisions are numerous enough to thermalize neutrons before they decay via $n \longrightarrow p + e^- + \overline{\nu}_e$. The neutrons are created in high-energy proton-nucleus collisions. Neutron capture by a proton leads to the formation of deuteron $n + p \longrightarrow^2_1 D + \gamma$. The emitted gamma-ray has the binding energy of the deuteron, 2.223 MeV. In accretion disks, the reaction $^{57}Fe + n \longrightarrow^{57} Fe^*$ may be important, leading to the emission of gamma-rays with energies of 7.632 and 7.646 MeV [3].

Decay Chain	Chain Lifetime τ (year)	Line Energies (keV)	Site
^{7}Be $\rightarrow$ ^{7}Li	0.21	478	Novae
^{56}Ni $\rightarrow$ ^{56}Co $\rightarrow$ ^{56}Fe	0.31	847 (1.), 1238 (0.685) 2598 (0.17) 1771 (0.45)	SN (SN1987A, SN1991T)
^{57}Co $\rightarrow$ ^{57}Fe	1.1	122 (0.86) 136 (0.11)	SN (SN1987A)
^{22}Na $\rightarrow$ ^{22}Ne	3.8	1275 (1.)	Novae
^{44}Ti $\rightarrow$ ^{44}Sc $\rightarrow$ ^{44}Ca	59	1156 (1.) 68 (1.) 78 (0.98)	SN (Cas A)
^{26}Al $\rightarrow$ ^{26}Mg	$1.1 \cdot 10^{6}$	1809 (1.)	WR, AGB, Novae, SN (Galaxy, Vela, Carina, Cygnus)
^{60}Fe $\rightarrow$ ^{60}Co $\rightarrow$ ^{60}Ni	$2.2 \cdot 10^{6}$	1332 (1.) 1173 (1.)	SN

Table 1: *The most important cosmic radioactivities for gamma-ray lines from nucleosynthesis are listed, along with the the corresponding lifetimes, energies, branching ratios, and astrophysical production sites (adapted from [2]). For double decay chains, the longest lifetime is given. The gamma-ray line energies that have been detected are underlined. The branching ratio is given in parenthesis. The production sites are supernovae (SN), asymptotic giant branch stars (AGB), Wolf-Rayet stars (WR), and novae. The objects from which the lines have been detected are in parenthesis.*

2.6 Cyclotron Lines

Cyclotron lines are the result of transitions between Landau levels, the quantized energy levels of electrons in strong magnetic fields. Assuming a "freezing" of the magnetic flux during the formation of a neutron star, i.e. $BR^2 = const.$ with B as the surface magnetic field strength and R as the star radius, the magnetic field strength of a neutron star should be of the order of 10^{12} G or 10^{8} T. For such a strong field, the quantized energy states, called Landau levels, are

$$E_n = mc^2 \left(1 + [2n+1]\,\frac{h\omega_B}{mc^2}\right)^{1/2} \tag{1}$$

with n=0,1,2,..., mc^2 as the electron rest mass, and $\omega_B = \frac{eB}{mc}$ as the Balmer frequency. Assuming $h\omega_B \ll mc^2$, the energy separation between adjacent energy states is

$$E_{n+1} - E_n = \frac{heB}{mc} \approx 11.6 B_{12} \quad \text{[keV]} \tag{2}$$

with B_{12} as the magnetic field strength in units of 10^{12} G. Thus, the observation of cyclotron resonance features in the spectra of X-ray binaries containing a neutron star is a direct measure

of the magnetic field close to the neutron star surface. The detection of both the first and second harmonic could in principle be used to deduce both the gravitational redshift of the line-forming region and the magnetic field.

2.7 Overview of Gamma-Ray Line Observations

Annihilation radiation from Discrete Sources

A number of transient features from discrete sources suggestive of pair annihilation radiation have been reported: During the October 13 1990 observation of the black hole candidate 1E 1740-294, the SIGMA telescope aboard the GRANAT spacecraft observed an excess in the 300 to 700 keV range. The feature was modeled as a Gaussian centered at 480 keV with a FWHM of 240 keV, with 50 % of the source energy between 35 keV and 1 MeV emitted in this feature [4]. The feature can be interpreted as broadened and redshifted pair annihilation radiation coming from a hot ($\approx 5 \cdot 10^8$ K) plasma. In an observation performed the day after, this feature was absent, showing that the source had recovered its nominal state within 18 to 70 h.

A similar, weaker emission feature was seen by SIGMA on September 19-20 1992, being fit by a Gaussian with a centroid of 350^{+110}_{-40} keV, a line width of 170^{+210}_{-65} keV, and a line flux of $4.28^{+2.7}_{-1.5} \cdot 10^{-3}$ photons cm^{-2} s^{-1} [7]. However, simultaneous observations of the source with the OSSE instrument aboard the CGRO satellite do not confirm the September 1992 outburst, and set an upper limit (3σ) of $\approx 2.4 \cdot 10^{-3}$ photons cm^{-2} s^{-1} [5].

Evidence for a line around 170 keV, the backscatter energy of 511 keV photons, from the direction of the Galactic center was obtained by HEXAGONE, a balloon-borne high-resolution germanium spectrometer with an 18° field of view, during a flight in May 1989 [6]. Besides a positron annihilation line with a flux of $10.0 \pm 2.4 \cdot 10^{-4}$ photons cm^{-2} s^{-1} and a FWHM of $2.9^{+1.0}_{-1.1}$ keV, the spectrum showed a peak centered at 163.7 ± 3.4 keV with a flux of $1.55 \pm 0.47 \cdot 10^{-3}$ photons cm^{-2} s^{-1} and a FWHM of 24.4 ± 9.2 keV. The 164 keV feature can be interpreted as Compton backscatter of broadened and redshifted annihilation radiation, possibly from the source 1E1740-294.

Sigma/GRANAT soft gamma-ray observations of the X-ray nova in Musca led to the discovery of an emission feature around 500 keV in one 13 h spectrum taken 10 days after the flare [8]. The feature can be fitted by a Gaussian with a line flux of $6.01^{+2.95}_{-2.76} \cdot 10^{-3}$ photons cm^{-2} s^{-1}, a line centroid of 481 ± 22 keV, and a line width compatible with the intrinsic detector resolution. There is also some evidence for an excess of $\approx 1.8 \cdot 10^{-3}$ photons cm^{-2} s^{-1} around 200 keV, which could be due to backscattering of 511 keV photons in the source.

The French-Italian FIGARO balloon-borne NaI instrument observed the Crab pulsar and Nebula in 1986 and in 1990. The combined observation led to the detection of a 3.5 σ excess in the 430 to 480 energy bins of the pulsar's second peak [9]. The excess was centered at 440±10 keV with a FWHM of 59 keV, compatible with the instrument resolution. The feature can be interpreted as a gravitationally redshifted annihilation line.

Annihilation radiation from the Galactic Center region

The first evidence for annihilation radiation coming from the Galactic center region was in the early 1970s from a group at Rice University [11] [12]. Using a balloon-borne NaI spectrometer with a 24° field of view, a line with an energy of 476 ± 24 keV and a line flux of $1.8 \pm 0.5 \cdot 10^{-3}$

photons cm^{-2} s^{-1} was reported. The significance of the feature combined for two flights was 5.3 σ. Two years later, the line was again detected with a 3.5 σ significance, a line energy of 530±11 keV, and a line flux of $8.0 \pm 2.3 \cdot 10^{-4}$ photons cm^{-2} s^{-1} [13]. With a balloon-borne germanium detector, the annihilation line energy was precisely determined by Leventhal et al. to be 510.7±0.5 keV with a line width compatible with the detector resolution and a flux of $1.22 \cdot 10^{-3}$ photons cm^{-2} s^{-1} [14]. Since then, numerous balloon-borne and satellite experiments have observed a 511 keV line flux from the direction of the galactic center. These results are reviewed in Teegarden 1995 [15]. The comparison of the different experiments is complicated by the differing fields of view, but evidence for time-variability of the line by as much as $2 \cdot 10^{-3}$ photons cm^{-2} s^{-1} as well as a correlation of the flux with the field of view was found. These results could be interpreted as the emission being due to a time-variable compact source and a steady-state diffuse galactic component [16].

The galactic longitude distribution of the 511 keV annihilation radiation and the 3-photon positronium continuum have recently been measured with OSSE [10]. The profiles are well represented by an $\approx 11°$ FWHM Gaussian central bulge together with a possible broad disk component comprising as much as 15 % of the integral flux between 40° and 320° longitude. Contributions from one or more discrete sources at or near the center with total annihilation radiation (line plus continuum) intensities of up to $\approx 4 \cdot 10^{-4}$ photons cm^{-2} s^{-1} (2 σ upper limit) are compatible with the observed distribution. The best estimate of the positronium fraction is 0.97 ± 0.03.

Purcell et al. produced a 511 keV sky map combining data from OSSE, TGRS and SMM [17]. The sky map shows evidence for three distinct features: a central bulge with a flux of $3.3 \cdot 10^{-4}$ photons cm^{-2} s^{-1} and a size of 4° FWHM, emission in the Galactic plane with a flux of 10^{-3} photons cm^{-2} s^{-1}, a latitude extent of 12° and a longitude extent of 30°, and an enhancement or extension of emission at positive latitudes above the Galactic center with a flux of $9 \cdot 10^{-4}$ photons cm^{-2} s^{-1}. No evidence for time variability of the 511 keV flux is found, in contradiction with earlier measurements. A supernova origin of the positrons may explain both the intensity (corresponding to a production rate of $3.3 \pm 0.5 \cdot 10^{43}$ positrons s^{-1}) and the morphology of the 511 keV flux.

Gamma-Ray lines from radioactivity

The appearance of the type II supernova SN1987A in the Large Magellanic Cloud at 50 kpc distance made the first observation of the ^{56}Co and the ^{57}Co decay from a supernova possible.

The gamma-ray spectrometer GRS onboard the SMM satellite detected gamma-rays at 847 keV and 1238 keV from the ^{56}Co decay starting ≈ 6 months after the explosion [25]. The line flux was $1.0 \pm 0.25 \cdot 10^{-3}$ photons cm^{-2} s^{-1} for the 847 keV line and $6 \pm 2 \cdot 10^{-4}$ photons cm^{-2} s^{-1} for the 1238 keV line. The appearance was about 6 months earlier than expected from theory, and suggested that mixing and/or fragmentation of the ejecta had taken place during or shortly after the explosion.

The profiles of the 847 keV and the 1238 keV lines were measured with several balloon-borne experiments [19]. The balloon-borne HPGe spectrometer GRIS observed SN1987A 433 and 613 days after the explosion [20]. The lines were redshifted by 400 to 900 km s^{-1}, contrary to what is expected from an optically thick source. The observed line broadening corresponds to velocities of 2700 to 3800 km s^{-1}, larger than model predictions, perhaps indicating that some of the ^{56}Co had

penetrated the high-velocity H-rich envelope. However, it is important to note that the significance of the GRIS measurement was low, with significances of 2.3 σ to 4.6 σ for the individual lines.

The ^{57}Co decay from SN1987A was observed by the OSSE instrument aboard CGRO 4 years after the explosion [21]. The ^{57}Co decay gives rise to lines at 122 and 136 keV, but due to Compton scattering in the source, the excess will be smeared out in energy. OSSE detected an excess in the 50 to 136 keV region with an observed flux of $9 \pm 2 \cdot 10^{-5}$ cm^{-2} s^{-1}. From the observed mass of ^{57}Co and ^{56}Co from SN1987A, the ratio of daughter nuclides ^{57}Fe to ^{56}Fe was determined to 1.5 ± 0.5 times solar.

The type Ia supernova 1991T in NGC4527 at the edge of the Virgo cluster at ≈13 Mpc distance exploded 1 week after the CGRO launch. Observations with OSSE [22] and with COMPTEL [23] showed no evidence for the ^{56}Co lines, with upper limits of $4.1 - 6.6 \cdot 10^{-5}$ ph cm^{-2} s^{-1} (OSSE, 99% CF) and $\approx 3 \cdot 10^{-5}$ ph cm^{-2} s^{-1} (COMPTEL, 2 σ) for the lines at 847 keV and 1238 keV. More recent data analysis of the COMPTEL observations show evidence for the ^{56}Co lines at 847 and 1238 keV with a combined flux of $(8.9 \pm 3.4 \pm 2.7) \cdot 10^{-5}$ photons cm^{-2} s^{-1} [24]. This observation would imply a production of 1.3 ± 0.5 M$_\odot$ of ^{56}Ni in the supernova explosion, consistent with models for an optically bright type Ia supernova. However, the COMPTEL positive detection exceeds the OSSE 3 σ upper limit for the 847 keV line.

Observations of the 3 kpc distant and about 300 year old supernova remnant Cas A with COMPTEL have led to the detection of the 1157 keV line from ^{44}Ti, with a flux of $(7.0 \pm 1.7 \pm 2.1) \cdot 10^{-5}$ photons cm^{-2} s^{-1} [26]. More recent analysis using more observations leads to a flux of $4.8 \pm 0.9 \cdot 10^{-5}$ photons cm^{-2} s^{-1} [27]. The line is larger than the instrumental resolution, the Doppler-broadening is 24 ± 9 keV, corresponding to a velocity of 7200 ± 2900 km/s. There is some uncertainty in the half-life of ^{44}Ti, needed to convert the line flux into a produced mass of ^{44}Ti. Recent measurements find a halflife of ≈ 63 yr [28]. The ^{44}Ti yield implies a large mass of ^{56}Ni, which again implies a bright supernova ($M_V < -4$). However, the supernova went unreported, requiring an optical extinction of 10 magnitudes to be consistent.

The first cosmic radioactivity detected in gamma-rays was ^{26}Al from observations with the HEAO3 Ge gamma-ray spectrometer. A preliminary search gave an indication of the 1809 keV line at a 2.6 σ confidence level [31]. With more observations, the line was detected at the 5 σ confidence level, with a flux of $4.8 \pm 1.0 \cdot 10^{-4}$ photons cm^{-2} s^{-1} rad^{-1} coming from the vicinity of the Galactic center [32]. The observed line energy of 1809.49 ± 0.41 keV was consistent with the decay of ^{26}Al at rest.

The first mapping of the Galactic center region in the light of the ^{26}Al line was carried out with the MPI Compton telescope in a balloon flight observation [33]. The observations of the COMPTEL detector aboard CGRO have allowed the mapping of Galactic distribution of ^{26}Al in some detail [34] [35]. The COMPTEL 1.809 MeV sky map shows the sites of nucleosynthesis of the last 10^6 years. The data show a diffuse, irregular emission along the Galactic plane and a central bright spot a few degrees offset from the Galactic center (see Fig. 1). Emission hotspots are seen along the Galactic plane in the region of Carina (l=290°), Vela (l=270°), Cygnus (l=80°) and others. The Cygnus hotspot can be attributed to several tens of supernovae in the past million years. The Vela hotspot could be due to the Vela supernova remnant and/or to the closest Wolf-Rayet star

γ Vel [36]. Several of the hotspots are along the tangents of spiral arms in our Galaxy. The sky distribution favors a massive star origin of the ^{26}Al, with supernovae and Wolf-Rayet stars as the main production sites.

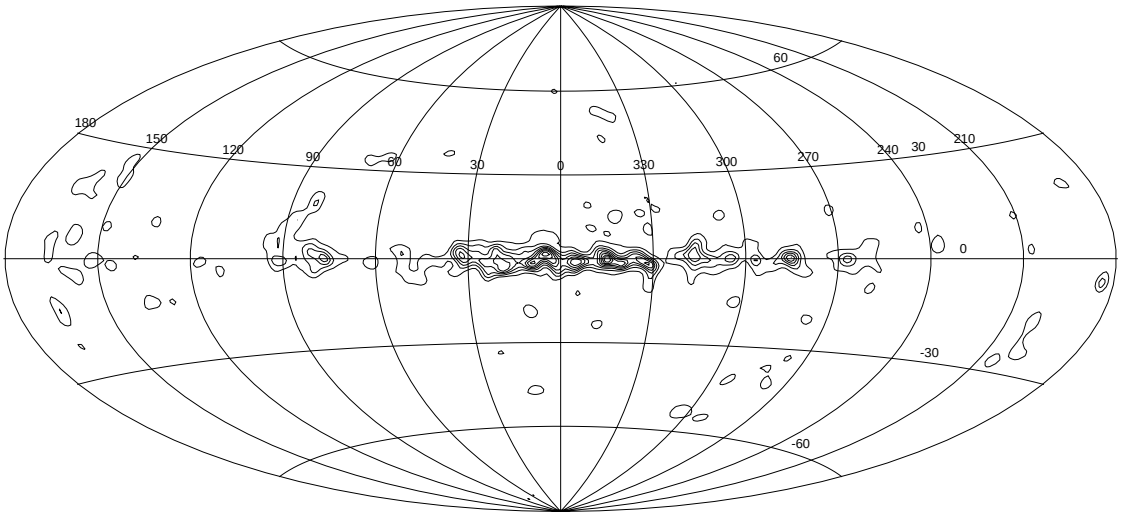

Figure 1: *The COMPTEL 1.8 MeV all-sky map for observation periods 0.1 - 522.5 derived by maximum entropy deconvolution (from [37]).*

Due to the 10^6 year lifetime, ^{26}Al should have slowed down before decaying and should therefore exhibit velocities typical of the differential Galactic rotation of < 150 km/s plus random motion of the interstellar medium. However, the balloon-borne gamma-ray spectrometer GRIS observed the ^{26}Al line from the Galactic plane during a flight in October 1995 to be broadened with a width of $5.4^{+1.4}_{-1.3}$ keV FWHM, implying velocities of > 450 km/s [38]. However, the high-resolution spectrometer HEAO-C reported a width compatible with a narrow line, and a 1σ intrinsic-width upper limit of 3 keV [39].

Gamma ray lines from nuclear deexcitation, neutron capture reactions

COMPTEL observations of the Orion/ Monoceros region show an excess in the 3 to 7 MeV range, which is tentatively attributed to nuclear deexcitation lines at 4.44 and 6.13 MeV from accelerated ^{12}C and ^{16}O nuclei [29]. The 3 to 7 MeV radiation is observed at the 9 σ significance level with a flux of $12.8 \pm 1.5 \cdot 10^{-5}$ photons cm^{-2} s^{-1}. The emission extends over the complex (the Orion A and B and the Mon R2 clouds), and may be due to a few localized source regions. There is also evidence (4.4 σ) for emission from the Mon OB1/OB2 area.

Narrow nuclear deexcitation lines arising from the interaction of protons accelerated in solar flares with ambient heavy nuclei have been detected in the spectra of strong flares. Deexcitation lines from ^{16}O (6.129 MeV), ^{12}C (4.439 MeV), ^{28}Si (1.779 MeV), ^{20}Ne (1.634 MeV), ^{24}Mg (1.369 MeV) and ^{56}Fe (0.847 and 1.238 MeV) were observed with the gamma-ray spectrometer aboard SMM for

the 1981 April 27 solar flare [30]. The line intensities, integrated over the 30 minutes of the burst, range from 0.2 to 40 photons cm^{-2}. Furthermore, excesses at $\approx$ 5.3 MeV and $\approx$ 7.0 MeV were detected, presumably from the inelastic excitation and spallation of ^{16}O. The neutron capture line at 2.223 MeV as well as the annihilation line at 511 keV were also detected.

Cyclotron lines

The first detection of a cyclotron scattering resonance feature was by Trümper et al. 1978 [40] in the spectrum of Hercules X-1. The feature was first interpreted as an emission line at 58 keV, with some evidence for a line at the second harmonic energy. More recent observations of Hercules X-1 by GINGA show that the feature is better described as an absorption line at 35.4±1 keV and a line width of 11.3±2.0 keV [41]. A recent review of cyclotron observations is given by Parmar 1994 [42]. Cyclotron scattering resonance features have been detected from nine pulsars at energies between 7 keV and 40 keV, corresponding to a range of surface magnetic field strength of $(0.8 - 4.4) \cdot 10^{12}$ G. There is evidence for a second harmonic in the spectra of six of the nine pulsars. For some systems such as Vela X-1, the cyclotron feature is only detected for part of the pulse phase. The energy can vary by as much as 30 % with pulse phase.

A small number of gamma-ray burst spectra have shown some evidence for cyclotron features, providing evidence for a magnetic neutron star origin of at least a fraction of gamma-ray bursts [43], [44]. Several spectra show two spectral dips which could be interpreted as the first and second cyclotron harmonic. The burst GB890929 observed by GINGA showed double line features near 25 keV and 50 keV, which could be due to resonant cyclotron scattering in magnetic fields of $\approx 1.7 \cdot 10^{12}$ G. However, analysis of data from the Spectroscopy Detectors of the Burst and Transient Source Experiment (BATSE) on CGRO has found no convincing line features in the spectra of gamma-ray bursts [45]. Due to the small number of bright bursts seen by BATSE and GINGA, there may not be a significant discrepancy between the two instruments [46]. Recent analysis of BATSE data using an automatic search procedure has led to 12 candidate bursts with spectral features, mostly at energies around 40 keV [47]. The recent observation of the optical counterpart to GRB970228 with the Hubble Space Telescope may indicate the association of gamma-ray bursts with high-redshift galaxies [48]. This could favor a fireball model of gamma-ray bursts [49], which would make cyclotron features unlikely.

3 Instrumentation in Hard X-Ray and Gamma-Ray Astronomy

Space-based gamma-ray astronomy spans almost 6 decades in energy. This implies a wide range of different detection techniques. The type of detector is determined by the dominant interaction mechanism of the detector material and the gamma-rays. At energies below several hundred keV, photoelectric absorption dominates. Between several hundred keV and tens of MeV, the Compton effect dominates. At higher energies, pair production dominates.
In this chapter, the different telescope types used in hard X-ray and gamma-ray instrumentation are reviewed. After a general description of each of these detection techniques, currently operational telescopes and a selection of next-generation detectors are briefly described.
Below 20 keV, grazing incidence telescopes are used (section 3.1). The use of multilayers with a d-gradient may increase this range to 100 keV (section 3.2). Bragg concentrators have been proposed for the energy range < 200 keV (section 3.2). Coded aperture masks cover the energy range of a few tens of keV to a few MeV (section 3.3). Compton telescopes have a working energy range of hundreds of keV to tens of MeV (section 3.4). At energies above tens of MeV, electron-positron tracking detectors together with calorimeters are used (section 3.5).

3.1 Grazing Incidence Telescopes

Grazing incidence mirrors use the principle of total reflection of X-rays. The complex index of refraction is given by [50]

$$n = 1 - \delta - i\beta \tag{3}$$

δ and β are the dispersive and absorptive parts of the index of refraction, and are given by

$$\delta = \frac{N_A(Z/A)\rho e^2 \lambda^2}{2\pi mc^2} \tag{4}$$

and

$$\beta = \frac{\mu\lambda}{4\pi} \tag{5}$$

away from the absorption edges. N_A is Avogadro's number, Z is the atomic number, A is the atomic weight, ρ is the density, e^2/mc^2 is the classical electron radius, μ is the absorption coefficient, and λ is the photon wavelength. As the refractive index is less than unity, X-rays incident on a material are totally reflected if the glancing angle θ is less than the critical angle θ_c. For θ_c one finds

$$\theta_c = \sqrt{2\delta} = 2.99 \cdot 10^{-23}\sqrt{n_e}\lambda[\text{Å}] \tag{6}$$

with n_e as the electron density. θ_c is typically less than 1° for X-ray wavelengths: at 8 keV, $\theta_c = 0.29^\circ$ for quartz and $\theta_c = 0.57^\circ$ for gold.
Grazing incidence X-ray telescopes consist of paraboloids and hyperboloids of revolution, with a reflective metal coating on their inner faces. This so-called Wolter configuration is necessary to avoid severe aberrations of a single-reflection telescope, and makes imaging with arc second resolution possible over a field-of-view of typically up to 1 degree. To increase the effective area, mirrors

are nested, i.e., consist of concentric mirrors with increasing diameter. Major advances have been made in mirror fabrication technology [51]: the mirrors for early X-ray missions were made from polished fused silica with reflective coatings such as Ni-Cr. These mirrors have good optical quality, but are heavy and costly. More lightweight mirrors can be obtained with electroformed full cylindrical Ni shell optics. Au is deposited onto super-polished mandrels, after which Ni is electroplated onto the gold. When the Ni-shell is removed by cooling, the Au adheres to the Ni, forming the reflective coating. Mirrors with less than 1 nm micro roughness can be achieved. Mirrors can also be formed from thin aluminum foils dipped in acrylic lacquer and then overcoated with gold. These mirrors are leightweight, thin, and less costly than other mirror types and thus enable large collection areas, but have reduced optical quality. The critical angle determines the field of view of the instrument, and is typically less than 2 degrees, decreasing with increasing energy. The focal length is typically several m. The focal plane instrumentation utilizes gas scintillation proportional counters, multiwire proportional counters, microchannel plates, semiconductor detectors such as pin diodes, segmented Si(Li), Ge(Li), CdTe, as well as X-ray sensitive CCDs. For high-resolution spectroscopy, Bragg crystal spectrometers and gratings are used.

ROSAT is an X-ray telescope proposed by the MPE in Garching, Germany, and built in cooperation with the US and the UK. ROSAT was launched 1990 by a Delta 2 rocket. The X-ray telescope consists of 4 nested Wolter telescopes with an 80 cm diameter and a focal length of 2.25 m. The focal plane instrumentation includes two position sensitive proportional counters as well as a high-resolution imager.

In the following, the X-ray missions, ASCA, AXAF, and XMM will be briefly described [52]. The Japanese satellite ASCA, launched in Feb. 1992, consists of 4 telescopes working in the energy range of 1 to 12 keV. Each telescope consists of two sets of 120 conical foils approximating a paraboloid-hyperboloid shape. The field of view is 24 arc minutes, the angular resolution is 3 arc minutes. The effective area is 600 cm^2 at 7 keV. The focal plane instrumentation consists of 2 CCD-based X-ray cameras and two imaging gas scintillation proportional counters.

The American Advanced X-Ray Astrophysics Facility (AXAF) is planned for launch in Fall 1998. The instrument consists of 4 nested Ir-coated mirrors in a Wolter geometry, with an outer mirror diameter of 1.2 m and a focal length of 10 m. The angular resolution will be better than 0.5 arc seconds over the 1° field of view. A high-energy and a low-energy grating together with a microchannel plate detector and a CCD-based X-ray camera will be used.

The X-ray Multi Mirror (XMM) mission is an ESA Horizon 2000 Cornerstone mission, and is planned for launch in 1999. The telescope consists of 3 individual nested Wolter telescopes, with a focal length of 7.5 m. The mirrors were fabricated using the Ni-electroforming technique. There are 3 CCDs, one at the focus of each telescope. Reflection gratings are used above 2 of the 3 CCDs for spectroscopy.

3.2 Hard X-ray Telescopes

As the critical angle for total reflection of X-rays is inversely proportional to the photon energy (equation 6), the effective area of Wolter-type telescopes becomes extremely small at energies above 20 keV.

The use of multilayers can increase this energy range up to 100 keV. Multilayers are periodic structures made of alternating layers of materials with a high and a low index of diffraction. Ni/C and W/Si multilayers have been successfully constructed [57]. Typical layer thicknesses are 20 Å to 100 Å. Multilayer reflection is governed by the Bragg formula $2dsin\theta = n\lambda$ with θ as the Bragg angle, n as an integer, and λ as the photon wavelength. For multilayers, d is the layer spacing, i.e., the period of the multilayer. The energy bandwidth is determined by the number of layer pairs participating in the reflection, and increases with decreasing number of layer pairs [53]. This is essentially the particle size broadening described by the Scherrer equation (equation 13.3 in [54]). Coating a Wolter-type mirror with multilayers would lead to a broadband instrument, as each mirror covers a range of grazing angles due to the mirror curvature. Higher energies could be focused: for a multilayer period d of 100 Å and a graze angle θ of 1 mrad, the focused energy is 62 keV.

A high reflectivity over a larger energy bandpass can be obtained using multilayers with a gradient in the d-spacing [55]. For a d-gradient multilayer, an incident photon encounters a range of d-values, and is reflected by the layers of d that fulfill the Bragg relation. As higher energy photons are absorbed less, the d-spacing decreases with increasing depth.

An American-Japanese collaboration is working on the realization of a balloon experiment InFOCμS, which would use a telescope system with nested thin foil mirrors with d-gradient multilayers [56]. The focal length would be 8 m. First reflectivity tests of Pt/C multilayers on replica foils show promising results.

For the energy range of 10 keV to 200 keV, Bragg concentrators have been proposed. These telescopes use the Bragg diffraction in surface-reflection geometry to concentrate photons onto a detector in the focal plane. The diffraction is governed by the Bragg relation $2dsin\theta = n\lambda$, with d as the crystalline plane spacing, θ as the Bragg angle, and λ as the incident photon wavelength. Due to the focusing, good sensitivities can be achieved.

A Bragg concentrator HEXTEL using mosaic pyrolithic graphite crystals has been proposed [58]. The concentrator consists of 28 confocal parabolical mirrors. Each mirror is made up of small pieces of mosaic crystal with the diffraction planes parallel to the parabolical surface, which results in a broadband energy response. The outer diameter is 1.3 m, the focal length is 3.8 m. The effective area is 1000 cm^2 at 15 keV decreasing to 35 cm^2 at 100 keV. An angular resolution of a few arc minutes could be achieved.

3.3 Coded Aperture Telescopes

A coded aperture telescope consists of a mask and a position sensitive detector plane (see Fig. 2) [64]. The mask consists of an array of opaque and transparent elements. Every source or source element within the field-of-view projects a shadow of the aperture onto the detector plane. The fully-coded field of view comprises all directions for which the mask shadow covers the entire detection plane. For a mask and a detector plane of the same dimension, the entire field-of-view, except for the on-axis direction, is only partly coded. For this reason, the mask is typically larger than the detector.

The sizes of the detector and the mask elements and the mask-detector distance determine the

sensitivity and angular resolution of the telescope. The angular resolution $\Delta\alpha$ is determined by the mask element size d, the mask-detector distance D, and the spatial resolution of the detector. Making the mask element size smaller than the spatial resolution of the detector would increase the angular resolution, but degrades the signal to noise ratio as well as the source localization accuracy. Typically, the mask element size and the detector element size are identical.
With A as the matrix which gives the transmission through the mask, S as the matrix of the source flux, and B as the matrix of the background counts, the encoding of the mask can be described by the correlation of A and S,

$$D = A * S + B. \tag{7}$$

D is the matrix of the detected flux. The decoding is achieved with a decoding matrix G so that

$$\hat{S} = G * A * S + G * B. \tag{8}$$

The mask thus needs to be designed so that $G * A$ is as close to a delta function as possible, and that the background is not amplified to distort or deteriorate the reconstructed image. So-called Uniformly Redundant Arrays (URAs) fulfill these criteria [65]. A URA is a matrix of dimensions $r \times s$ where r and s are prime numbers with $r - s = 2$. The mask pattern is obtained by a cyclic shift to obtain a coded mask with dimensions $2r$ times $2s$.

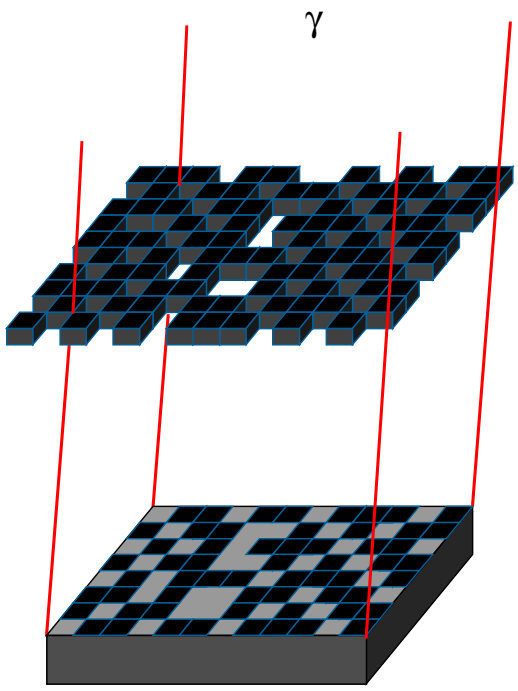

Figure 2: *The functioning principle of a coded aperture telescope is depicted (see text).*

The first orbiting instrument employing the coded mask technique was the X-Ray Telescope (XRT)

developed by the University of Birmingham and flown on the Spacelab-2 mission in 1985 [66]. Two telescopes with gold-coated masks about 3 m from position-sensitive proportional counters produced angular resolutions of 3 arc min and 12 arc min. The working energy range was 2.5 to 25 keV.

The SIGMA imaging telescope, constructed by the CEA Saclay and the CESR, was the first satellite-based coded-aperture telescope working at soft gamma-ray energies [67]. It was launched on-board the GRANAT space observatory in 1989. The detector consists of a 1.25-cm-thick NaI(Tl) crystal optically coupled to an array of 61 hexagonal photomultiplier tubes. The coded mask consists of 1.2-cm-thick tungsten elements with a URA base pattern of 49 $\times$ 53 elements. The distance between the mask and the detector is 2.5 m, the fully-coded field of view is 4.7° by 4.3°, and the geometric angular resolution is 13 arc minutes.

Next-generation coded-aperture mask telescopes aim to improve the angular resolution by decreasing the mask dimensions and improving the spatial resolution of the detector plane. Using sets of orthogonal strip detectors, arc second positioning of sources at energies up to 150 keV seems achievable. Also, the energy resolution of the detector plane can be improved using materials such as Si, Ge, and CdZnTe.

The BASIS (Burst ArcSecond Imaging and Spectroscopy) telescope uses a 2-cm-scale mask pattern superimposed on a 100 μm-pitch mask to achieve a precise ($<$ 30 arc second) positioning of gamma-ray bursts [68]. The mask consists of 100 μm thick Au on a Be substrate, and is fabricated using X-ray lithography. The detector, at a distance of 60 cm from the mask, consists of CdZnTe strip detectors with a 100 μm pitch wire-bonded to ASIC readout chips. The working energy range is 10 to 150 keV.

The AXGAM (All-Sky X-Ray and Gamma-Ray Monitor) concept consists of a large field of view instrument with an energy range of 1 to 200 keV [69]. The instrument consists of a dome made of hexagonal mask segments 0.5 to 0.8 m from the detector plane to achieve a field of view of 1 to 2 π. CdZnTe pin detectors with an element size of 100 μm $\times$ 100 μm and several mm thick are connected to ASIC readout chips below the detector plane via indium bumps.

The two main instruments aboard the INTEGRAL satellite, to be launched in 2001, utilize coded aperture masks.

The IBIS instrument uses $\approx$ 16000 6 $\times$ 6 $\times$ 2 mm^3 CdTe pixels and $\approx$ 4000 9 $\times$ 9 $\times$ 30 mm^3 CsI pixels in the detector plane [70]. The front-end electronics of the CdTe pixels are provided by ASIC chips, the CsI pixels are bonded to Si-PIN photodiodes. The 14 mm thick W mask is at a distance of 3.1 m from the detection plane, the fully coded field of view is 9° by 9°. The energy range of the instrument is 15 keV to 10 MeV. The angular resolution is 12 arc minutes.

The SPI spectrometer uses 19 HPGe detectors cooled to 85 K and a 3-cm-thick W mask at a distance of 1.7 m from the detector plane to achieve excellent energy resolution ($E/\Delta E = 500$ at 1 MeV) and good angular resolution (2°) [71]. The mask is a hexagonal uniformly redundant array (HURA) made up of elements with a 6 cm center-to-center distance. The detectors are n-type coaxial HPGe crystals 7 cm high and 6 cm wide. The crystals are enclosed in a Be cryostat. The working energy range is 20 keV to 8 MeV.

3.4 Compton Telescopes

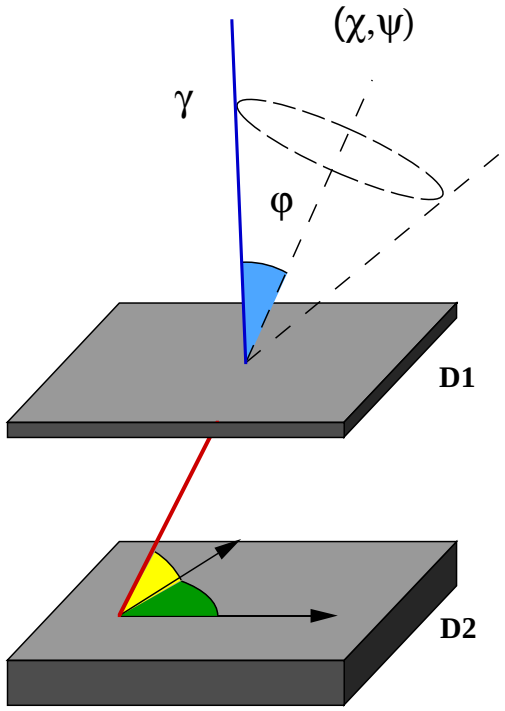

Figure 3: *The functioning principle of a Compton telescope is depicted (see text).*

A Compton telescope uses the Compton interaction to detect gamma-rays. The telescope consists of two position-sensitive detection planes, separated by a distance L (Fig. 3). An ideal event consists of a single Compton interaction in the upper detector plane D_1, with the energy of the recoil electron being fully absorbed in D_1. The Compton-scattered photon is then fully absorbed in the lower detector plane D_2. Thus, D_1 works as a converter and D_2 as a calorimeter. This implies using low Z materials such as organic scintillators, liquid argon, or silicon for D_1, and high Z materials such as inorganic scintillators, liquid xenon, germanium, or cadmium-zinc-telluride (CdZnTe) for D_2.

"Conventional" Compton telescope measure the electron recoil energy E_1, the Compton-scattered photon energy E_2, the position of the interactions x_1, y_1, x_2, y_2, and the time of both interactions t_1 and t_2. The direction of the recoil electron as well as the z position of the interactions are not measured. From the spatial information, the direction of the Compton-scattered photon (χ, ψ) is determined. The Compton scatter angle φ is determined from the energy measurements:

$$\varphi = acos\left(1 - m_e c^2 \left(\frac{1}{E_2} - \frac{1}{E_1 + E_2}\right)\right) \tag{9}$$

This implies that the incident photon direction is only known to a ring on the sky with a ring radius of φ centered on the scatter direction (χ, ψ).

Compton telescopes tend to have low background, as events rely on a coincidence between D_1 and D_2 [59]. For "conventional" Compton telescopes, a time-of-flight measurement is used to discriminate between upward and downward moving particles. Due to the polarization-dependence of the Klein-Nishina cross section, Compton telescopes can in principle be used as polarimeters.

The Compton telescope COMPTEL aboard the CGRO satellite launched April 1991 has 7 cylindrical modules filled with the liquid organic scintillator NE213A in detector plane D_1, and 14 cylindrical NaI crystals in D_2. Each D_1 module is viewed by 8 photomultiplier tubes arranged radially about the module, and each D_2 module is viewed from below by 7 photomultipliers. This allows a spatial resolution of 2.3 cm for D_1 and 1.5 cm for D_2 (1 σ errors). The distance between the detector planes is 1.5 m, the field of view is $\approx$ 1 sr. The energy resolution is $\frac{\Delta E}{E} = 0.04$ at 1 MeV.

Recent developments in improving the design of Compton telescopes aim at higher spectral and spatial resolution, as well as tracking the direction of the recoil electron, which would allow an unambiguous determination of the incident photon direction.

LXeGRIT is a next-generation liquid xenon imaging telescope working from 300 keV to 30 MeV that could be realized in the constraints of a MIDEX satellite mission [60]. It consists of two time projection chambers (TPCs)- a 15-cm-thick liquid argon TPC as D_1 and a 26-cm-thick liquid xenon TPC as D_2. Both scintillation light, which serves as a trigger, and ionisation electrons are produced as a result of the Compton interaction. The electrons drift to the anode, the charge induced on 2 orthogonal sets of wire planes determines the x and y coordinates of the interaction, the z coordinate is determined from the anode drift time. Multiple-interaction events can be reconstructed in three dimensions. The spatial resolution would be 250 μm in all directions, the energy resolution would be 0.012 at 1 MeV, and the angular resolution would be $\leq 0.14^\circ$ for events in both detector planes, and $\leq 0.4^\circ$ for events detected only in D_2. There would be about 10^4 readout channels per detector layer. The field of view would be $\leq$ 1 sr.

The TIGRE concept would use 50 layers of 200 μm thick, 25 μm pitch Si strip detectors as D_1 and 10 layers of 5-mm-thick, 375 μm pitch CdZnTe strip detectors as D_2 [61] [62]. The Si strip detectors would allow the tracking of the recoil electron above 400 keV. The telescope could be used up to 100 MeV by tracking pair-production events. The geometric angular resolution is 5 arc minutes, the energy resolution is 5 keV at 511 keV and 10 keV at 1809 keV. A laboratory prototype has been tested.

The ATHENA concept is a high-resolution Compton telescope using 2-mm-pitch Ge planar strip detectors to achieve an energy resolution of 2-3 keV and a spatial resolution of < 2 mm [63]. Both detector layers have a 1.4×1.4 m^2 surface made up of individual $5 \times 5 \times 1$ cm^3 Ge-strip detectors, with 1 layer of detectors as D_1 and 5 layers as D_2. The separation of the detector layers is 1 m. The Compton telescope would cover the energy range of 300 keV to 10 MeV, and would achieve narrow line sensitivities of a few 10^{-7} ph cm^{-2} s^{-1}. For the energy range 10 keV to 200 keV, a coded aperture mask above the D_1 layer would serve as a coded aperture telescope with a few arc minute angular resolution and a field-of-view of 10-15°.

3.5 High Energy Gamma-Ray Detectors

At energies above several tens of MeV, pair production is the dominant gamma-ray interaction process. Detectors consist of alternating layers of high-Z material converters and tracking detectors. Ideally, a pair-production occurs in the converter, and the electron and positron positions are determined in several tracking detectors. This allows a reconstruction of the incident photon direction. A calorimeter, generally an inorganic scintillator, is below the converter to absorb the total gamma-ray energy. The energy is then determined by correcting for the energy loss in the converters and tracking detectors.

The EGRET experiment aboard the CGRO satellite launched April 1991 consists of a spark chamber and an NaI crystal as calorimeter [72]. The spark chamber consists of two sections separated by a layer of segmented plastic scintillator which serves as a trigger to apply high voltage to the chamber. The upper section consists of 28 spark chamber modules interleaved with 27 thin Ta converter foils. The working energy range is 20 MeV to 30 GeV, the field of view is 0.6 sr. The effective area is 1200 cm^2 at 1 GeV.

The GLAST (Gamma-Ray Large Area Space Telescope) detector is a NASA mission concept study for a next-generation high energy gamma-ray detector [73]. The instrument uses layers of anticoincidence scintillators, converter foils and orthogonal single-sided 240 μm-pitch silicon strip detectors, followed by a segmented CsI(Tl) calorimeter. The design foresees 49 "towers", each of which is 24 $\times$ 24 cm large, and each of which consists of 10 converter/tracking layers followed by two tracking layers. The total area of the silicon strip detectors needed is 68 m^2, and the number of readout channels is $1.2 \cdot 10^6$. The CsI(Tl) calorimeter is segmented into 64 crystals each of size $3 \times 3 \times 19$ cm^3. The angular resolution would be 0.3° at 1 GeV, and 0.03° for energies > 20 GeV. The working energy range is 10 MeV to 300 GeV, the field of view is 2.5 sr. The effective area is 8000 cm^2 at 1 GeV.

4 A Crystal Lens Telescope

After reviewing some basic crystallographic terms (section 4.1), the functioning principle of a crystal lens telescope is described (section 4.2). Design criteria of a crystal lens telescope are discussed in the context of the Darwin mosaic model (section 4.3). The realization of the first prototype crystal lens from 1992 to 1995 with fixed crystal inclinations is reviewed (section 4.4). Using the configuration of this prototype, the imaging properties of a crystal lens telescope are discussed (section 4.5). A brief account of broadband concentrators as proposed by other groups follows (section 4.6).

4.1 Crystal Structure, the Bragg Relation

An ideal crystal is constructed by an infinite repetition of identical structural units in space. This ideal crystal structure is the lattice, with an atom or group of atoms attached to every lattice point. The atom or group of atoms form the basis. The lattice is defined by three fundamental translation vectors $\vec{a}_1, \vec{a}_2, \vec{a_3}$, and every lattice point can be described by $u_1\vec{a}_1 + u_2\vec{a}_2 + u_3\vec{a}_3$, $u_i \in \mathbf{N}$. The parallelopipedon defined by the translation vectors $\vec{a}_1, \vec{a}_2, \vec{a_3}$ is the unit cell, with cell volume $V = |\vec{a}_1 \cdot \vec{a}_2 \times \vec{a}_3|$. The lattices are grouped into seven types of cells. The cubic cell has $a_1 = a_2 = a_3$, and the axes are orthogonal, $\alpha = \beta = \gamma = 90°$. There are three lattices in the cubic cell system: the simple cubic, the body-centered cubic (bcc), and the face-centered cubic lattice (fcc). Many metals crystallize in the cubic structure: for example, copper is described by a face-centered cubic cell system with a basis composed of one atom. Silicon and germanium are described by the diamond structure: this is a fcc cell system with a basis of two atoms at (0, 0, 0) and (1/4, 1/4, 1/4) (Fig. 4). The cell size a is 3.51 Å for Cu (4 atoms per unit cell), 5.43 Å for Si (8 atoms per unit cell), and 5.66 Å for Ge (8 atoms per unit cell).

The crystalline plane is described by the Miller indices (hkl): with $\vec{a}_1$, $\vec{a}_2$, and $\vec{a}_3$ as the crystallographic axes designating the unit cell, the Miller indices (hkl) define equidistant crystalline planes with intercepts ma_1/h, ma_2/k, and ma_3/l, $m \in \mathbf{N}$ on the crystallographic axes. For a cubic unit cell with volume a^3, the crystalline plane spacing is $a/\sqrt{h^2+k^2+l^2}$.

The interaction of X-ray and gamma-ray photons with the atoms in the crystal leads to diffraction. Fig. 5 shows the elementary derivation of the Bragg condition, which assumes that the incident waves are reflected off the parallel planes of the atoms in the crystal. There is constructive interference if the optical path difference between neighboring paths is a multiple of the wavelength $n\lambda$:

$$\begin{aligned} n\lambda &= AB + BC - AE = 2AB - AE \\ &= 2\tfrac{d}{\sin\theta} - 2AD\cos\theta \end{aligned} \tag{10}$$

As $AD = \frac{d}{\tan\theta}$, this can be written as

$$n\lambda = n\frac{hc}{E} = 2d\sin\theta \tag{11}$$

Here, λ is the photon wavelength, E is the photon energy, θ is the angle with respect to the crystalline planes (if the Bragg condition is met, $\theta = \theta_b$ is called the Bragg angle), and n is a

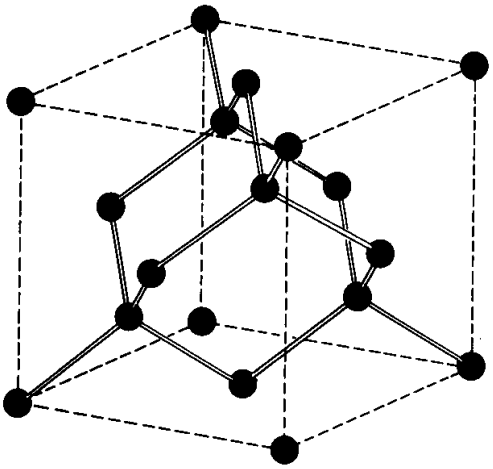

Figure 4: *The figure, adapted from [83], shows the diamond crystal structure. The structure is composed of a face-centered cubic cell with a basis of 2 atoms at (0, 0, 0) and (1/4, 1/4, 1/4). Germanium and silicon crystallize in this structure.*

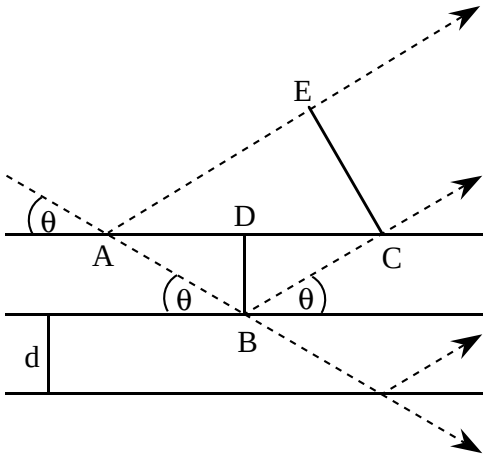

Figure 5: *The elementary derivation of the Bragg relation is depicted (see text).*

positive integer. The higher the energy of the incoming photon, the smaller the Bragg angle. At several hundred keV, Bragg angles are generally less than one degree.

The Bragg reflection can be a surface reflection (so-called Bragg geometry) or can pass through the crystal volume (so-called Laue geometry). This is shown in Fig 6. For high energies, Laue geometry is the better choice: due to the small Bragg angles at high energies, the crystal would need to be extremely long. For a 1-cm beam and a Bragg angle of 1 degree, the crystal length

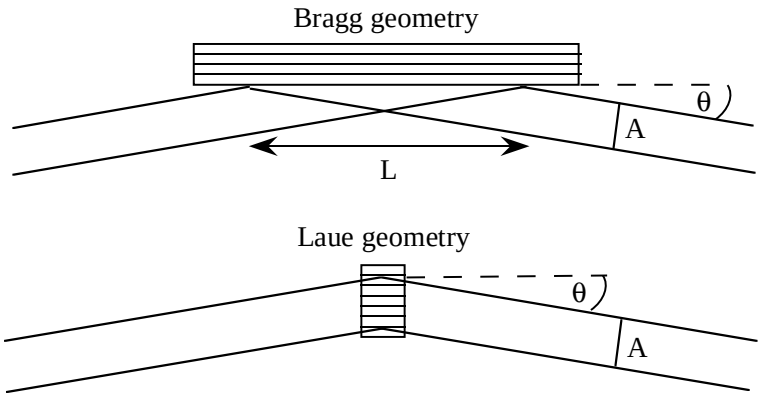

Figure 6: *The Bragg reflection can either be in Bragg geometry (upper plot) or in Laue geometry (lower plot). Laue geometry uses volume reflection, whereas Bragg geometry uses surface reflection. In Bragg geometry and for an incident photon beam with a cross-section A, the crystal needs to have a length L that is the beam size divided by the sine of the Bragg angle:* $L = A/\sin\theta_B$.

$A/\sin\theta_B$ would be 57 cm! Also, the attenuation due to the beam passing through the crystal becomes small at high energies, making Laue geometry possible.

4.2 Functioning Principle, Characteristics

A crystal lens telescope uses Bragg-reflection to focus gamma-rays. This is possible, as the diffraction process changes the direction of the incident photon by twice the Bragg angle. The functioning principle of a crystal lens is shown in Fig 7. For a crystal at a distance r_1 from an arbitrary optical axis, a photon with energy E_0 and an incident direction parallel to the optical axis is Bragg-reflected if the crystal is oriented so that the angle between the photon and the crystalline planes is the Bragg angle θ_1. The Bragg-reflected photon intercepts the optical axis at the focal length $f = \frac{r_1}{tan(2\theta_1)}$. For a second crystal at a larger distance from the optical axis, a photon with the same energy E_0 and the same incident direction parallel to the optical axis can only be Bragg-reflected with the same focal length if the Bragg-angle θ_2 is larger than θ_1. According to equation 11, this is only possible if the crystalline plane spacing is smaller.

By rotating Fig. 7 around the optical axis, one obtains concentric rings of crystals, with the crystals of one ring all using the same crystalline plane for the Bragg-reflection. As for a given crystal material only certain crystalline planes are possible, the ring radii are determined by the Miller indices (hkl). For materials with a cubic unit cell, the ring radii in small angle approximation are $const \cdot \sqrt{(h^2+k^2+l^2)}$. The Bragg-reflection is in Laue geometry.

As the Bragg relation is only valid in a small angle and energy range (determined by the mosaic width of the crystal, see section 4.3.1), only a narrow range of energies is focused at a time.

The focal spot is determined by the crystal size, as can be seen in Fig. 7. For crystals with a square surface, the focal spot FWHM is 1.08 times the crystal size. This is true for monochromatic

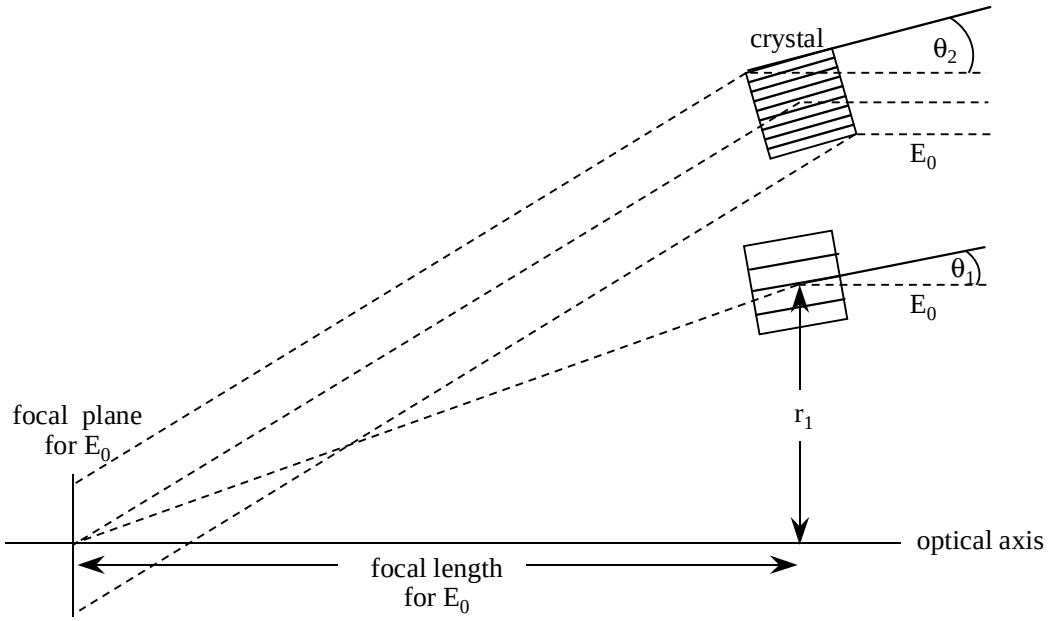

Figure 7: *The functioning principle of a crystal lens is depicted (see text). The gamma-ray trajectories are depicted as the dotted lines. The figure is not to scale; the Bragg angles at gamma-ray energies are of the order of one degree.*

radiation from a point source at infinity (i.e., incoming radiation parallel to the optical axis), for a discussion of crystals of arbitrary size and imaging properties for extended, continuum radiation, see section 4.5.4.

To change the energy that is focused by the crystals, according to equation 11 it is necessary to change the orientation of each crystal, each ring being changed by a different amount. The change in Bragg angle also leads to a change in focal length. The focal length increases linearly with energy in small angle approximation:

$$f = \frac{r}{\tan(2\theta)} \propto E. \tag{12}$$

4.3 Design Considerations

4.3.1 Perfect vs. Mosaic Crystals: The Darwin Mosaic Model

A perfect crystal reflects monochromatic radiation over an angular range ω_D called the Darwin width, that is

$$\omega_D = \frac{4r_e|F|d^2}{\pi V} \cdot tan(\theta_B) \tag{13}$$

with r_e as the classical electron radius, $|F|$ as the structure factor, d as the crystalline plane spacing, V as the unit cell volume, and θ_B as the Bragg angle ([79], eq.3.151, assuming a zero-absorption

thick crystal). At 200 keV, the Darwin width is 0.1 arc seconds for Ge (111), and 0.02 arc seconds for Ge (333). For continuum radiation with zero angular divergence, this translates into an energy bandpass of the Bragg-reflection of 0.01 keV for Ge (111) and 0.0007 keV for Ge (333), decreasing as $1/E$ with energy in small angle approximation. Excepting monochromatic line radiation, the source flux in such a small energy window is negligeable. To diffract monochromatic line radiation, the crystal would need to be oriented with a precision $\ll 1$ arc sec. These conditions imply that perfect crystals cannot be used for a crystal lens telescope.

Larger energy bandpasses can be achieved with so-called mosaic crystals. A mosaic structure model of a crystal was first proposed by Darwin [78]. In this model, the true defect structure of the crystal, which may be due to dislocations, inhomogeneous strains, etc., is described by an agglomorate of perfect crystal blocks. Each block is in itself an ideal perfect crystal, but adjacent blocks are slightly offset in angle with respect to one another (Fig. 8). The relative displacements of the blocks are large compared to the Darwin width, so that the blocks scatter incoherently. The block size is microscopic or sub-microscopic, so that a great number of blocks take part in the scattering process, and the angular distribution of the blocks can be defined as a continuous function. This distribution is assumed to be Gaussian. The FWHM is the so-called *mosaic width*, and is an intrinsic crystal property (Fig. 9). For a crystal lens telescope, crystals with mosaic widths ranging from a few arc seconds to a few arc minutes will be discussed.

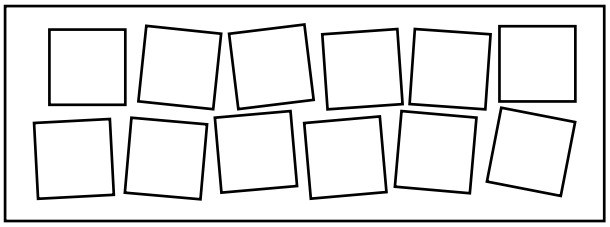

Figure 8: *The Darwin model describes the mosaic crystal as an agglomorate of perfect crystal blocks typically of microscopic size, each of which are offset in inclination from one another.*

The diffraction process for mosaic crystals is described in [79]. An important property of the diffraction process is the diffraction efficiency ε, defined as the ratio of the number of reflected to the number of incident photons. ε is a function of photon energy and of photon incident direction. The variation in the power of the incident and diffracted beams as a function of the penetration depth T inside the crystal is described by the two transfer equations ([79], eq. 4.21)

$$\begin{aligned} dP_0 &= -\mu_0 P_0 \frac{dT}{\gamma_0} - \alpha P_0 dT + \alpha P_H dT \\ dP_H &= -\mu_0 P_H \frac{dT}{|\gamma_H|} - \alpha P_H dT + \alpha P_0 dT \end{aligned} \tag{14}$$

with P_0 as the power in the incident beam, P_H as the power in the reflected beam, μ as the absorption coefficient, $\gamma = cos(\theta_B)$ as the cosine of the Bragg angle, and α as the diffraction coefficient. The first two terms in equation 14 describe the decrease in power due to absorption

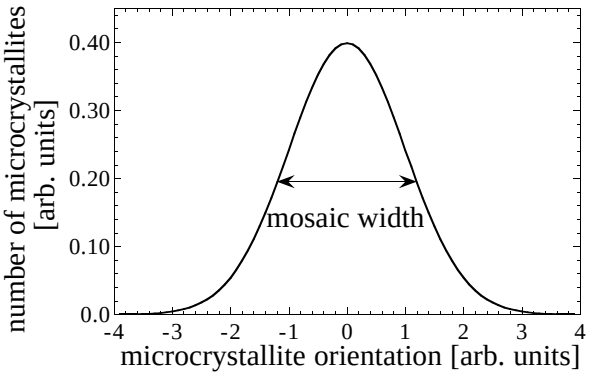

Figure 9: *The distribution of the inclination of the perfect crystal blocks is assumed to be Gaussian in the Dawin mosaic model, with a Full Width at Half Maximum (FWHM) called the mosaic width.*

and diffraction, the third term is the increase of the incident or of the diffracted beam due to reflection of the diffracted and incident beams respectively.
The solution of equations 14 for the Laue case, whereby the diffracted photon passes through the crystal volume, i.e., for the boundary conditions $P_H(0) = 0$, leads to the following expression for the diffraction efficiency ([79], equation 4.25):

$$\frac{P_H(T)}{P_0(0)} = \varepsilon = 0.5 \cdot exp(-\frac{\mu}{\gamma}T) \cdot (1 - exp(-2\alpha T)), \tag{15}$$

with T as the crystal thickness. The physics of the diffraction process is contained in the diffraction coefficient α,

$$\alpha dT = W\frac{R}{t_0}dT \tag{16}$$

with W as the normalized Gaussian distribution function of the block orientations, R as the integrated reflecting power of a single block, and t_0 as the block size. Equation 16 states that the relative power change due to diffraction in the layer of thickness dT equals the integrated reflecting power R of a single block times the probability that the block has the "correct" inclination W times the number of single block layers in dT, which is dT/t_0.
R is given by the zero-absorption thin crystal reflecting power if the so-called primary extinction is negligeable, meaning that the attenuation of the incident beam power by the diffraction process inside each mosaic block can be neglected. This is the case if the mean block size is much smaller than the so-called *primary extinction depth* t_{ext}, which for the Laue case is [80]

$$t_0 \ll t_{ext} = \frac{2V}{\pi r_e F \lambda}\sin(90^\circ - \theta). \tag{17}$$

At 200 keV, for Ge (111) one calculates $t_{ext} = 0.24$ mm, for Ge (333), $t_{ext} = 0.38$ mm.
The integrated reflecting power of a zero-absorption thin crystal is calculated in the kinematical theory by summing the electric field at a point P due to the scattering of all electrons in the crystal.

The scattered electric field from a single atom is proportional to the atomic structure factor

$$f = \sum_n \int exp\left(\frac{2\pi i}{\lambda}(\vec{s} - \vec{s}_0)\vec{r}\right)\rho_n(\vec{r})d^3r \tag{18}$$

which contains the electron charge density distributions ρ_n. The sum is over all electrons of the atom. $\vec{s}_0$ is the unit vector of the incident photon direction, and $\vec{s}$ is the vector of the scattered direction. The atomic structure factor is the amplitude of unmodified scattering (i.e., the energy is unchanged, in contrast to Compton scattering) and depends on $sin\theta/\lambda$ with θ as the scatter direction. For small $sin\theta/\lambda$, $f \longrightarrow Z$ with Z as the atomic number.
The scattered electric field from all atoms making up the unit cell is proportional to the structure factor

$$F = \sum_n f_n exp\left(\frac{2\pi i}{\lambda}(\vec{s} - \vec{s}_0)\vec{r}_n\right) \tag{19}$$

with the sum being over all atoms of the unit cell. The scattered intensity is proportional to the square of the electric field, and thus $\propto |F|^2$. Thermal vibrations of the atoms lead to a reduction of the scattered intensity by a factor of $exp(-2M)$, with $2M = 16\pi^2\overline{u^2}sin^2\theta/\lambda$ as the Debye-Waller factor. $\overline{u^2}$ is the variance of the component of the thermal displacement of the atoms normal to the diffraction planes.
The integrated reflecting power is then found by integrating the intensity over area and angle. For the case of the zero-absorption thin crystal, a more correct treatment of the diffraction process using the dynamical theory gives the same result as the kinematical theory described here.
Using the intensity of the zero-absorption thin crystal for a single block, α is given in small angle approximation as ([79], equations 4.33)

$$\alpha(\theta - \theta_b) = \frac{r_e^2 F^2 \lambda^3 e^{-2M}}{V^2 sin(2\theta_b(E))} \cdot \frac{1}{\sqrt{2\pi}\sigma} exp(-\frac{(\theta - \theta_b(E))^2}{2\sigma^2}), \tag{20}$$

with V as the volume of the unit cell, r_e as the classical electron radius, λ as the incident photon wavelength, θ as the angle of the incident photon, θ_b as the Bragg angle for the energy E, F as the structure factor, and σ as $1/(2\sqrt{2ln2})$ times the mosaic width. There is a second type of extinction due to the attenuation of the beam due to diffraction before reaching a given crystal block. For the lens crystals, this so-called secondary extinction is not negligeable.
In summary, equations 15 and 20 give the diffraction efficiency $\varepsilon(\theta, E)$ as a function of photon energy and incident angle, under the following assumptions

- the lattice imperfections can be described in the framework of the block model
- the distribution of the orientation of the blocks is Gaussian and homogeneous over the crystal volume
- the blocks scatter incoherently, i.e., the mosaic width of the crystal is much larger than the intrinsic Darwin width of a single perfect block
- the block size is small compared to the primary extinction depth, so that absorption in a single crystal block can be neglected

The last two conditions are more easily met at high energies, as the Darwin width decreases with energy as $1/E$ and the primary extinction length increases linearly with energy. For the energy range of 200 keV to 2000 keV discussed here, the extinction depth is typically a fraction of a mm to a few mm, and the Darwin width is typically 0.1 to 0.001 arc seconds. Thus, even crystals with a mosaic width of a few arc seconds can fulfill the above conditions.
In equation 15, the diffraction efficiency is the product of an absorption term $exp(-\frac{\mu}{\gamma}T)$ and a diffraction term $(1-exp(-2\alpha T))$. The diffraction efficiency is always ≤ 0.5. This can be understood as the loss of information of the incident and reflected direction due to multiple reflections in the crystal.
Equations 15 and 20 form the basis of the calculations presented in this thesis and govern many of the design parameters of the crystal lens, including the choice of crystal material, the choice of mosaic width, the working energy range and the number of rings. These will now in turn be discussed.

4.3.2 Crystal Material

According to equations 15 and 20, the value of the diffraction coefficient to the absorption coefficient, α/μ, should be maximized in order to maximize the diffraction efficiency. Both α and μ are energy-dependent, α also depends on the mosaic width. For the calculations in this section, the mosaic width was fixed to 10 arc seconds.
Only regarding pure elements, the dependence of the diffraction coefficient α on the crystal material and energy can be crudely estimated to

$$\alpha \propto \frac{F^2\lambda^3}{V^2 sin(2\theta_b)} \propto \frac{1}{E^2}\frac{Z^2N_{cell}^2}{V^2}$$
$$=> \alpha \propto \frac{\rho^{5/3}}{E^2} \tag{21}$$

Here, the small angle approximation $sin(2\theta) = 2sin\theta$ was used. N_{cell} is the number of atoms per unit cell, Z is the atomic number, V is the unit cell volume, and ρ is the density of the material. Using the proportionality of the atomic weight to the atomic number, $A \propto Z^{1.2}$, $ZN_{cell}/V \propto \rho^{5/6}$. The absorption coefficient μ_c due to Compton scattering scales linearly with density and decreases slowly with energy in the region of interest here. The decrease between 100 keV and 1000 keV is typically only a factor of 2 to 3. Assuming that μ_c is independent of energy, for the Compton-dominated energy region one finds

$$\frac{\alpha}{\mu} \propto \frac{\rho^{2/3}}{E}, \tag{22}$$

so that elements with high densities are superior.
At lower energies where photoabsorption dominates, $\mu \propto \rho Z^5/E^3$ [81]. For this energy region

$$\frac{\alpha}{\mu} \propto \frac{\rho^{2/3}E}{Z^5}, \tag{23}$$

so that elements with smaller Z are more advantageous.

The qualitative results of these estimates can be validated with explicit calculations. In the following, Cu, Ge, and Si crystals are compared. All three elements crystallize in the face-centered cubic form.

For Ge and Si, there are 8 atoms per unit cell at positions (0, 0, 0), (1/2, 1/2, 0), (1/2, 0, 1/2), (0, 1/2, 1/2), (1/4, 1/4, 1/4), (3/4, 3/4, 1/4), (3/4, 1/4, 3/4), and (1/4, 3/4, 3/4) (see e.g. [83]). The structure factor is determined with

$$F_{hkl} = \sum_n f_n exp(2\pi i(hx_n + ky_n + lz_n)), \tag{24}$$

with f_n as the atomic structure factor, (x_n, y_n, z_n) as the positions of the atoms in the unit cell, and the sum being over all atoms in the unit cell. The f_n are tabulated in [82]. The structure factor is $F_{hkl} = 8f_{hkl}$ for $h + k + l = 4n$ with n as an integer, $F_{hkl} = 5.65f_{hkl}$ for h, k, l all odd, and zero otherwise. Thus, crystalline places with a non-negligeable reflection instensity are (111), (220), (311), (400), (331),...

For Cu, there are 4 atoms per unit cell at positions (0, 0, 0), (1/2, 1/2, 0), (1/2, 0, 1/2), (0, 1/2, 1/2). The structure factor is $F_{hkl} = 4f_{hkl}$ for h, k, l all even or all odd, and zero otherwise. Thus, crystalline places with a non-negligeable reflection intensity are (111), (200), (220), (311), (222),...

The densities are 8.96 g/cm^3 (Cu), 5.32 g/cm^3 (Ge), and 2.33 g/cm^3 (Si). The unit cell size is 3.61 Å (Cu), 5.43 Å (Ge), and 5.65 Å (Si). The atomic numbers are Z=29 (Cu), Z=32 (Ge), and Z=14 (Si).

Fig. 10 (left plot) compares the α/μ-parameter as a function of lens radius for a lens made of Cu, Ge, and Si at 500 keV. The radii are chosen to have an identical focal length which is 8 m at 500 keV. Each point corresponds to a different crystalline plane. The innermost eight crystalline planes for Ge along with the corresponding radii are tabulated in Table 3. The "zigzag" behaviour of the Ge and Si points in the left-hand plot of Fig. 10 is due to the fact that the planes with $h + k + l = 4n$ are more efficient than those with h, k, l all odd. Thus, the (220) plane has a larger α than the (111) plane, the (400) plane has a larger α than the (311) plane, etc. At 500 keV, Cu is always more efficient than Ge, and Ge is always more efficient than Si. Fig. 10 (right plot) shows the dependence of α/μ on energy for the planes of the two innermost rings for Cu, Ge and Si. Even though Si with its lower atomic number is inferior to Ge and Cu at high energies (equation 22), at energies below 100 keV Si is superior to Ge and Cu (equation 23).

The discussion above did not consider the practical difficulties associated with the crystal growth. In reality, the growth of mosaic crystals is non-trivial.

For low energies and surface-reflection (Bragg geometry), Highly Oriented Pyrolithic Graphite (HOPG), available with mosaic widths of 0.2 to several degrees, is commonly used [84]. For Ge, Si, and other crystals, surface lapping with abrasive powders or dipping the crystal into liquid nitrogen can increase the mosaic width of the surface. The disadvantage of these techniques is that the mosaic width is depth-dependent.

Ge and Si crystals are typically highly perfect (mosaic widths $<$ 1 arc second) after growth. However, Si crystals with mosaic widths of a few arc seconds have been achieved by annealing Czochralski-grown crystals [87]. The annealing process leads to the formation of SiO_2-clusters which deform the lattice. Recently, mosaic widths between 40 and 130 arc seconds have been

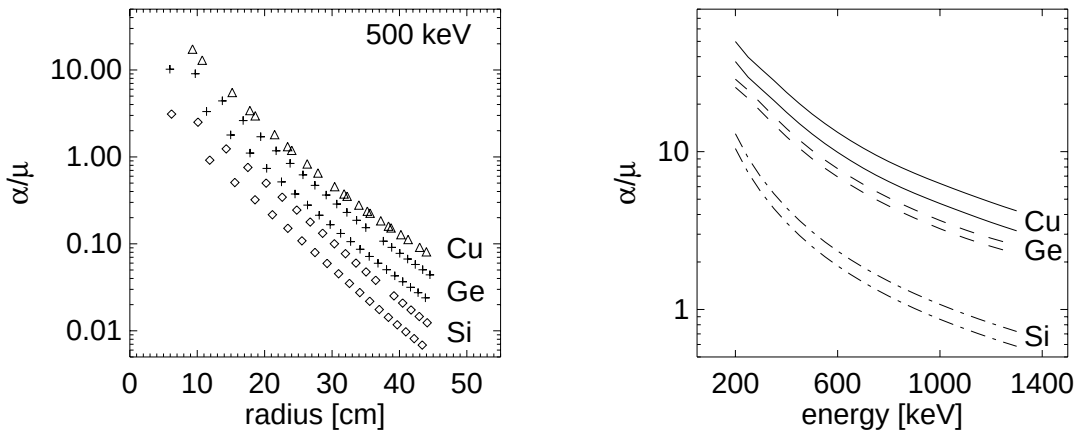

Figure 10: *The diffraction efficiency of Cu (triangles, solid lines), Ge (crosses, dashed lines), and Si (diamonds, dashed-dotted lines) is compared. The left plot shows the ratio of the diffraction and the absorption coefficient α/μ as a function of the lens radius for identical focal lengths normalized to 8 m at 500 keV. Each point corresponds to a different crystalline plane. The calculations are for 500 keV, and a mosaic width of 10 arc seconds. The right plot shows α/μ as a function of energy for the two innermost reflection planes for each element, i.e., the (111) and the (200) planes for Cu, and the (111) and the (220) planes for Ge and Si.*

achieved with Si-$TaSi_2$ crystals, where the highly perfect silicon matrix contains several volume % of metallic $TaSi_2$ in form of rods oriented parallel to the (111) silicon growth direction [85]. Keitel et al. [86] have studied the diffraction properties of Czochralski grown $Si_{1-x}Ge_x$ gradient crystals in Laue geometry at 120 keV, and find mosaic widths of 15 to 50 arc seconds and peak reflectivities up to 96% neglecting absorption. The mosaic width is seen to increase with increasing concentration of Ge. The mosaic width can also be increased by heating and squeezing the crystal.

4.3.3 Mosaic Width and Energy Bandwidth

The diffraction coefficient α is inversely proportional to the mosaic width, so that the peak diffraction efficiency decreases with increasing mosaic width. From equation 15, the thickness that maximizes the peak efficiency is given by

$$T_{max} = \frac{1}{\alpha} ln \frac{\alpha + \mu}{\mu} \tag{25}$$

with μ as the absorption coefficient and α as the diffraction coefficient. In Fig. 11, T_{max} is plotted as a function of mosaic width. The figure shows that T_{max} increases with increasing mosaic width. This is intuitively clear, as the probability of finding a crystal block with the "right" orientation decreases as the mosaic width increases, so that the crystal needs to be thicker to compensate

for this effect. A thicker crystal however absorbs more of the incident radiation, so that the peak efficiency decreases.
The choice of mosaic width is governed by the following factors:

- The integrated reflectivity $\int \varepsilon(\theta, E_0) d\theta$ assuming incident photons with fixed energy E_0 increases with increasing mosaic width (see Fig. 12). The increase is at first steep, then flattens off to only rise asymptotically. This can be seen qualitatively in Fig. 13, where reflectivity curves $\varepsilon(\theta, E_0)$ are plotted for mosaic widths of 5, 30, 60, and 120 arc seconds.

  This result can be interpreted in terms of an observation of a point source with a flat source spectrum with a crystal lens telescope. If the source is aligned with the optical axis of the lens, the integrated reflectivity $\int \varepsilon(\theta, E_0) d\theta$, which is the efficiency for fixed energy and variable angle, translates to $\int \varepsilon(E, \theta_0) dE$, the efficiency for fixed angle and variable energy. $\int \varepsilon(E, \theta_0) dE$ is then proportional to the focused source flux. For large mosaic widths, the integrated reflectivity is essentially constant (Fig. 12), so that the same detected source flux gets spread out over an ever larger energy window. For a crystal lens telescope, the background increases linearly with the size of the energy window. This implies that there is a background-dependent mosaic width that optimizes the sensitivity.

- The energy bandpass of a Bragg reflection is proportional to the square of the energy. This can be seen by forming the derivative of the Bragg relation in small angle approximation:

$$\begin{aligned} 2d\theta &\approx \frac{hc}{E} \\ \frac{\Delta\theta}{\theta} &= \frac{\Delta E}{E} \\ \Delta E = \frac{\Delta\theta}{\theta} E &\propto E^2 \end{aligned} \tag{26}$$

  $\Delta\theta$ is the mosaic width of the crystal, and ΔE is the energy bandpass of the reflection. If the scientific objective of a crystal lens telescope is the observation of gamma-ray lines, the mosaic width should be large enough so that the energy window at the lowest working energies is comparable to expected line widths. Typical energy bandpasses for mosaic widths of a few tens of arc seconds are 5 to 10 keV at 500 keV and 25 to 50 keV at 1300 keV. As the energy bandpass of the n-th order diffraction plane is reduced by a factor of n (e.g. the energy bandpass of (333) diffraction is 1/3 that of the (111) diffraction assuming the same mosaic width), it may be advantageous to use crystals with larger mosaic widths in the outer rings.

- For intensity mapping of slightly extended emission, it is necessary that the angular resolution of the crystal lens is smaller than the emission region size. Assuming a detector with infinite energy resolution, for a crystal lens the FWHM of the directional error of a single event equals the mosaic width of a single crystal. At low energies, the detector energy resolution adds an additional uncertainty in the direction of a single event (see section 4.5.3).

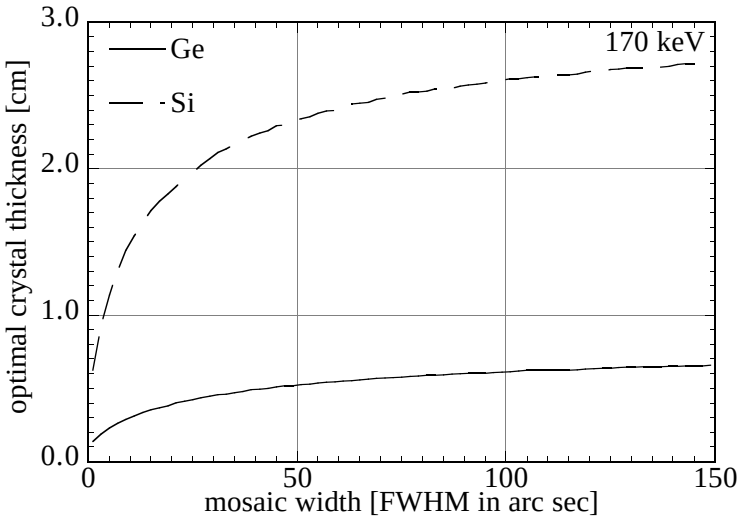

Figure 11: *The thickness that maximizes the diffraction efficiency (equation 25) is plotted as a function of mosaic width for Si and Ge. The calculation is for 170 keV.*

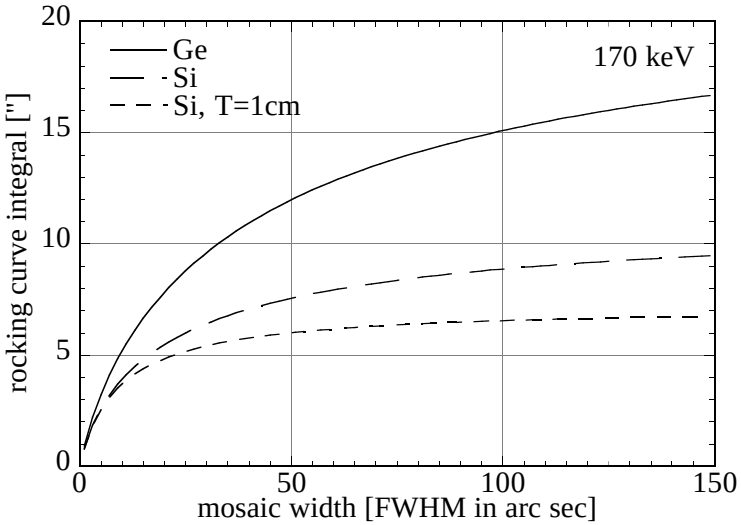

Figure 12: *The rocking curve integral, i.e. the integrated reflectivity* $\int \varepsilon(\theta) d\theta$ *is plotted as a function of mosaic width for Si and Ge. At each mosaic width, the crystal was assumed to have the optimal thickness as shown in Fig. 11. For comparison, the values calculated for a 1-cm-thick Si crystal are also plotted. The calculation is for 170 keV.*

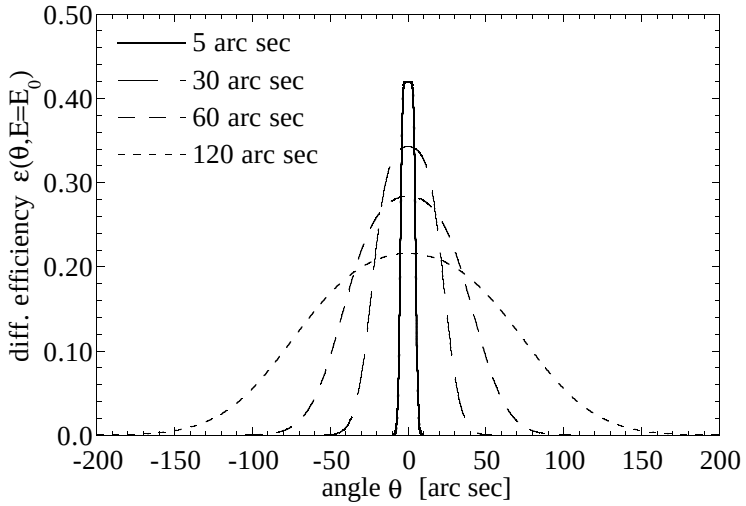

Figure 13: *The diffraction efficiency as a function of angle is plotted for mosaic widths of 5, 30, 60, and 120 arc seconds. The calculation is for the Ge (111) diffraction and for incident monochromatic radiation of energy 170 keV.*

4.3.4 Crystal Thickness and Working Energy Range

The crystal lens telescope described in this work only focuses one energy or at most a few energies at a time in order to obtain a large effective area, a large gain and thus good sensitivity. The working energy can however be changed by changing the distance between the detector and the lens and by changing the orientation of the crystals. The range of energies that such a telescope can focus is limited due to the following factors:

- As stated in section 4.3.3, the crystal thickness that maximizes the peak efficiency (for a given mosaic width) is $T_{max} = \frac{1}{\alpha} ln \frac{\alpha+\mu}{\mu}$. As both μ and α are energy-dependent, the optimal thickness changes with energy. For increasing energy, the optimal thickness increases. This limits the working energy range of a crystal lens, as a crystal with a given thickness will only diffract efficiently in a limited energy range. This is shown in Fig. 14, where the peak efficiency as a function of crystal thickness is shown for 4 different energies for a Ge (400) crystal with 10 arc seconds mosaic width. Assuming a thickness of 8 mm (dotted vertical line), the diffraction efficiency is small below 200 keV and above 1000 keV. At low energies, the absorption in the crystal dominates, at high energies, the decrease of α with energy dominates.

- As the focal length and thus the lens-detector distance of the instrument increases linearly with energy, $f \propto E$, the high-energy range of the instrument is limited by the maximal feasible focal length. For the prototype lens described in section 4.4, the focal length is 21.1 m at 1300 keV.

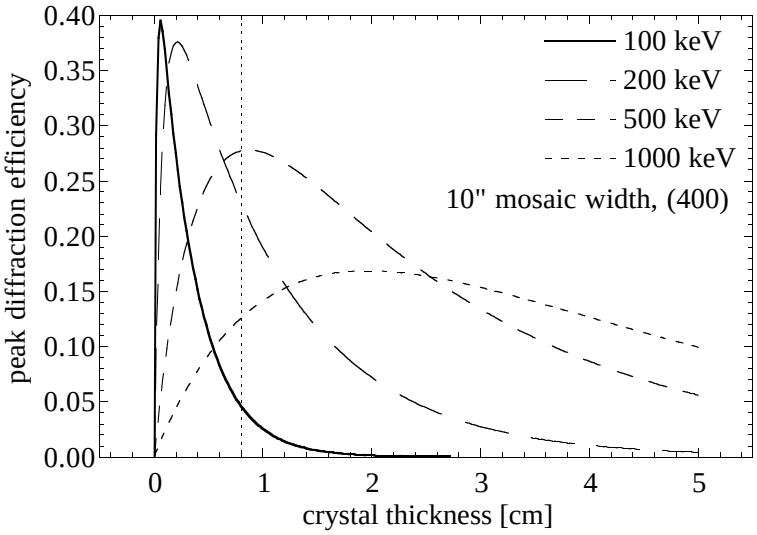

Figure 14: *The peak diffraction efficiency is shown as a function of crystal thickness for 4 different energies. The calculations are for the Ge (400) plane and a mosaic width of 10 arc seconds. A crystal thickness of 8 mm is depicted by the vertical dotted line.*

- The diffraction coefficient α decreases with the square of energy. The crystal can be made thicker to compensate, but the net effect is still a decrease of diffraction efficiency with increasing energy. This can be seen by the decrease of the α/μ-parameter with increasing energy in Fig. 10, as well as in Fig. 14, where the peak efficiency is smaller for the higher energies.

- Most importantly, the working energy range depends on the scientific objectives. Calculated and observed gamma-ray lines from novae and supernovae range from the ^{44}Ti-lines at 68 and 78 keV to lines at several MeV. Another main objective is the observation of annihilation radiation.

4.3.5 Number of Crystal Rings

For a given crystal material, the ring radii r_i are determined by the crystalline planes, and are given by $r_{hkl} = const * \sqrt{h^2 + k^2 + l^2}$. The crystals of the outer rings generally contribute less to the focused flux due to the following factors:

- The diffraction coefficient α is generally smaller for the crystalline planes used in the outer rings. The dependence of the diffraction coefficient on the crystalline plane is $\alpha \propto |F|^2/\sqrt{h^2 + k^2 + l^2}$. The structure factor $|F|$ decreases with increasing $\sqrt{h^2 + k^2 + l^2}$ and thus with increasing ring radius, and $\sqrt{h^2 + k^2 + l^2}$ increases with increasing ring radius.

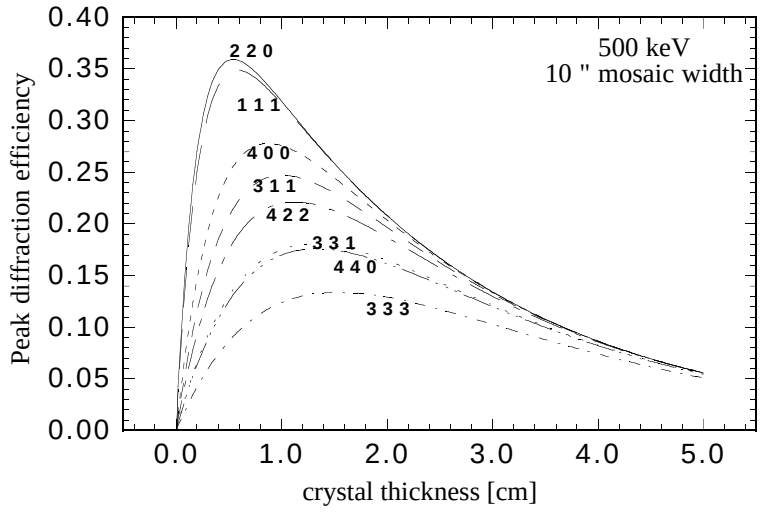

Figure 15: *The peak diffraction efficiency at 500 keV for Ge as a function of crystal thickness is shown for eight crystalline planes. The mosaic width is assumed to be 10 arc seconds. For a crystal lens, the (111) plane corresponds to the innermost ring, and the (440) plane to the outermost ring.*

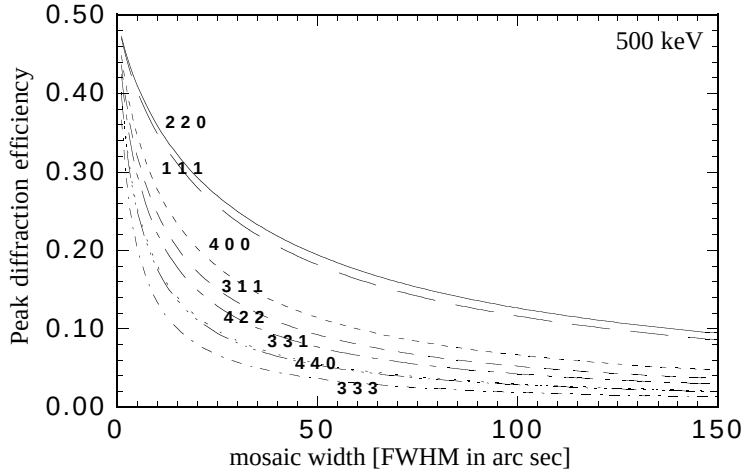

Figure 16: *The peak diffraction efficiency at 500 keV for Ge is shown as a function of mosaic width for eight crystalline planes. For each mosaic width, the crystal was assumed to have a thickness that maximizes the peak efficiency. For a crystal lens, the (111) plane corresponds to the innermost ring, and the (440) plane to the outermost ring.*

- Assuming crystals with a fixed mosaic width, the energy bandpass is smaller for the crystalline planes used in the outer rings. The energy bandpass of a reflection scales with $1/\sqrt{h^2+k^2+l^2} \propto r^{-1}$.

- The Debye-Waller temperature factor is larger for the crystalline planes used in the outer rings. For Ge (111) and a temperature of 300 K, α is reduced by a factor of $exp(-2M) = 0.98$, whereas for Ge (440), the reduction is $exp(-2M) = 0.76$.

The decrease of the efficiency of the outer rings can be seen in Figures 15 and 16, which show the peak efficiency as a function of crystal thickness and mosaic width for eight planes of Ge.
The effects listed above lead to each ring having roughly the same integrated reflectivity, even though the crystal area (the number of crystals per ring) increases for the outer rings. This is shown in Table 2, where the integrated reflectivity and the crystal area per ring are listed for eight crystalline planes of Ge. For a given energy, the diffraction coefficient α of the outer rings is smaller. As the absorption coefficient μ is independent of the ring, the optimal thickness T_{max} for the outer rings is larger. This is also shown in Table 2.

ring number	reflection plane [hkl]	$\sqrt{h^2+k^2+l^2}$	crystal area	T_{max} [cm]	peak efficiency	$A_i \cdot \int \varepsilon(\theta) d\theta$ [arc sec]
1	111	1.7	1.0	0.28 (0.80)	0.34 (0.34)	16.2 (5.18)
2	220	2.0	1.9	0.30 (0.84)	0.33 (0.33)	29.5 (5.25)
3	311	3.3	2.1	0.44 (1.26)	0.24 (0.24)	20.7 (6.85)
4	400	4.0	2.7	0.40 (1.12)	0.27 (0.27)	30.8 (10.21)
5	331	4.4	3.0	0.54 (1.52)	0.18 (0.18)	20.3 (6.72)
6	422	4.9	3.3	0.48 (1.36)	0.22 (0.22)	28.4 (9.37)
7	333	5.2	3.6	0.60 (1.72)	0.13 (0.13)	17.4 (5.74)
8	440	5.7	3.9	0.54 (1.54)	0.18 (0.18)	25.6 (8.47)

Table 2: *The crystalline plane defined by the Miller indices (hkl), $\sqrt{h^2+k^2+l^2}$ which is proportional to the ring radius, the crystal area relative to the innermost (111) ring, the crystal thickness that maximizes the peak efficiency T_{max}, the peak diffraction efficiency, as well as the integrated reflectivity multiplied with the crystal area, $A_i \cdot \int \varepsilon(\theta) d\theta$, are listed for eight planes of Ge. The calculations are for 170 keV and crystals with 30 arc second mosaic width. The values in parenthesis are for 500 keV and crystals with a 10 arc second mosaic width.*

4.3.6 Detector Design

The detector in the focal plane should have an energy resolution that is better than the energy bandpass of the lens at the lowest working energy, and the detector pixel size should be matched to the focal spot size. The detector should have a high full energy peak efficiency over the entire working energy range of the telescope.

A matrix of close-packed, identical HPGe detectors fulfills the above requirements. The size of one detector element should contain most of the integrated intensity of the focal spot, and the element thickness should be about twice the interaction length $1/e$ for gamma-rays at the highest working energy of the telescope ($1/e$=0.35 cm at 100 keV, $1/e$=2.9 cm at 1 MeV [76]). Centering the focal spot on a single detector element maximizes the signal-to-noise ratio: the effective background volume is reduced due to the rejection of all events with no energy deposit in the element containing the focal spot, whereas the gamma-ray detection volume is larger than the background volume due to neighboring elements that can absorb Compton-scattered photons. The focal spot can also be allowed to wander over the surface of the detector, either if the lens is adjusted to scan over a small region of the sky without adjustment the detector, or if the pointing precision of the telescope requires a fine adjustment of the lens orientation. This leads to an increase in the effective detector volume by a factor of 2 to 3, and thus a loss of sensitivity. Assuming the position of the focal spot is known, this can however eliminate the need for separate OFF-source measurements. Depending on the element size, a large fraction of gamma-rays can be multi-element events at energies above several hundred keV. This can be used to discriminate against localized beta events, the dominant source of background in this energy range [75]. The use of enriched ^{70}Ge can also decrease the detector background by a factor of 1.2 to 2 at energies of 200 keV to 1 MeV [74].

4.4 Description of the Ground-Based Prototype, Test Results

A ground-based prototype lens was built at Argonne National Laboratory in 1992-1995 [90], [91], [92], [93]. A photo of this lens is shown in Fig. 17. The lens consists of an Al-frame with 45 cm diameter, which holds 600 Ge-crystals in 8 rings. The crystals are 1 cm^3 cubes, excepting the 5th and 7th ring, which have a 0.8 × 1.0 cm^2 surface, and are 1.5 cm thick. The total lens area is 563 cm^2. The crystalline planes, ring radii, Bragg angles at 500 keV and other parameters of this lens are listed for each ring in Table 3.

ring number	reflection plane [hkl]	crystal size height × width × thickness [cm^3]	number of crystals	radius [cm]	Bragg angle at 500 keV [degree]
1	111	1 × 1 × 1	28	5.95	0.21
2	220	1 × 1 × 1	52	9.70	0.35
3	311	1 × 1 × 1	60	11.40	0.42
4	400	1 × 1 × 1	76	13.75	0.50
5	331	0.8 × 1 × 1.5	84	14.98	0.54
6	422	1 × 1 × 1	92	16.84	0.60
7	333	0.8 × 1 × 1.5	100	17.86	0.64
8	440	1 × 1 × 1	108	19.44	0.70

Table 3: *The crystalline plane, the crystal size, the number of crystals per ring as well as the ring radius and the Bragg angle at 500 keV are listed for each ring of the prototype crystal lens.*

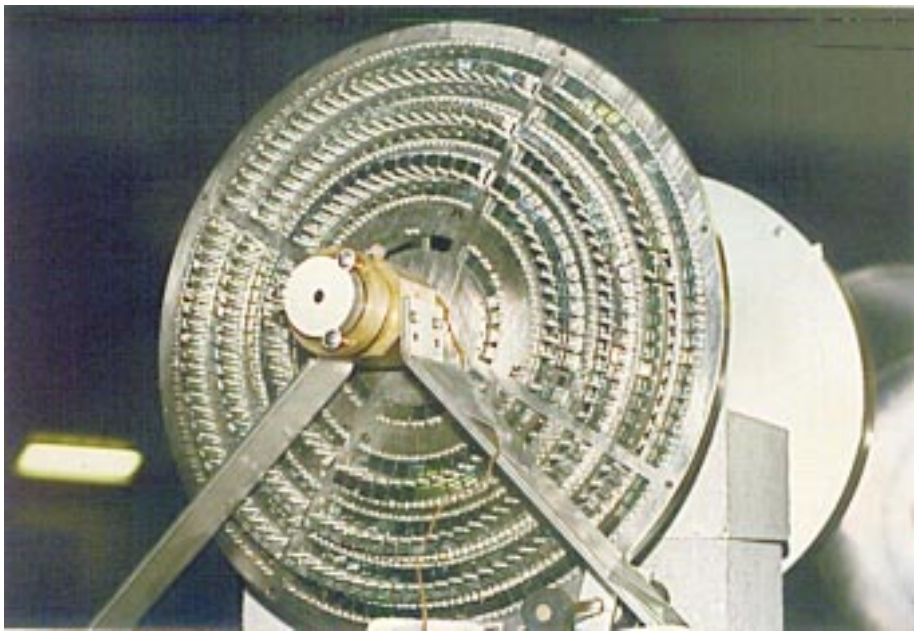

Figure 17: *A photo of the ground-based prototype crystal lens built at Argonne National Laboratory completed in 1995. The 45-cm diameter aluminum frame holds 600 Ge crystals in 8 rings. The crystals are glued onto Al-plates which are fixed onto the frame. The ring radii are determined by the reflection planes and are thus not equidistant.*

The focal length of the lens is 8.3 m at 511 keV, increasing linearly with energy. The crystal orientation was adjusted manually and then fixed. The adjustment was done via a spring mechanism pushing on the plate holding the crystal, which allowed a very fine adjustment of the orientation (Fig. 18).

The lens was tested with line energies ranging from 303 to 662 keV using ^{22}Na, ^{133}Ba, ^{137}Cs, and ^{239}Pu gamma-ray sources placed at 10 to 25 m distance from the lens, and with a single HPGe detector as well as a HPGe detector array placed at 10 to 20 m distance from the lens. The single HPGe detector (EG&G Ortec GEM-X) was a 6-cm-diameter p-type coaxial detector with a central 1-cm diameter bore customized to a length of 3 cm. The HPGe detector array (from Eurysis, Strasbourg) consisted of a 3 × 3 detector matrix housed in a single Al-cryostat. Each of the 9 detectors is a 1.5 × 1.5 × 4 cm^3 n-type coaxial detector, with a central hole of 0.5 cm diameter and 3.5 cm long. The single detector size of 1.5 × 1.5 cm^2 is well-suited to the focal spot size (FWHM 1.1 cm) of the lens. This makes it possible to reject a large fraction of background events, as the focal spot can be centered on one detector, and events with no energy deposit in this detector can be rejected.

Even though the crystal orientation was fixed, it was nonetheless possible to focus a range of energies. This is only true for a source at finite distance, as can be seen from Fig. 19: For a source

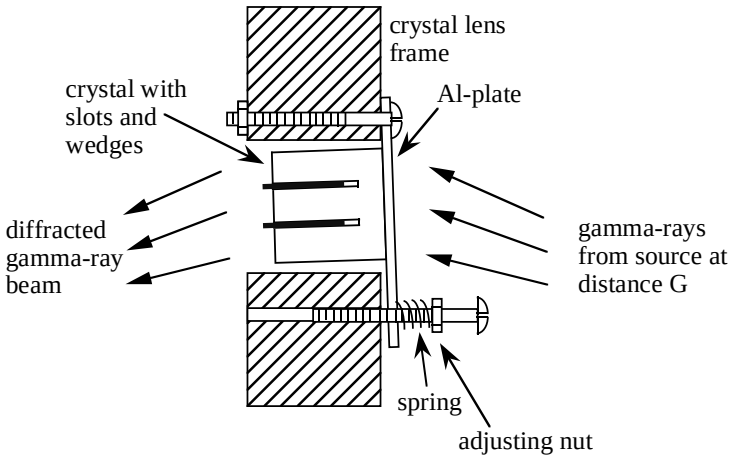

Figure 18: *The figure, adapted from [93], shows the mounting and the adjustment of a crystal on the prototype lens. The crystal is glued onto an Al-plate mounted onto the lens frame. The orientation of the crystal is changed by adjusting a nut that pushes the plate via a soft spring that increases the sensitivity of the adjustment by a factor of 100. The figure also shows the "wedging" of the crystal: in order to better match the angular divergence of a source at finite distance, the crystals are slotted parallel to the diffraction planes. Plastic sheets are inserted into the slots to bend and strain the crystals.*

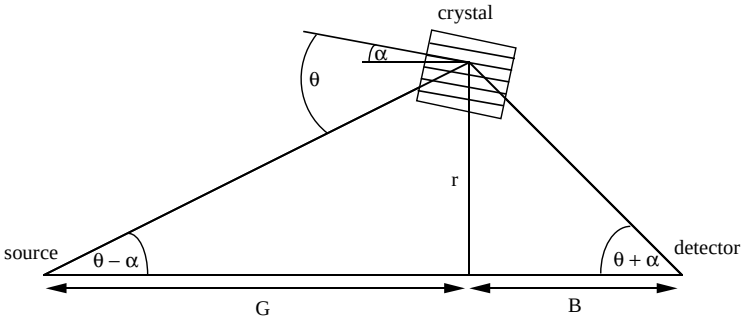

Figure 19: *A crystal that focuses gamma-rays of energy $E_\circ$ aligned with the optical axis can also focus gamma-rays of a different energy from a source at finite distance. G is the source-lens distance, B is the detector-lens distance. The Bragg angle for gamma-rays of energy $E_\circ$ aligned with the optical axis is α, the Bragg angle for a source at distance G is θ.*

at distance G and a detector at distance B from the lens and a crystal with radial distance r from the optical axis, one derives $tg(\theta - \alpha) = \frac{r}{G}$ and $tg(\theta + \alpha) = \frac{r}{B}$, with θ as the Bragg angle for the source at finite distance, and α as the Bragg angle for a source at infinity. By subtracting these

two equations, one finds

$$\alpha = 0.5 \cdot \left(atg\frac{r}{G} - atg\frac{r}{B} \right) \tag{27}$$

By adding the two equations, one finds in small angle approximation ($\tan\theta \approx \theta$)

$$\frac{1}{f} = \frac{1}{B} + \frac{1}{G} \tag{28}$$

where the relation for the focal length $f = \frac{r}{2\theta}$ has been used. The fixed crystal orientation means that α is fixed. The focal length for a given energy is fixed by the lens radii. Thus, for each energy only one pair (B,G) is possible, as B and G are constrained by both equations 27 and 28. For a point source at infinity, B is infinite, meaning that only one energy can be focused. This makes it necessary to motorize the crystals for a space-borne lens.

The results of the tests with the prototype lens can be summarized as follows:

- The gain of the lens, i.e., the number of photons detected with the lens compared to the number of photons detected without the lens, was 2.0 at 511 keV. This was measured using the count rate in the single, 6-cm-diameter HPGe detector. This translates into a diffraction efficiency of 2.8% for the crystals at 511 keV. The lens diffraction efficiency ranged from 3.3% at 303 keV to 5.6 % at 662 keV. This low efficiency is due to the mismatch of the mosaic width of the crystals and the angle that the source subtends over the crystal.

- For the 3 × 3 HPGe detector, events with no energy deposit in the pixel or pixels containing the focal spot are rejected as background events. The background rejection efficiency, defined as $(N(E_0) - N(E_0, E))/N(E_0)$ with $N(E_0)$ as the number of counts with total energy E_0 and $N(E_0, E)$ as the number of counts with total energy E_0 and an energy deposit in the pixels containing the focal spot, was measured at 511 keV with the laboratory ambient background flux. The background rejection efficiency was 79.3% for the focal spot centered on the central pixel, 66.3% for the focal spot centered between 2 pixels, and 44.9% for the focal spot centered between 3 pixels. This implies a sensitivity improvement of 2.2, 1.7, and 1.3 for the three cases assuming a background-dominated measurement. For a satellite-based crystal lens telescope, even at the sensitivity limit this is not the case. For the focal spot centered on the central pixel, the effective volume for the background is only about 2 single detector volumes, whereas the active volume for gamma-rays focused by the lens is the full detector size (9 single detector volumes).

The low diffraction efficiency measured in the ground-based tests were due to the fact that the crystals used were too perfect. The mosaic width was a few arc seconds, whereas the angle that the source subtends over the crystal ranged from 80 to 200 arc seconds. This means that only a narrow slice of the crystal volume was actually diffracting. In order to increase the volume contributing to the diffraction, two slots parallel to the diffraction planes were cut into the crystal. Plastic sheets were inserted into the slots to strain and bend the crystals to better match the divergent gamma-ray beam (Fig. 18, so-called "wedging" of the crystals). The "wedging" led to an increase of a factor of 3 in efficiency. The above-quoted values for the efficiency are those for the wedged crystals. The "wedging" is only optimal for one source-lens distance. For a spaceborne crystal lens, non-wedged crystals will be used.

4.5 Imaging Properties, Calculation of the Telescope Performance

In this section, the diffraction efficiency formulas in section 4.3.1 and the configuration of the prototype lens are used to determine the lens efficiency as a function of photon energy and direction as well as the focal plane image. For the calculations, the crystals are not wedged and the mosaic width is 10 arc seconds. The formulas for the lens response for a given source flux distribution as well as for the line sensitivity of a lens telescope are presented. These formulas form the basis of the performance simulations in sections 5 and 6.

4.5.1 Off-Axis and Off-Energy Efficiency

The coordinate systems used are shown in Fig. 20. The lens is in the XY-plane, the optical axis is the Z-axis (Fig. 20 a). The direction of an incoming photon is described by an angle ψ_p with respect to the Z-axis, and an angle ϕ_p, which is the azimuthal angle of the direction projected into the XY-plane. The position of each crystal is described by an azimuthal angle ϕ_c in the XY-plane, and a crystal coordinate system $X_c Y_c$ can be defined for each crystal by rotating the XYZ-system by $\phi_c - 90°$ about the Z-axis.

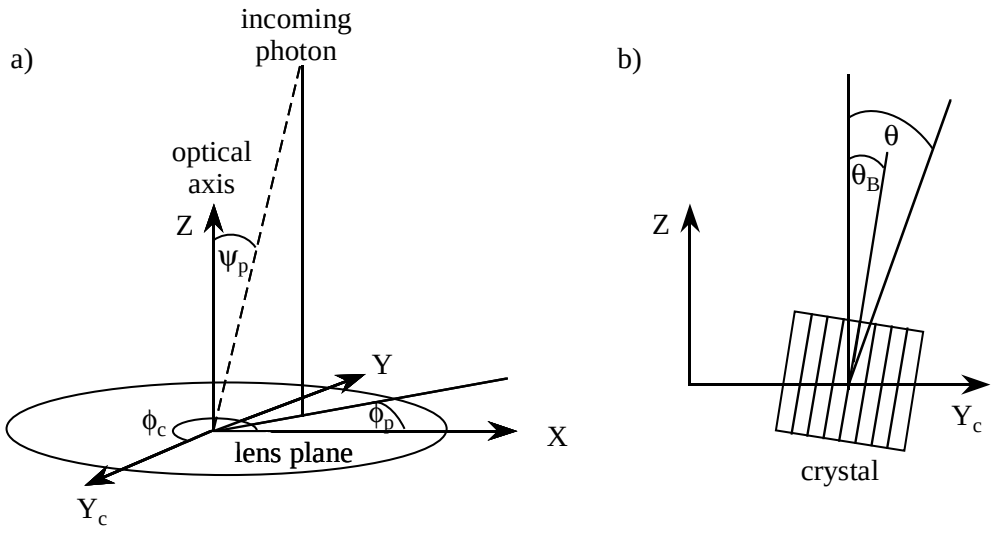

Figure 20: *Plot a) shows the coordinate systems used in the calculation of the off-axis and off-angle response of the lens. Plot b) shows the diffraction planes of the crystal in the $Y_c Z_c$ plane of the crystal system. The angle between the projection of the incident photon direction onto the $Y_c Z_c$ plane and the crystalline planes is θ. θ_B is the Bragg angle for an incident photon with a direction parallel to the optical axis with energy E_0.*

Assuming that the lens crystals are oriented to focus an energy E_0 from photons aligned with the optical axis Z, one can calculate the diffraction efficiency of the entire lens for photons with energy

E and an incident direction (ψ_p, ϕ_p). Equations 15 and 20 define the diffraction efficiency of the incident photon as a function of energy and angle with respect to the crystalline planes. The angle θ between the photon direction and the crystalline planes of a given crystal is found by rotating (ψ_p, ϕ_p) into the crystal system and then projecting the vector into the $Y_c Z_c$ plane. θ is the angle between this projected vector and the Z-axis (Fig. 20, b). The offset of the angle θ from the Bragg angle θ_B is decisive for the diffraction efficiency. This offset is

$$\theta - \theta_B = \psi_p cos(\phi_p - \phi_c) + \frac{E - E_0}{E}\theta_B + \delta \tag{29}$$

whereby the first term describes the offset of the incident photon from the optical axis, the second term contains the difference in energy between the incident photon and E_0, and the third term is a possible "detuning" of the crystals.
The average diffraction efficiency for the point (ψ_p, ϕ_p) and energy E is then

$$\bar{\varepsilon}(\psi_p, E|E_0) = \sum_i \varepsilon_i(\theta - \theta_B) \tag{30}$$

whereby the sum is over the lens crystals, and $\theta - \theta_B$ is given by equation 29. The efficiency is independent of azimuth ϕ_p due to the concentric rings of crystals.
Assuming perfectly oriented crystals, Figures 21 and 22 show surface plots of $\bar{\varepsilon}$ as a function of off-axis angle and energy. Fig. 21 averages over the crystals of the innermost (111) ring, whereas Fig. 22 is the average over the entire lens. The calculations are for $E_\circ = 500$ keV and assume 1 cm thick crystals.
The peak efficiency decreases with increasing off-axis angle, and for large off-axis angles there are two efficiency maximas, one at an energy lower than $E_\circ$ and one at an energy higher than $E_\circ$. The offset of these maxima from $E_\circ$ increases with increasing off-axis angle.
For a given energy E, the efficiency is maximal for an off-axis angle of $\psi_p = (E - E_0) \cdot \theta_B$. For Figure 21, θ_B is the Bragg angle for the (111) diffraction, for Figure 22, there are several efficiency maxima at each energy due to the different θ_B of each ring of the lens.
The off-axis and off-energy efficiency of the lens can be understood from Fig. 23. For an incident photon with a direction (ψ_p, ϕ_p), the change in angle with respect to the crystalline planes is $\approx \psi_p$ for those crystals with an azimuthal angle $\phi_c \approx \phi_p$. According to the Bragg relation, a larger energy $E_\circ + \Delta E$ is focused. The change in angle with respect to the crystalline planes is $\approx (-\psi_p)$ for those crystals with an azimuthal angle $\phi_c \approx \phi_p + 180°$. According to the Bragg relation, a smaller energy $E_\circ - \Delta E$ is focused. For 500 keV and the Ge (111)-planes, a ψ_p of 1 arc second leads to an energy offset of the efficiency maximum by 1.4 keV.

4.5.2 Response to Extended Emission

For an extended source with a spectral and spatial flux distribution $f(\psi_s, \phi_s, E)$, the flux diffracted by the lens for energy E, assuming the lens optical axis is (ψ_0, ϕ_0) and that the lens is tuned to energy E_0, is given by

$$F(\psi_0, \phi_0, E) = \int d\psi_s \int d\phi_s \bar{\varepsilon}(\sqrt{(\psi_0 - \psi_s)^2 + (\phi_0 - \phi_s)^2}, E|\phi_0, \psi_0, E_0) f(\psi_s, \phi_s, E) \tag{31}$$

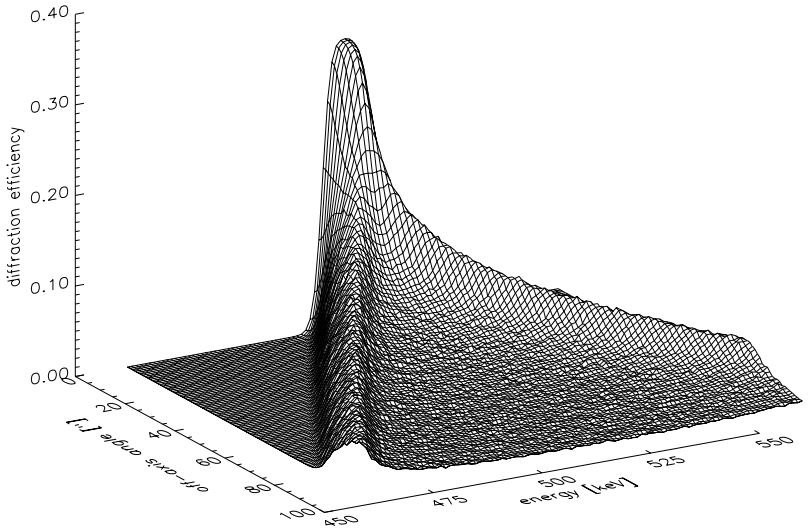

Figure 21: *The diffraction efficiency as a function of off-axis angle and off-energy averaged over the innermost (111) ring. The calculations are for 1-cm-thick crystals with a 10 arc second mosaic width.*

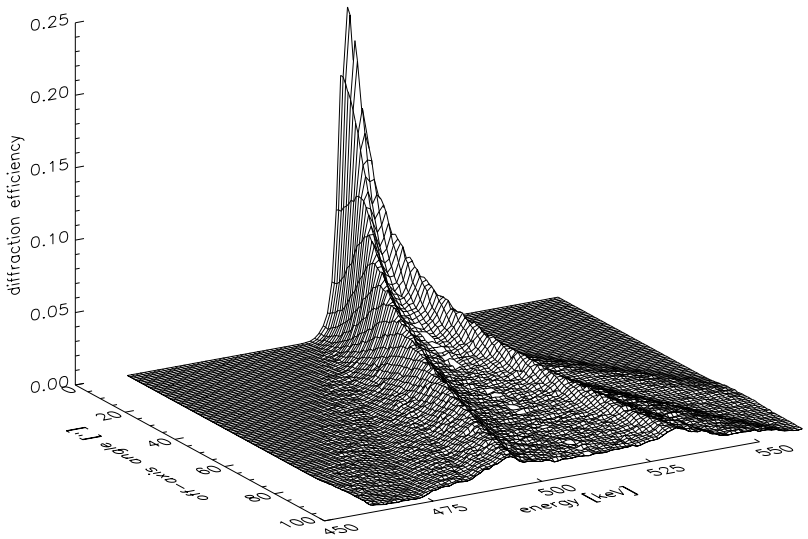

Figure 22: *The diffraction efficiency as a function of off-axis angle and off-energy averaged over the entire lens. The calculations are for an 8-ring lens at 500 keV, and 1-cm-thick crystals with a 10 arc second mosaic width.*

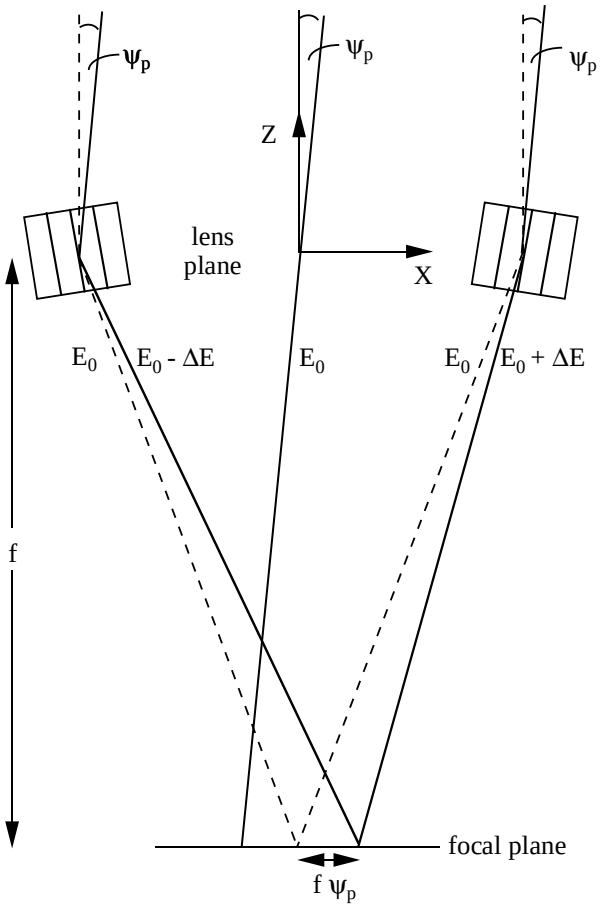

Figure 23: *For an incident photon with a direction (ψ_p, ϕ_p), the change in angle with respect to the crystalline planes is $\approx \psi_p$ for those crystals with an azimuthal angle $\phi_c \approx \phi_p$. According to the Bragg relation, a larger energy $E_\circ + \Delta E$ is focused. The change in angle with respect to the crystalline planes is $\approx (-\psi_p)$ for those crystals with an azimuthal angle $\phi_c \approx \phi_p + 180°$. According to the Bragg relation, a smaller energy $E_\circ - \Delta E$ is focused. For both cases, the position of the diffracted photons in the focal plane is offset by the $f\psi_p$ with f as the focal length.*

with the integral extending over the entire source region. Calculations of the lens response to extended emission are shown in sections 5.2 and 6.1.

4.5.3 Angular Resolution

The angular resolution of a crystal lens telescope is determined by the mosaic width of the crystals, as well as the energy resolution of the detector. The angular resolution is calculated by integrating the diffraction efficiency vs. off-axis angle curves over the assumed energy resolution of the detector. The resulting curves are generally non-Gaussian. The angular resolution is here defined as the

region (diameter) which contains 78% of the integral of the efficiency vs. angle curve. This is motivated from the FWHM of the Gaussian distribution, which contains 78% of the integral of the curve. The angular resolution is shown in Fig. 24 for crystals with a 10 arc sec mosaic width and for an energy resolution of 1 keV and 2 keV. The effect of the detector energy resolution decreases with the square of the working energy of the telescope. At high energies, the angular resolution is determined by the mosaic width. The angular resolution shown is for photons at the working energy of the telescope.

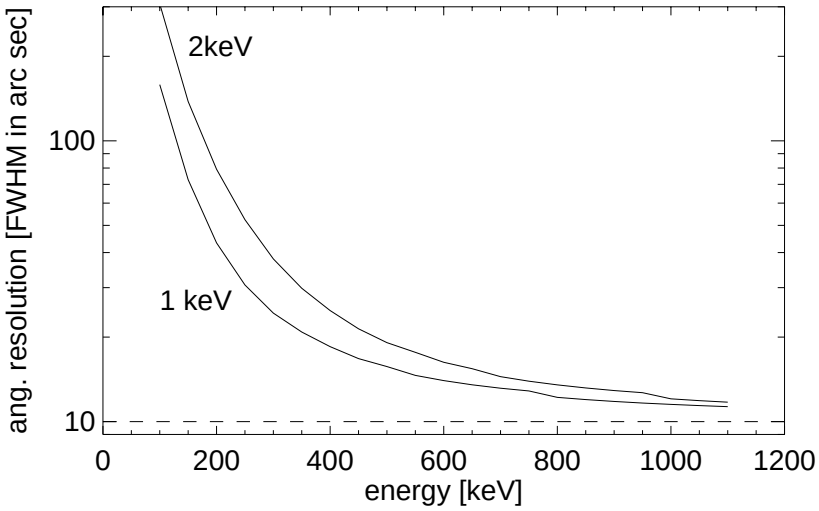

Figure 24: *The angular resolution of the crystal lens telescope is shown as a function of energy for crystals with a mosaic width of 10 arc seconds and for an energy resolution of 1 keV and of 2 keV. The dotted line at 10 arc seconds shows the contribution of the mosaic width of the crystals to the angular resolution.*

4.5.4 Focal Plane Image

The gamma-ray lens focuses monochromatic radiation of energy E_0 parallel to the optical axis to a spot in the focal plane whose intensity distribution depends on the crystal size. For a single crystal, the image in the focal plane is a rectangle of the same size as the crystal surface seen by the incoming radiation. Due to the small Bragg angles, this is identical to the size of the crystal. For one ring of the lens containing N_{crys} crystals, the image in the focal plane is the superposition of N_{crys} rectangles, each rotated by an angle $(n2\pi)/N_{crys}$ with $0 \leq n < N_{crys}$. For a multi-ring lens with several hundred crystals, the focal spot can be well approximated by a radial intensity distribution calculated by letting the above discrete rotation steps become infinitely small. For a

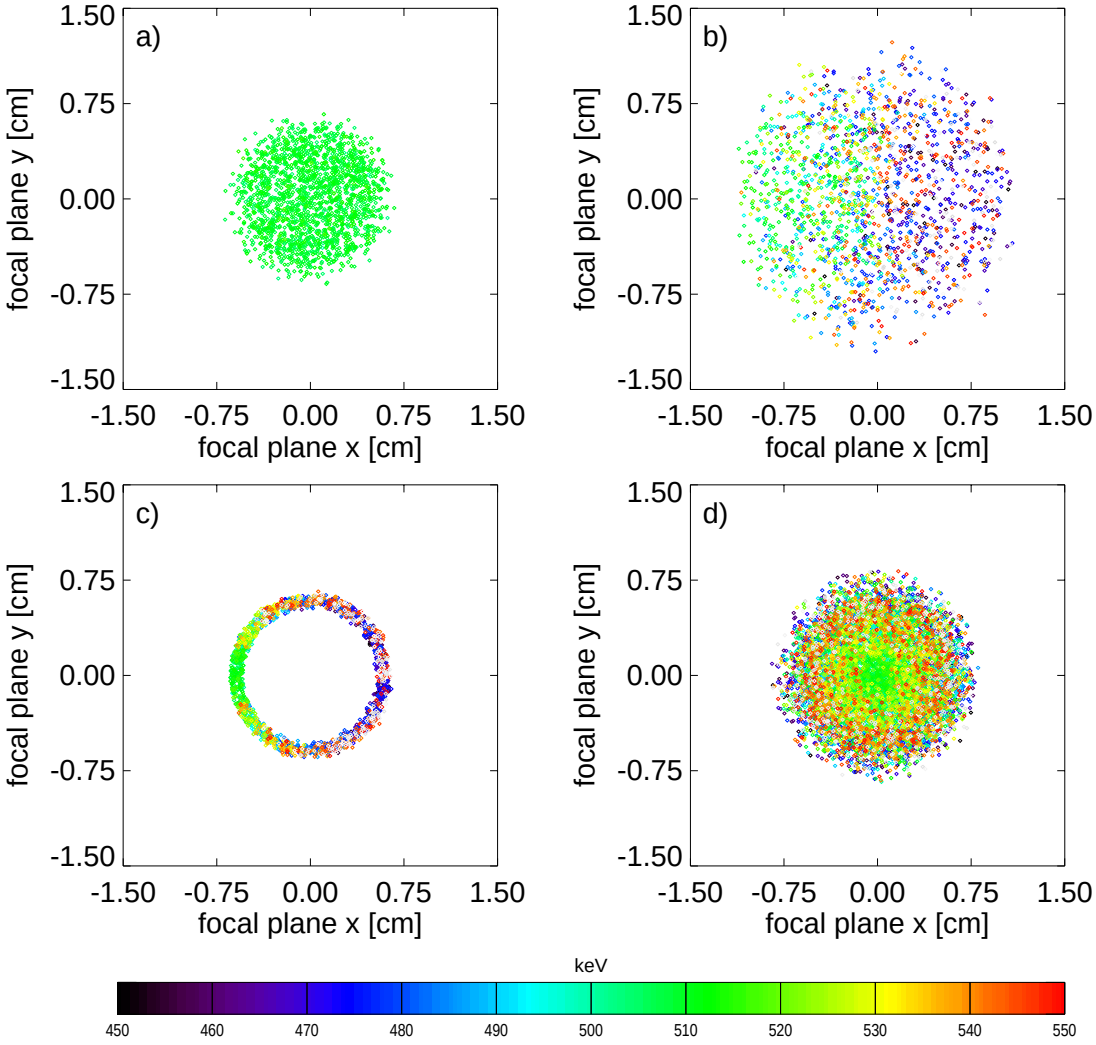

Figure 25: *The focal plane image for different continuum sources is shown. Only points with diffraction efficiencies > 1% are plotted. All plots are calculated for an 8-ring lens and crystals with a 10 arc second mosaic width, and for a working energy E_0 of 511 keV. The color-scales correspond to energies between 450 and 550 keV. The upper two plots show the focal plane image for a flat-spectrum continuum point source aligned with the optical axis (plot a) and offset by an angle of 150 arc seconds in the +x-direction (plot b). The crystal surface is 1 × 1 cm^2. The lower two plots show the focal plane image for crystals with a 0.1 × 0.1 cm^2 surface. Plot c is the image for a continuum point source offset by an angle of 150 arc seconds in the +x-direction (the same as the upper right plot). Plot d is the image of an extended continuum source with a flat source distribution over a radius of 150 arc seconds.*

crystal with a surface of length x_0 and width y_0 and $x_0 > y_0$, the normalized radial intensity $I(r)$ of the focal spot is 1 for $r_1 \leq y_0$ and 0 for $r_2 > \sqrt{(x_0/2)^2 + (y_0/2)^2}$. For the region between r_1 and r_2 one obtains

$$
\begin{aligned}
I(r) &= \frac{90^o - \phi_1 - \phi_2}{90^o} \\
\phi_1 &= \begin{cases} acos(x_0/r) & : \quad x_0/r < 1 \\ 0 & : \quad else \end{cases} \\
\phi_2 &= \begin{cases} acos(y_0/r) & : \quad y_0/r < 1 \\ 90^o - atg(y_0/x_0) & : \quad else \end{cases}
\end{aligned}
\tag{32}
$$

For crystals with a 1 cm^2 surface and sides of 1 × 1 (square), $\sqrt{1/2} \times 2\sqrt{1/2}$ (rectangle with sides 1:2) and $\sqrt{1/3} \times 3\sqrt{1/3}$ (rectangle with sides 1:3), 50% of the radiation is contained within 0.56 cm (square), 0.54 cm (rectangle 1:2), and 0.51 cm (rectangle 1:3), and 90% of the radiation is contained within 0.81 cm (square), 1.17 cm (rectangle 1:2), and 1.38 cm (rectangle 1:3). In order to minimize the size of the detector element and thus the background, and nonetheless contain most of the focal spot intensity in one element, square crystals are better than rectangular crystals.

Fig. 25 shows the focal plane image for a flat-spectrum continuum point source aligned with the optical axis of the lens (plot a) and offset by an angle of 150 arc seconds (plot b). These plots assume crystals with a 1 cm^2 surface. Plot c is for the same configuration as plot b, but for crystals with a 0.01 cm^2 surface. Plot d shows the focal plane image for a flat-spectrum continuum source with a flat source distribution over a radius of 150 arc seconds.

These calculation are for $E_\circ = 511$ keV and crystals with 10 arc second mosaic width. The calculation ray-traced photons with a random energy distribution, and only photons with diffraction efficiencies > 1% are depicted. The color-scales correspond to energies between 450 and 550 keV.

As shown in Fig. 22, the efficiency for an off-axis source is spread out over a larger energy range, with two pronounced maxima at energies $E_0 \pm \Delta E$. From Fig. 23, one can see that the photons with energies around $E_0 \pm \Delta E$ form a roughly circular focal spot, but with the centroid displaced in the $+x$-direction by $f\psi_p$, whereas the focal spot of photons with energy E_0 is displaced in the $-x$-direction by $f\psi_p$. This is seen in plots b and c of Fig. 25.

In Fig. 25, plot d, the photons with energy $E_0 \pm \Delta E$ focused by the lens mainly come from a ring of the source with an angle $\psi_p = \theta_B(\Delta E/E)$ to the optical axis. These photons are imaged onto a ring in the image plane with a mean radius of $\psi_p f = \theta_B(\Delta E/E)f$ and centered on the the optical axis. The width of the ring in the source that contributes to the focused flux increases with increasing mosaic width of the crystals, the width of the ring in the image plane depends both on the crystal size as well as the mosaic width. Thus, with increasing distance from the image center, the deviation of the photon energy from E_0 as well as the off-axis angle of the source photons contributing to the focused flux increases.

4.5.5 Calculation of the Line Sensitivity

The performance of a crystal lens telescope can be quantified by the gamma-ray line sensitivity, i.e., the minimal detectable flux. For gamma-ray line observations, the expression for the sensitivity is [89]

$$s_n = \frac{n}{2X}\left[n + \sqrt{n^2 + 4N}\right] \approx \frac{n\sqrt{N}}{X}\left[1 + \frac{n}{\sqrt{4N}} + \frac{n^2}{8N}\right] \tag{33}$$

with n as the number of standard deviations, N as the total background counts, and X as the exposure in units of $\mathrm{cm}^2\mathrm{s}$. For a background dominated observation, typically the case for observations at gamma-ray energies, the sensitivity can be approximated by $f_n \approx n\sqrt{N}/X$. For a crystal lens telescope, the background counts and the source counts are comparable, so that the full equation needs to be used.
The background is

$$N = \phi_{bg}\Delta E_{bg} V_{bg} t \tag{34}$$

with ϕ_{bg} as the background count rate in counts cm^{-3} s^{-1} keV^{-1}, ΔE_{bg} is the background energy width, V_{bg} is the effective background volume, and t is the observation time. ΔE_{bg} is either the detector resolution, the energy bandpass of the lens, or the line width, depending on the relative widths and the type of sensitivity (narrow or broad line) being calculated.
For the exposure, one obtains

$$X = A_{lens} t \sum_{ring} \frac{N_{ring}}{\Delta E_{line}} \int_{\Delta E} \varepsilon_{ring}(E) I_{line}(E) dE \tag{35}$$

A_{lens} is the geometric lens area, ΔE_{line} is the line width, $I_{line}(E)$ is the normalized intensity distribution of the line, N_{ring} is the number of crystals in a ring, and the sum is over all rings. The so-called narrow line sensitivity assumes a line width narrower than the detector resolution. Sensitivity calculations are presented in sections 5.1 and 6.2.

4.6 Broadband Concentrators

Several configurations for broadband concentrators have been proposed. Lund [94] describes a concentrator with crystals arranged in an Archimedian spiral or hexagonal pattern. At each energy, a band of crystals with a central radius $r = \frac{f\lambda}{d}$ contribute to the focused flux (f is the focal length, d is the crystalline plane spacing, λ is the wavelength). The crystals with small radii focus the high energy radiation (small Bragg angle), whereas the crystals at large radii focus low energy radiation (large Bragg angle). Melone et al. [95] describe a number of broadband concentrators, including a ring concentrator, a spherical concentrator, a focusing spherical concentrator and a focusing paraboloidal concentrator. A schematic of the focusing spherical concentrator is shown in Fig. 26. The diffraction planes lie along the radial direction of a sphere with radius R, and photons with incoming direction parallel to the optical axis are focused at the focal length $f = R$. The lens uses asymmetrically-cut crystals, meaning that the crystal surface is not aligned with the diffraction planes.

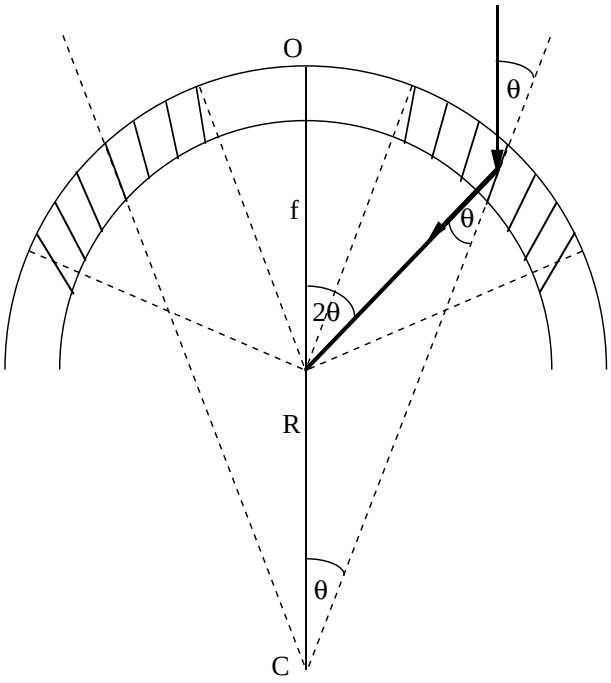

Figure 26: *A focusing spherical-zone broadband concentrator is shown (adapted from [95]). The crystals are used in asymmetric Laue geometry. The diffraction planes lie along the radial directions of the sphere with center C and radius $2R$. Photons parallel to the optical axis $\overline{OC}$ are diffracted to the center of the sphere at the focal length $f = R$. The Bragg angle θ increases with increasing distance from the optical axis, meaning that high energies are focused by crystals close to the optical axis, and low energies by crystals far from the optical axis.*

Broadband concentrators obviously have the advantage of a large energy bandpass (up to many hundreds of keV). However, only a small fraction of the concentrator area focuses radiation at any one energy, compromising the signal to noise increase which can be achieved with such instruments. Furthermore, the radial configuration of the crystals always leads to small geometric areas at high energies, which correspond to the inner radii. The geometric area thus decreases with energy as $1/E$.

5 Potential of a Crystal Lens Telescope

In the preceding chapter, the characteristics of a crystal lens telescope were described. This chapter shows the potential of such an instrument based on these characteristics. The most outstanding advantage of a crystal lens telescope is the sensitivity increase compared with existing and next-generation instruments (section 5.1). The angular resolution of less than an arc-minute allows an intensity mapping of slightly extended sources (section 5.2). The potential of a the crystal lens telescope for spectroscopy, such as the measurement of line profiles from expanding supernova and nova shells, is discussed in section 5.3. Finally, the use of a crystal lens telescope as a polarimeter is mentioned (section 5.4).

5.1 Sensitivity

The line sensitivity of a gamma-ray instrument, defined as the limiting source flux s_n in units of photons cm^{-2} s^{-1}, can be approximated for a background-dominated observation to

$$s_n = n\frac{\sqrt{2\phi_{bg}V_{bg}}}{A_\gamma\sqrt{t}} \tag{36}$$

with n as the significance in units of Gaussian σ, ϕ_{bg} as the background flux in counts cm^{-3} s^{-1} keV^{-1}, V_{bg} as the effective background volume, A_γ as the effective area for gamma rays, and t as the observation time. Assuming fixed n and t, the sensitivity can be increased by increasing A_γ or by decreasing ϕ_{bg} and V_{bg}. The effective area for gamma-rays A_γ can be increased either by increasing the detector area or the detector efficiency, which both tend to increase the detector mass. For space-based astronomy, weight limitations essentially restrict the increase of A_γ. The background flux ϕ_{bg} can be reduced by optimizing the detector shielding, minimizing the amount of material surrounding the detector inside the shield, and by optimizing the choice of detector material and other material inside the shield. For narrow lines, increasing the detector energy resolution will decrease the amount of background counts over the width of the line. Much progress has been made in recent years in understanding and minimizing detector background, but there are intrinsic limits due to the flux going through the telescope aperture and the necessity to have material surrounding the detector. The reduction of the effective background volume V_{bg} has inherent limitations due to the gamma ray attenuation length, which is typically a few cm (e.g., 2.9 cm for Ge and 2.0 cm for BGO for 1 MeV gamma rays).

In summary, large gains in sensitivity using traditional instrumentation seem difficult to achieve. The concept of the crystal lens telescope overcomes this impasse by dramatically decreasing the effective background volume V_{bg} by concentrating the gamma-ray flux coming from a large gamma-ray detection area onto a small detector.

The flux concentration decouples the gamma-ray detection area, i.e., the lens area, and the background-inducing detection volume, i.e., the volume of the detector in the focal plane. This leads to the signal-to-noise (S/N)-ratio increasing linearly with the lens area, whereas for non-focusing detectors the S/N-ratio only increases roughly with the square root of the detector area. Due to the fact that the lens area can be made quite large (several thousand cm^2) and the background

volume quite small (several tens of cm^3), a crystal lens telescope achieves a dramatic improvement in sensitivity compared with existing and next-generation gamma-ray detectors.

The potential of a spaceborne crystal lens telescope in terms of line sensitivity is shown in Fig. 27. The line sensitivity depends on the width of the line, as the background count rate over the energy width of the line increases with line width. For supernovae and novae, the line width can be expressed in terms of an expansion velocity, with $\frac{\Delta E}{E} = \frac{v}{c}$.

Fig. 27a shows an estimate of the 3 σ line sensitivity for narrow and slightly broadened lines as a function of energy for line widths (FWHM) of $\frac{\Delta E}{E} = 0.003$, $\frac{\Delta E}{E} = 0.007$, $\frac{\Delta E}{E} = 0.017$, and of $\frac{\Delta E}{E} = 0.033$. Assuming an optically thin expanding envelope, these line widths correspond to expansion velocities of $\pm$500 km/s, $\pm$1000 km/s, $\pm$2500 km/s, and $\pm$5000 km/s. The observation time is 10^6 s. Narrow line sensitivities of $2 \cdot 10^{-7}$ ph cm^{-2} s^{-1} to $1 \cdot 10^{-6}$ ph cm^{-2} s^{-1} over the energy range of 200 keV to 1300 keV seem achievable with a lens of moderate size. This energy region covers many of the astrophysically interesting line features, inluding the 511 keV positron annihilation line, ^{56}Co lines at 847 keV and 1238 keV, ^{44}Ti at 1156 keV, and ^{22}Na at 1275 keV. In principle (neglecting the problem of long focal lengths), the energy range can be extended to higher energies to include the ^{26}Al line at 1809 keV and the n-p capture line at 2223 keV, with sensitivities of $2 \cdot 10^{-6}$ ph/cm^2 s (1809 keV) and $4 \cdot 10^{-6}$ ph/cm^2 s (2223) keV for narrow lines. The sensitivity shown in Fig. 27 is a factor of 10 improvement over INTEGRAL (to be launched in 2001) and almost a factor of 100 improvement over OSSE (aboard CGRO, launched 1991).

As shown below, these sensitivies imply the detection of several supernovae of type Ia per year in the 847 keV line, and the likely detection of a type Ib or Ic supernova during a mission lifetime of a few years. The detection of a supernova of type II is unlikely. Novae could be detected out to 2.0 to 2.7 kpc in the 478 keV line of the ^{7}Be decay for the case of a CO nova, and could be detected out to 1.7 kpc in the 1275 keV line of the ^{22}Na decay for the case of a ONe nova. To date, there has only been one marginal detection of gamma-ray lines from a supernova of type Ia, and no line detections from novae. For comparison, the expected detection rate of the INTEGRAL spectrometer to ba launched 2001 is about 1 supernova of type Ia per year and 0.2 supernovae of type Ib/c per year. CO and ONe novae should be detectable out to 0.5 kpc.

The sensitivity calculations of Fig. 27 assume the lens configuration of Table 4, with 544 Ge crystals, mostly with a 2 $\times$ 2 cm^2 surface, and a total lens area of 2676 cm^2. The mosaic width is assumed to be 10 arc seconds, and the crystals are 1.5 cm thick. The focal length would be 16.6 m at 511 keV, increasing linearly with energy. At 2000 keV, the focal length would be 65 m. Such long focal lengths may be difficult to realize. The calculations assume a detector made up of ^{70}Ge-enriched HPGe elements with a 3 $\times$ 3 cm^2 surface and a length of 7 cm. The detector efficiency was assumed to be 80 % at 200 keV, 54 % at 511 keV, and 39 % at 1000 keV. The background was estimated using a fit to the GRIS continuum background spectrum for a ^{70}Ge-enriched HPGe detector during a balloon flight in Alice Springs in 1992. The background was reduced by a factor of five to roughly account for the lower mass of the anticoincidence shield needed, which reduces the contribution of secondary particles. This gives a background estimate of $9.42 \cdot 10^{-4} \left(\frac{E}{100keV}\right)^{-1.054}$ counts cm^{-3} s^{-1} keV^{-1}. This is of course a very crude estimate and emphasizes the need for detailed Monte Carlo background simulations. Background simulations

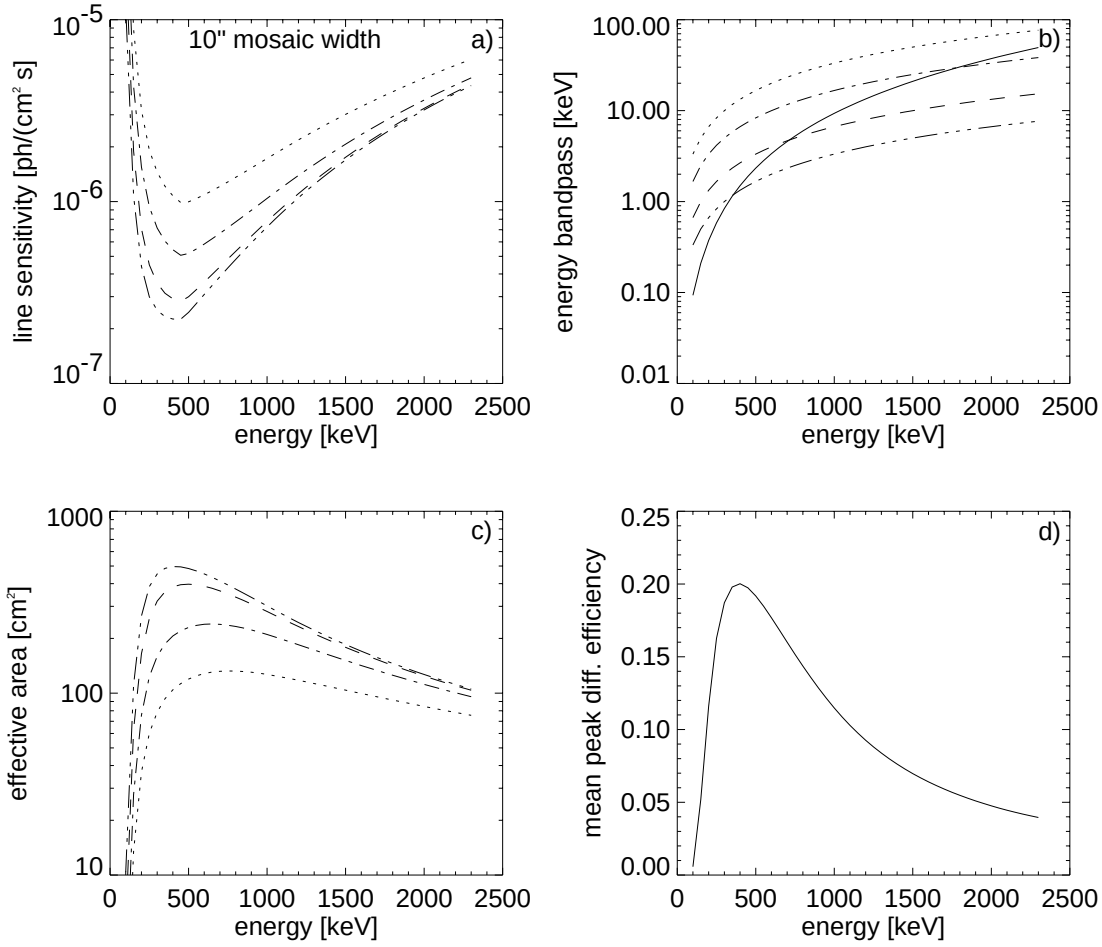

Figure 27: *Plot a shows the 3 σ line sensitivity as a function of energy. The curves are for line widths (FWHM) of $\frac{\Delta E}{E} = 0.003$ (long dash-short dashes), $\frac{\Delta E}{E} = 0.007$ (long dashes), $\frac{\Delta E}{E} = 0.017$ (long dash-short dash), and of $\frac{\Delta E}{E} = 0.033$ (short dashes). Assuming an optically thin expanding envelope, these line widths correspond to expansion velocities of ±500 km/s, ±1000 km/s, ±2500 km/s, and ±5000 km/s. The curves are for a 10^6 s observation time, and a detector efficiency of 80% at 200 keV, 54% at 511 keV, and 39% at 1000 keV. The background was crudely estimated using the GRIS [70] Ge-enriched HPGe detector background spectrum from a balloon-flight from Alice Springs in 1992, reduced by a factor of five. Plot b shows the energy bandpass of the lens (solid line) and the line width corresponding to expansion velocities of ±500 km/s (long dash-short dashes), ±1000 km/s (long dashes), ±2500 km/s (long dash-short dash), and ±5000 km/s (short dashes). Plot c shows the effective area, i.e., the lens area times the diffraction efficiency averaged over the energy bandwidth of the line, as a function of energy for the four different line widths. Plot d shows the mean peak diffraction efficiency as a function of energy.*

were however not carried out in the framework of this thesis.

ring number	reflection plane (hkl)	crystal surface cm^2	radius [cm]	number of crystals	area cm^2	peak eff. at 500 keV
1	111	2 × 2	11.9	28	112	0.26
2	220	2 × 2	19.4	52	208	0.26
3	311	1 × 2	22.8	60	120	0.24
4	400	2 × 2	27.5	76	304	0.25
5	331	0.5 × 2	30.0	84	84	0.19
6	422	2 × 2	33.7	94	376	0.23
7	440	2 × 2	38.9	110	440	0.20
8	622	2 × 2	45.6	122	488	0.16
9	800	2 × 2	55.0	136	544	0.11

Table 4: *The configuration of the lens used to calculate the curves of Fig. 27 is shown. Listed are the crystalline planes, the ring radii, the peak diffraction efficiencies at 500 keV, and the crystal size and the number of crystals for each ring.*

Fig. 27b compares the energy bandwidth of the lens to a line width corresponding to expansion velocities of ±500 km/s, ±1000 km/s, ±2500 km/s, and ±5000 km/s. The energy bandpass of this lens is 2.3 keV at 500 keV, 6.7 keV at 847 keV, and 11.4 keV at 1238 keV. For a given expansion velocity, the line width in keV grows linearly with energy, whereas the energy bandpass of the lens grows with the square of energy. The energy bandpass of the lens becomes larger than line widths of ±500 km/s above 380 keV and larger than line widths of ±1000 km/s above 760 keV.
It is important to note that the true line widths for supernova and nova ejecta can deviate substantially from the expansion velocities assumed here. The ejected particles have a velocity distribution, the opacity of the envelope varies as a function of time, Compton-scattering causes a red-shift in energy, and particles can be reaccelerated by shocks in the expanding envelope.
Fig. 27c shows the effective area of the lens, defined as the lens area multiplied with the diffraction efficiency averaged over the line width. The effective area for narrow ($\frac{\Delta E}{E} = 0.003$) lines is 480 cm^2 at 500 keV and 230 cm^2 at 1250 keV. This implies that the 3 σ detection comprises between 130 and 460 photons superimposed on an underlying background of 200 to 1000 counts. The small number of detected photons is due to the limited area of the lens. One would need to increase the lens area and thus the weight of the instrument to increase the number of detected photons.
The line sensitivities of Fig. 27a can be used to estimate the number of supernovae that can be seen in gamma-ray lines. The number of supernovae of type Ia, Ib/c and II detectable per year as a function of telescope sensitivity has been estimated by Timmes and Woosley [96] using the Sternberg Astronomical Supernova Catalog and the Asiago Supernova Catalog. Following these authors, the crystal lens telescope could detect ca. 2.7 supernovae Ia per year, and ca. 0.4 supernovae Ib/c per year in the 847 keV line. These values are for a 3 σ detection during a 10^6 s observation time.

To date, there has only been one marginal detection of ^{56}Co from a supernova of type Ia, namely 1991T [24]. With a crystal lens telescope, the production of ^{56}Ni in SN Ia could quickly be verified. With a sample of several positive detections of ^{56}Co from SN Ia, the variation of the mass of ^{56}Ni produced in the explosion can be studied, and compared with variations in the lightcurve at other wavelengths. The measurement of line profiles can make it possible to deduce deviations from a spherically symmetric explosion. This may help to clarify the explosion mechanism, and to better use SNIa as distance indicators.

Thermonuclear runaways on accreting white dwarfs are at the origin of nova explosions. Typical accretion rates are $2 \cdot 10^{-10}$ M$_\odot$/yr, typical ejecta masses are 10^{-5} M$_\odot$. The amount of radioactive nuclei produced in the nova explosion depends strongly on the initial composition of the nova envelope. Models assume some enrichment with material of the white dwarf core. Depending on the initial composition, the models differentiate between CO novae and ONe or ONeMg novae. Gomez-Gomar et al. [97] have calculated gamma-ray yields for both types of novae. For CO novae, the ^{7}Be decay with a line energy of 478 keV and a decay time of τ=77 d could be observable. At 1 kpc distance, the models predict a peak line flux at 478 keV of $1.4 - 2.6 \cdot 10^{-6}$ ph cm^{-2} s^{-1} and a line width of 3 to 7 keV. This corresponds to expansion velocities of 2000 km/s to 4500 km/s. For ONe novae, the models predict a peak line flux at 1275 keV of $4 - 6 \cdot 10^{-6}$ ph cm^{-2} s^{-1} and a line width of 20 keV. Both CO and ONe novae give rise to strong 511 keV line emission during the first week after explosion, but the rapid decline of the emission makes this radiation difficult to observe.

Using the above sensitivities for a crystal lens telescope, CO novae could be detected out to 2.0 to 2.7 kpc (radius) in the 478 keV line of the ^{7}Be decay, and ONe novae could be detected out to 1.6 to 2.0 kpc in the 1275 keV line of the ^{22}Na decay. This should be compared to the estimated Galactic nova rate of ca. 35 yr^{-1} [98], [99], [100]. The rate of nova detections within a given radius around the sun is rather insensitive to the underlying nova distribution model, and is $\approx$0.5/yr for a radius of 2 kpc and $\approx$1.2/yr for a radius of 3 kpc [101].

5.2 Imaging

Existing and next-generation coded aperture mask telescopes achieve a resolution of $>$ 10 arc minutes at energies of several hundred keV. A crystal lens telescope achieves an angular resolution of less than an arc minute. The resolution is determined by the mosaic width of the crystals, as well as the energy resolution of the detector (see section 4.5.3). The effect of the energy resolution decreases with energy: for crystals with a 10 arc sec mosaic width and a 1 keV (2 keV) detector resolution, the angular resolution is 43 (79) arc sec at 200 keV, 16 (19) arc sec at 511 keV, and 12 (13) arc sec at 847 keV.

This unprecented angular resolution at gamma-ray energies can be used to map the intensity of slightly extended sources.

The crystal lens telescope could contribute to our understanding of the origin of annihilation radiation from the Galactic center by looking for 511 keV radiation from the Galactic black hole candidate 1E1740-294, and by mapping the intensity within the source. From the observation of the 511 keV line flux from the direction of the Galactic center by numerous balloon-borne and

satellite experiments [15], evidence for a time variability by as much as $2 \cdot 10^{-3}$ photons cm^{-2} s^{-1} as well as a correlation of the flux with the field of view was found. These results could be interpreted as the emission being due to a time-variable compact source and a steady-state diffuse galactic component [16].

The SIGMA telescope detected a strong transient feature in the energy range 300 keV to 700 keV during 1E1740-294 observations in October 1990 and in September 1992. This feature can be interpreted as broadened and redshifted pair annihilation radiation coming from a hot ($\approx 5 \cdot 10^8$ K) plasma. VLA observations at radio wavelengths discovered radio jets whose lobes are aligned with a central, time-variable radio source [102]. The extent of the radio jets is about 1 arc minute. IRAM infrared observations show a high-density molecular cloud in the direction of the gamma-ray source, and velocity measurements make it likely that 1E1740-294 is embedded in this cloud [103]. This led to a model where 1E1740-294 emits bursts of e^+e^--pairs. These partly annihilate close to the disk, giving rise to the broadened, redshifted annihilation radiation seen by SIGMA, and are partly accelerated in the jets, where they could be slowed down in the high-density molecular cloud, giving rise to a time-variable narrow 511 keV line. Ramaty, Leventhal, Chan and Lingenfelter [104] predict a narrow and variable 511 keV line emission from a region as large as 20 arc seconds and a flux of 10^{-4} to 10^{-3} ph cm^{-2} s^{-1}. It is important to note that recent measurements of the 6.4 keV Fe line from 1E1740-294 with ASCA [105] imply a column density 5 to 15 times lower than the line-of-sight column density derived from other means, perhaps indicating that the bulk of absorbing gas may be located in front of the source.

More recent observations with OSSE find no time-variability of annihilation radiation from the direction of the Galactic center. Purcell et al. give a 3 σ upper limit on persistant 511 keV emission from 1E1740-294 of $1.6 \cdot 10^{-4}$ ph cm^{-2} s^{-1} [17]. If 1E1740-294 is contributing to the 511 keV line flux, a crystal lens telescope could determine the flux as well as localizing the annihilation regions.

A simulation of an observation of 1E1740-294 at 511 keV is shown in Fig. 28. The simulation assumes the telescope configuration of section 5.1, a line flux of 10^{-4} ph cm^{-2} s^{-1}, a line width $<$ 2 keV, and a 10^6 s observation time. The background at 511 keV is estimated to $4 \cdot 10^{-5}$ cts cm^{-3} s^{-1} keV^{-1} in a manner similar to section 5.1, dividing the GRIS ^{70}Ge-enriched 511 keV line flux by a factor of five. The detector resolution was assumed to be 2 keV, the angular resolution (FWHM) is 19 arc seconds. The simulation assumes that the telescope optical axis sweeps over a source region of 60 by 60 arc seconds with equal exposure. The simulation was carried out assuming a source consisting of 2 Gaussians with a 2 arc sec FWHM and separated by 40 arc seconds (Fig. 28 a,b,c), and for a single Gaussian with a 2 arc sec width (Fig. 28 a,b,c). Fig. 28a shows a contour map of the assumed source distribution of the 2 Gaussians, Fig. 28b shows the source distribution convolved with the telescope response, and Fig. 28c shows the reconstructed image for the observation parameters cited above. Fig. 28d shows the reconstructed image assuming a single Gaussian as the source distribution.

Beyond the Galactic microquasars 1E1740-294 and GRS 1758-258, the intensity mapping of line emission from young supernova remnants and from novae is possible with a crystal lens telescope. A mapping of the ^{44}Ti emission of the $\approx$ 300 year old supernova remnant Cas A (a few arc minutes

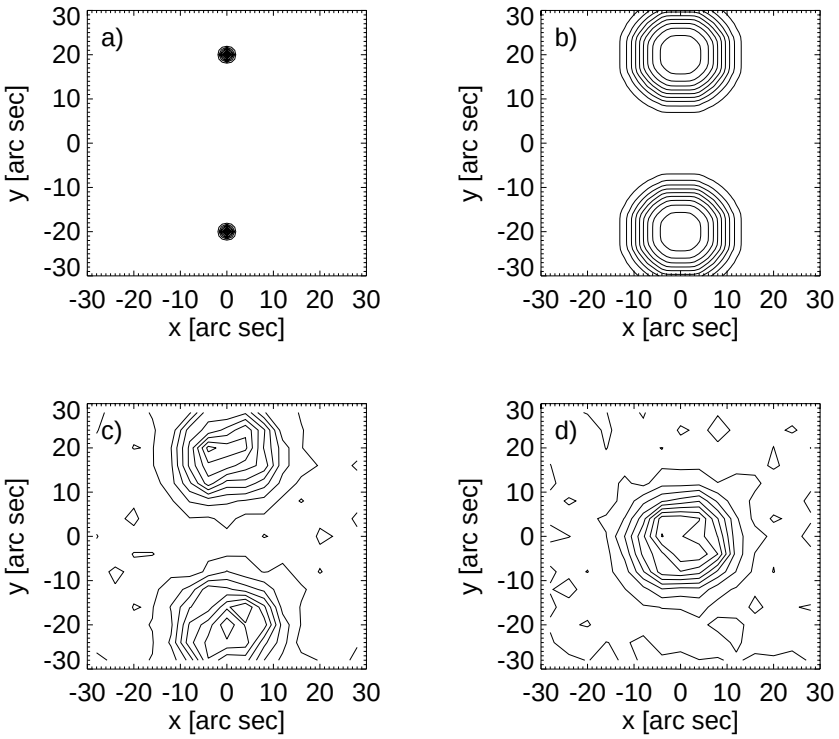

Figure 28: *A simulation of an observation of the source 1E1740-294 is shown. Plot a) shows the assumed source distribution consisting of 2 Gaussians with a 2 arc sec FWHM and separated by 40 arc seconds. Plot b) shows the crystal lens telescope response assuming infinite photon statistics. Plot c) shows the contour map obtained for a source line flux of* 10^{-4} *ph* cm^{-2} s^{-1}*, a line energy of 511 keV, a line width* < 2 *keV, a background of* $4 \cdot 10^{-5}$ *cts* cm^{-3} s^{-1} keV^{-1} *and a* 10^6 *s observation time. Plot d) shows the contour map obtained for the same conditions assuming that the source consists of a single source modeled as a Gaussian with 2 arc sec FWHM. These simulations assume that the telescope optical axis sweeps over the region of 60* $\times$ *60 arc sec shown in the plots with equal exposure. The pointing of the telescope as well as the crystal orientation was assumed to be perfect.*

extent), as well as the ^{26}Al emission from the Vela supernova remnant (a few degrees extent), both detected with COMPTEL, are possible with a crystal lens telescope.

5.3 Spectroscopy

The energy resolution of the crystal lens telescope is determined by the energy resolution of the focal plane detector. Assuming an array of HPGe detectors, an energy resolution of $\approx$ 2 keV at 1 MeV can be achieved. This resolution allows the measurement of gamma-ray line profiles. Supernova and nova line profiles are decisive for understanding the dynamics of the explosion and the ejecta. First attempts at measuring line profiles were made for the ^{56}Co lines from SN1987A using several balloon-borne HPGe spectrometers, but the results are inconsistent and suffer from low detection significances [19].

A crystal lens telescope is an ideal instrument for the measurement of line profiles. Assuming the lens configuration of section 5.1, the flux of the ^{56}Co lines from the type Ia supernova 1991T as measured by COMPTEL [24], and a line width (FWHM) of 15 keV, the crystal lens telescope would detect the source with a significance of 8.2 σ for the 847 keV line and 4.2 σ for the 1238 keV line for a 1-day ON-observation. The effective area of 230 cm^2 (847 keV) and 180 cm^2 (1238 keV) would lead to a detected flux of 1050 photons (847 keV) and 550 photons (1238 keV) for the same 1-day ON-observation. The signal-to-background ratio would be 0.14 (847 keV) and 0.07 (1238 keV). The contribution of the source continuum flux to the background can presumably be neglected. Thus, line profiles could be established on an almost daily basis, and, especially if observed at early times after the explosion, could contribute greatly to our understanding of the explosion dynamics.

It is important to note that the measurement of line profiles implies that the lens reponse curve is known. This implies an independent method of verifying the crystal orientations. This may be possible by observing a bright gamma-ray source such as the Crab, or by optical means, e.g. verifying the crystal orientations via laser reflections off the face of the crystals. For lines broader than the energy window of the lens, the line profiles can be established by scanning over energy, however at the cost of sensitivity.

At low energies, where the energy bandpass of the lens is less than the detector energy resolution, the energy resolution of the crystal lens telescope is determined by the lens. Assuming the lens configuration of section 5.1, this is the case below $\approx$ 350 keV. By changing the orientation of the lens crystals in small steps, scans in energy can be performed with an energy resolution superior to that achievable with current technology. At 200 keV, the energy bandpass is 0.35 keV (FWHM), at 150 keV, it is 0.2 keV. However, as the background energy window is determined by the detector energy resolution, these measurements have a reduced signal-to-noise ratio.

5.4 Polarimetry

Astronomical measurement of polarization have never been performed at energies $>$ 10 keV. Gamma-ray production mechanisms such as synchrotron radiation and Bremsstrahlung can lead to polarized emission, and high polarization levels are expected from some gamma-ray sources (up

to 80% for the Crab pulsar, and up to 75% for solar flares) [106].
The diffraction efficiency depends on the angle between the polarization angle of the electric field and the diffraction plane χ. The diffraction efficiency ε as a function of χ is modulated by a factor of [107] [108]

$$\varepsilon(\chi) \propto sin^2\chi + cos^2\chi cos^2 2\theta_b. \tag{37}$$

with θ_b as the Bragg angle. The variation of ε decreases with decreasing Bragg angle, and is small at high energies. For Ge (440), the relative modulation $(\varepsilon(\chi) - \varepsilon(90°))/\varepsilon(90°)$ is 95% at 10 keV , 6.1% at 50 keV, and 1.5% at 100 keV. Unfortunately, the effect of polarization is negligeable for the working energy range of the crystal lens telescope.
The crystal lens telescope can be used as a polarimeter if the focal plane detector is able to measure polarization. Polarimeters rely on the fact that the differential Compton cross-section depends on the polarization of the incident photon. With E_0 as the incident photon energy, E as the scattered photon energy, η as the scattering angle, the differential cross section is

$$\frac{d\sigma}{d\omega} = \frac{1}{2} r_0^2 \frac{E^2}{E_0^2} \left(\frac{E}{E_0} + \frac{E_0}{E} - 2sin^2\eta cos^2\phi \right). \tag{38}$$

ϕ is the azimuthal angle of the scattered photon with respect to the electric vector of the incident photon. The modulation factor is defined as

$$Q(\theta) = \frac{N_\perp(\eta) - N_\parallel(\eta)}{N_\perp(\eta) + N_\parallel(\eta)} \tag{39}$$

where $N_\perp(\eta)$ is the detected count rate of the scattered gamma-rays in a direction perpendicular to the electric vector of the incident gamma-ray (i.e., $\phi = 90°$), and $N_\parallel(\eta)$ is the detected count rate in a direction parallel to the electric vector (i.e., $\phi = 0°$).
Assuming a liquid xenon TPC as the focal plane detector, modulation factors of 0.5 at 200 keV to 0.4 at 1000 keV are achievable [109]. Segmented HPGe detectors or Ge strip detectors as the focal plane detector would also make polarimetric measurements possible.

6 Simulations of a Spaceborne Crystal Lens Telescope

The preceding chapter outlined the scientific potential of a space-based crystal lens telescope. This chapter uses the formulas derived in chapter 4 to calculate the performance of a balloon-borne (section 6.1) and a satellite-based (section 6.2) crystal lens telescope. For a balloon-borne lens, configuration criteria are derived. The effect of atmospheric absorption is discussed. The performance of a balloon-borne crystal lens telescope for an observation of the Crab at 170 keV as well as for an observation of 1E1740-294 is discussed. The simulation of the balloon-borne observation of 1E1740-294 is based on work prior to this thesis (von Ballmoos and Smither 1994 [118]). Finally, this chapter compares different configurations of a satellite-based crystal lens telescope.

6.1 A Balloon-Borne Crystal Lens Telescope

A balloon flight of a crystal lens telescope is an important intermediary step between laboratory tests and a satellite-based instrument. The objectives of a first balloon flight are technological as well as scientific. The technological aim is to demonstrate the principle of focusing gamma-rays from a point source at infinity and to demonstrate the dramatic improvement in signal-to-noise ratio inherent to the detection technique. Scientific objectives and the simulation of possible results will be discussed below.

6.1.1 Configuration

Compared to laboratory tests, a balloon flight presents several technological challenges. For the observation of a point source, the lens needs to be pointed with a precision better than the mosaic width of the crystals, i.e., less than one arc minute. The position of the optical axis of the lens should be known to a few arc seconds. This makes it necessary to maintain the alignment of a star sensor with the optical axis of the lens to a precision of a few arc seconds. Furthermore, the lens needs to be thermalized to avoid a "detuning" of the lens crystals.
For a first flight of a balloon-borne instrument, the following design criteria are important:

- The telescope structure needs to be lightweight and low in power consumption.
- A short (few m) focal length is preferable. The effective lens area should be sufficiently large to ensure a good signal-to-noise ratio, and a sufficient number of detected photons. This implies an observation at a low energy.
- Typical balloon flight durations are several hours. Thus, it seems reasonable to fly a lens with fixed crystal orientations, i.e., to only observe at one energy. This makes a rigid structure connecting the detector and the lens possible. In order to demonstrate the tunability, one could motorize one ring of crystals, even though the detector-lens distance is fixed.
- Due to its role as a precursor to a spaceborne instrument, the balloon-borne configuration should not be too different from the space-borne configuration.

For the observational objectives, the following criteria are important:

- The source should be bright enough to ensure a significant detection even for short flight durations, and to demonstrate the high signal-to-noise ratio achievable with such an instrument.

- The observation of a source with known strength would enable a direct determination of the diffraction efficiency of the lens.

- As the main scientific objective of such an instrument is in gamma-ray line astronomy, the observation of a gamma-ray line would be preferable.

For the following, the crystal lens telescope is assumed to consist of an 8-ring, 600 1×1 cm^2-surface crystal lens. The detector is the existing 3×3-element HPGe detector used in the ground-based tests of the 1st prototype lens. The single elements are n-type coaxial detectors, with a 1.5×1.5 cm^2 surface area, and a length of 4 cm.

6.1.2 Candidate Sources

Candidate sources include the observation of radioactive ^{44}Ti in Cas A via the hard X-ray lines at 68 and 78 keV, and the observation of the Crab continuum at a low gamma-ray energy.
The 1156 keV emission from the $\approx$ 300 year old supernova remnant Cas A was detected by COMPTEL with a line flux of $4.8 \pm 0.9 \cdot 10^{-5}$ ph cm^{-2} s^{-1} and a Doppler-broadening of 24 ± 9 keV [112]. This observation could be confirmed by the detection of the hard X-ray emission arising from the same decay.
The energy bandpass of the lens increases with the square of energy, and depends on the mosaic width of the crystals. For the observation of Cass A, one would need crystals with a mosaic width of around 1 degree. Ge would not be suited as a crystal material, due to its high attenutation coefficient, and the large mosaic width needed. This makes the lens configuration rather different from the space-borne instrument. Furthermore, the high background at low energies as well as the low line flux make a significant detection difficult for a short-duration flight.
Another candidate source is the observation of the Crab pulsar and nebula. The Crab is undoubtably one of the best-studies objects in the gamma-ray sky, and can be regarded as a "standard candle" for gamma-ray astronomy. The Crab is a bright, young supernova remnant, with steady emission, and no persistant line features. The brightness and the well-known source spectrum are advantageous for the observation with the crystal lens telescope. The lack of gamma-ray lines make the choice of working energy somewhat arbitrary. For the following calculations, a working energy of 170 keV was assumed. This energy limits the focal length to less than 3 m (f=2.76 m), and does not coincide with a known background line. Furthermore, 170 keV is the energy of Compton-backscattered annihilation radiation, and 511 keV photons are observed in third-order diffraction.

6.1.3 Simulation of the Observation of the Crab Nebula and Pulsar

In this section, the detected flux from the Crab nebula and pulsar during a balloon flight observation at 170 keV is calculated, the background is estimated, and the effect of an extended nebula on the detected flux is discussed.

The Crab flux has been measured by numerous groups. For the following,

$$\phi = 37.5 \cdot 10^{-5} \left(\frac{E}{100keV} \right)^{-2.18} + 7.6 \cdot 10^{-5} \left(\frac{E}{100keV} \right)^{-2.04} \tag{40}$$

taken from [111] is used. The first term is the nebula flux, the second term is the phase-averaged pulsar flux. The total flux at 170 keV is $1.44 \cdot 10^{-4}$ ph cm^{-2} s^{-1} keV^{-1}, with the nebula contributing 82% of the total flux.

In contrast to satellite-based experiments, the effect of the residual atmosphere in attenuating the gamma-ray source flux is not negligeable. The atmospheric depth τ in g cm^{-2} is the integral of the density over the residual atmosphere, and depends on height and zenith angle. For small zenith angles, one obtains

$$\tau = \frac{1}{\cos z} \int_h^\infty \rho(h) dh \tag{41}$$

with z as the zenith angle, ρ as the density, and h as the height. The gamma-ray attenuation $I/I_\circ$ as a function of atmospheric depth and energy is then

$$\frac{I}{I_\circ} = e^{-\mu(E)\tau} \tag{42}$$

with $\mu(E)$ as the gamma-ray attenuation coefficient.

The zenith angle of the source varies as the source sweeps across the sky. As a function of hour angle, the altitude a is [110]

$$\sin a = \sin\delta \sin\phi + \cos\delta \cos h \cos\phi \tag{43}$$

with h as the hour angle, and ϕ as the observation latitude.

$I/I_\circ$ is plotted as a function of time around the upper culmination for atmospheric depths of 3, 5, 7, and 9 g cm^{-2} in Fig. 29. The plot assumes a geographic latitude of 45°, and the Crab declination of $\delta = 22°$. One can see that the balloon altitude plays a decisive role, and that the maximal observation window is about 8 h for this geographic latitude.

The number of detected photons is

$$N_\gamma = \phi \cdot A \cdot \sum \left(\int \varepsilon(E) dE \right) \cdot \varepsilon_{air} \cdot \varepsilon_{det} \cdot t \tag{44}$$

with ϕ as the Crab flux, A as the total crystal area, $\int \varepsilon(E) dE$ as the rocking curve integral, ε_{det} as the detector efficiency, ε_{air} as the air absorption averaged over the observation time t, and the sum being over all lens crystals.

The full peak energy efficiency of the 3 × 3-element HPGe detector has been measured [113]. At 170 keV, the average efficiency is 73%, assuming an active volume of 8.3 cm^3 per element. This

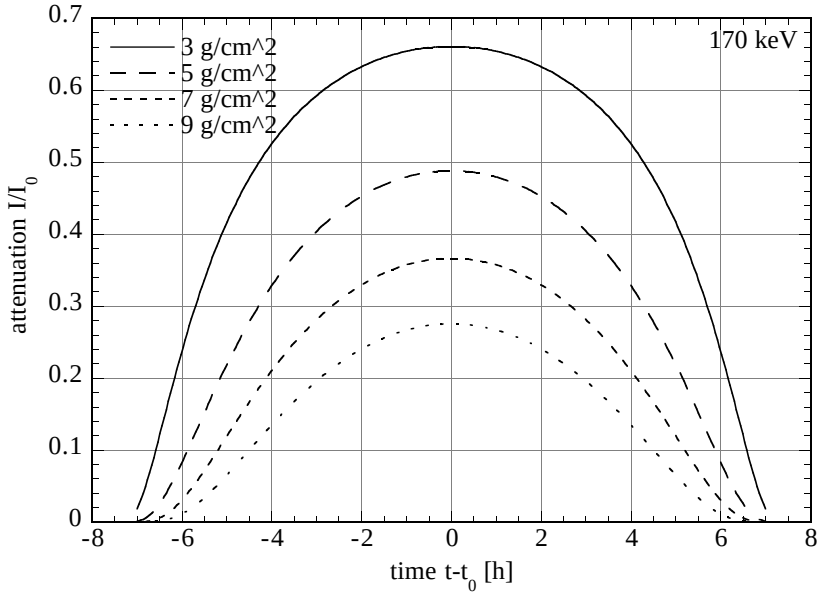

Figure 29: *The atmospheric attenutation of 170 keV photons, $I/I_\circ$, as a function of time around the upper culmination for atmospheric depths of 3, 5, 7, and 9 g cm^{-2}. The curves are for a geographic latitude of* 45°*, and the Crab declination of* $\delta = 22°$.

efficiency includes multiple-element events. The percentage of multiple events depends on position: 16% for the central element, 11% for the side elements, and 6% for the corner elements.

The total number of estimated photons as a function of the observation time is shown in Fig. 30 for Si and Ge crystals and mosaic widths of 30 and 60 arc seconds. The time window is assumed to be symmetric around the upper culmination. The calculations assume an optimal crystal thickness (1.7 to 2.7 cm for Si, and 0.4 to 0.7 cm for Ge, depending on ring). The atmospheric depth if 5 g cm^{-2}. One can see that the number of detected photons first rises linearly, and then flattens off for large observation times. This is due to the detected flux decreasing with increasing zenith angle of the source due to the air absorption ε_{air}. For a 6-hour duration balloon flight and Ge crystals with a 60 arc second mosaic width, the number of detected photons would be 60 photons from the pulsar, and 260 photons from the nebula. For 30 arc second Ge crystals, the number of detected photons would be 40 photons from the pulsar and 190 from the nebula. These numbers assume a point source.

The number of background counts for the observation time t is

$$N_{bg} = \phi_{bg} \cdot V_{bg} \cdot \Delta E \cdot t \tag{45}$$

with the background flux ϕ_{bg} in cts cm^{-3} s^{-1} keV^{-1}, V_{bg} is the effective background volume, ΔE is the energy bandwidth. For the observation of a continuum source, ΔE is either the energy bandpass of the lens or the detector energy resolution, whichever is larger. Crystals with a 30 arc

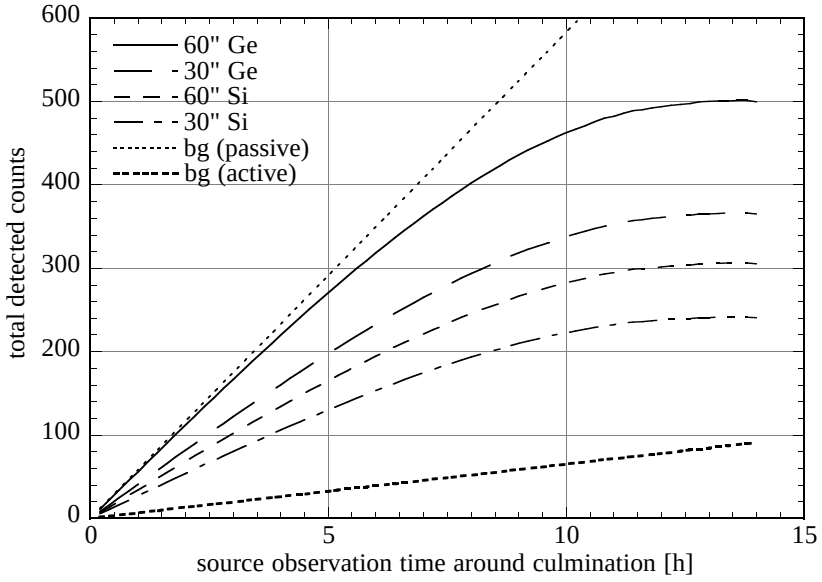

Figure 30: *The total number of detected photons from the Crab as a function of the observation time for Ge and Si crystals with 30 arc second and 60 arc second mosaic width. The observation time is assumed symmetric around the upper culmination. The curves are for a geographic latitude of* $45°$*, and assume an atmospheric depth of 5 g cm*$^{-2}$*. The Crab nebula is assumed to be a point source. Also plotted are the estimated number of background counts for an active shield (30 mm BGO) and a passive shield (10 mm BGO), assuming an effective background volume of 2 detector elements, and a detector energy resolution of 2.0 keV.*

second mosaic width correspond to an energy bandpass of the lens of 1 keV at 170 keV. Here, a detector energy resolution of 2.0 keV was assumed. V_{bg} was set to the volume of two detector elements, 18 cm^3.

The background flux at 170 keV has been estimated for different shield configurations using the GEANT package by Pierre Jean at CESR. An active BGO shield would give a background flux of $5 \cdot 10^{-5} - 4 \cdot 10^{-4}$ cts cm^{-3} s^{-1} keV^{-1}, a passive BGO shield would give a background flux of $4 - 5 \cdot 10^{-4}$ cts cm^{-3} s^{-1} keV^{-1}, depending on the BGO thickness. For the following calculations, background fluxes of $4.5 \cdot 10^{-4}$ cts cm^{-3} s^{-1} keV^{-1} (passive 10-mm-thick BGO shield) and $5 \cdot 10^{-5}$ cts cm^{-3} s^{-1} keV^{-1} (active 30-mm-thick BGO shield) are assumed.

The number of background counts assuming these fluxes are also shown in Fig. 30. One can see that the ratio of signal counts to background counts is generally larger than one: for 60 arc second Ge crystals, the ratio is 8.7 (1.0), for 30 arc sec Ge crystals, the ratio is 6.3 (0.7), with the values in parenthesis corresponding to the passive shield flux.

Even for short observation times, the Crab is detected with a large significance: for a 1-hour ON-source observation of the Crab, the significance is 6.8 σ (4.2 σ) for Ge crystals with a 60 arc second

mosaic width, and 5.6 σ (3.3 σ) for Ge crystals with a 30 arc second mosaic width. The values in parenthesis again correspond to the passive shield background flux.

In the following, the effect of the nebular size on the detected flux will be discussed. In the optical, the nebula has an extent of 4 × 7 arc minutes. The nebular size is seen to decrease with increasing photon energy. ROSAT has imaged the nebula in the 0.4 to 2 keV energy band [114], the emission is concentrated in a torus aligned with the equatorial plane of the pulsar with a size of 2 arc minutes. In the hard X-ray band, the nebular size was measured by lunar occulations [115]. The size in the 1-50 keV band can be described by

$$FWHM(arcsec) = 52.5 \pm 3.3 \cdot \left(\frac{E}{1keV}\right)^{-0.13\pm0.04} . \quad (46)$$

Extrapolation of this formula to 170 keV would give a source size of 27 arc seconds. 2-dimensional maps of the Crab were obtained using a scanning modulation collimator in the 22-64 keV energy range [116]. These measurements show an asymmetry in the intensity distribution, the nebula being more extended along the optical minor axis, and a major (minor) axis of 63 (25) arc seconds. Aschenbach and Brinkman propose a model [117] whereby the nebular size should not shrink below 10 arc seconds with increasing energy. This is the size of the cavity surrounding the pulsar. At the outer edge of the cavity, the supersonic wind emanating from the pulsar is terminated by the shock boundary. Beyond the shock, the particle motions become randomized, leading to intense synchrotron emission.

In section 4.5, the imaging properties of the telescope for off-axis and off-energy photons were discussed. The angular resolution depends on the mosaic width as well as the energy resolution of the detector (section 4.5.3). The contribution of the detector energy resolution decreases roughly with $E^{-3/2}$, but is important at 170 keV.

At this energy, the angular resolution is 61 arc sec (FWHM) for crystals with a 30 arc second mosaic width and ΔE = 1 keV, and 98 arc sec for ΔE = 2 keV. At 511 keV, the angular uncertainty assuming a 1 keV (2 keV) detector energy resolution would be 32 arc sec (34 arc sec), so that the angular resolution is almost fully determined by the mosaic width.

With sufficient photon statistics, it is nonetheless possible to precisely determine the angular extent of the source. This is shown in Fig. 31, where the detected nebular flux is plotted as a function of the angle between the source centroid and the optical axis of the telescope for various source sizes. The detected flux is integrated over the detector energy resolution assumed to be 1.5 keV. The source was modeled as a 2-dimensional Gaussian intensity distribution, with a FWHM of 1, 20, 40, and 80 arc seconds. Also shown in Fig 31 is the detected flux for a point source, but with "detuned" crystals, i.e., crystals whose orientation is slightly offset from the nominal orientation due to mechanical or thermal instabilities. This curve was calculated assigning a random offset following a Gaussian probability function with a FWHM of 50 arc seconds to each crystal (the δ in equation 29). One can see that "detuned" crystals mimic an extended source. As the position on the detector for a focused energy is different for a "detuned" crystal, one could in principle differentiate between the two cases. However, a detuning of 60 arc seconds would only result in a 1 mm offset on the detector. Using a standard Ge detector, it seems necessary to verify the crystal orientations via other means.

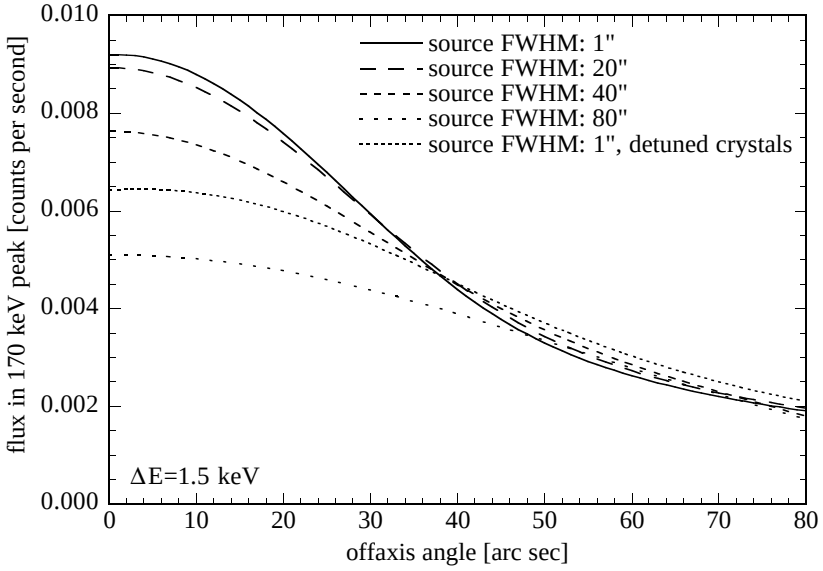

Figure 31: *The detected flux in couns per second from the Crab nebula is plotted as a function of the angle of the optical axis of the telescope with the source center. The curves are for source sizes (FWHM) of 1, 20, 40 and 80 arc seconds, and assume a 2-dimensional Gaussian source intensity distribution. The curves are for Ge crystals with a mosaic width of 30 arc seconds. Also shown is the curve for a point source (FWHM of 1 arc second), but with "detuned" crystals. The crystals were detuned randomly following a Gaussian distribution with a FWHM of 50 arc seconds.*

The expected results of the observation of the Crab at 170 keV during a first balloon flight can be summarized as follows:

- A significant detection of the Crab is to be expected even for short-duration flights. For Ge crystals with 30 (60) arc second mosaic width, an atmospheric depth of 5 g cm^{-2}, and a geographic latitude of 45°, using a background estimate based on the GEANT code gives a significance of $\sigma = 5.6 \cdot \sqrt{t[h]}$ ($\sigma = 6.8 \cdot \sqrt{t[h]}$) for an active BGO shield, and a significance of $\sigma = 3.3 \cdot \sqrt{t[h]}$ ($\sigma = 4.2 \cdot \sqrt{t[h]}$) for a passive BGO shield

- For Ge crystals with 30 (60) arc second mosaic width, the energy bandpass of the lens is 1 keV (2keV), the detected flux around culmination is 40 (55) photons/hour. The ratio of source photons to background counts is 6.3 (8.7) for an active BGO shield, and 0.7 (1.0) for a passive BGO shield.

- The extent of the nebula will be difficult to determine, due to the large mosaic width of the crystals and the additional angular uncertainty arising from the detector energy resolution as well as limited photon statistics. Using crystals with 30 arc sec mosaic width and assuming a detector resolution of 1.5 keV, the angular uncertainty (FWHM) is 80 arc seconds. The

effect of the detector resolution decreases with energy, at 511 keV the angular uncertainty would only be 33 arc seconds.

6.1.4 Simulation of the Observation of 1E1740-294 at 511 keV

The characteristics and scientific potential of the prototype crystal lens telescope working at 511 keV during a stratospheric balloon flight are described in von Ballmoos and Smither 1994 [118]. The crystal lens configuration is identical to the ground-based prototype described in section 4.4, however, non-wedged crystals with a larger mosaic width (about 10 arc seconds FWHM) are used. The crystals are oriented to focus 511 keV gamma-rays from infinity, and they are fixed in inclination. The 3 × 3 HPGe detector used in the ground-based tests is at the focal plane of the crystal lens.

The diffraction efficiency at 511 keV as well as the effective background volume of the 3 × 3 HPGe detector have been measured [92]. The efficiency of the central detector is 25% at 511 keV, including single-element events and multi-element events with an energy deposit in the central element. The background rejection is 79% compared with a detector of the same active volume as the 9 elements. This translates into an effective background volume of 16 cm^3, whereas the active volume for gamma-rays is 81 cm^3.

The characteristics of this crystal lens telescope have been recalculated using the Darwin model and are summarized in Table 5. The mosaic width of the crystals is assumed to be 10 arc seconds. The energy bandpass for radiation parallel to the optical axis is 3 keV. However, for off-axis radiation, a larger band of energies is focused with decreased efficiency (see section 4.5). This leads to an energy band of 511 ± 150 keV being focused for an off-axis angle of 0.15°, which corresponds to the size of the detector. The narrow line sensitivity is $4.6 \cdot 10^{-5}$ ph cm^{-2} s^{-1} for a 20 h observation (Australia) or a 5 day observation (Antarctica). The simulations assume a background energy window of 2 keV. The background flux was estimated taking the background rate of the 511 keV line of two balloon-borne Ge spectrometers with active BGO shielding, namely the HEXAGONE '89 launch from Alice Springs and the HIREGS '92 launch from Antarctica. This gives background estimates of $2.3 \cdot 10^{-4}$ counts cm^{-3} s^{-1} for Australia, and $1.3 \cdot 10^{-3}$ counts cm^{-3} s^{-1} for Antarctica. The scientific interest of an observation of 1E1740-294 is described in section 5.2. To date, no 511 keV emission from 1E1740-294 has been detected, with a 3 σ upper limit on persistant 511 keV emission of $1.6 \cdot 10^{-4}$ ph cm^{-2} s^{-1} [17]. This is three times higher than the sensitivity limit of the above simulation, justifying a balloon-borne observation of 1E1740-294 with a crystal lens telescope.

CRYSTAL LENS	
• diffracting medium	600 1 cm^3 Ge crystals in 8 rings, 10 arc sec mosaic width
• diameter of frame	45 cm
• focal length	8.29 m
• diameter of focal spot for monochromatic (511 keV) radiation	1.1 cm FWHM
• field-of-view for monochromatic (511 keV) radiation	16 arc sec
• field-of-view for continuum radiation	0.15 degree (determined by the detector size)
• energy bandwidth (on-axis)	3.0 keV FWHM
• energy bandwidth (off-axis)	511 keV ± 150 keV (determined by the detector size)
• mean peak diffraction efficiency for monochromatic (511 keV) radiation	23%
• effective collection area for monochromatic (511 keV) radiation	138 cm^2
DETECTOR MATRIX	
• detector type	9 HPGe n-type coaxial detectors, each element 1.5 × 1.5 × 4 cm^3
• energy resolution	≈2 keV at 511 keV
• total detecting volume	81 cm^3
• total detector area	20.25 cm^2
• efficiency at 511 keV	25%
POINTING REQUIREMENTS	
• absolute pointing	optical axis of the lens ≤ 5 arc sec
• telescope axis pointing	5 arc minutes
• lens weight to be stabilized	≈ 50 kg
• telescope weight	≈ 250 kg
TELESCOPE SYSTEM	
• system effective area for monochromatic (511 keV) radiation	35 cm^2
• angular resolution	19 arc sec (FWHM)
• energy range (on-axis)	511 ± 1.5 keV
• energy range (0.15 degree off-axis, edge of the detector)	511 ± 150 keV
• energy resolution	≈ 2 keV
• effective background volume (focal spot in central pixel)	16 cm^3
• 3σ narrow line sensitivity	$4.6 \cdot 10^{-5}$ ph cm^{-2} s^{-1} (20 h observation [Australia] or 5 day observation [Antarctica])

Table 5: *Characteristics of a balloon-borne crystal lens telescope working at 511 keV are summarized.*

6.2 A Satellite-Based Crystal Lens Telescope

6.2.1 Comparison Criteria

The aim of this section is to compare several possible configurations for a satellite-based tunable crystal lens telescope. The emphasis will be on the optimization of the lens and detector configuration, without considering the practical difficulties of the realization, such as long focal lengths, the orientation and motorization of up to thousands of crystals. The comparison assumes identical focal lengths and identical energy bandpasses of the telescopes.
In order to compare different configurations, criteria need to be found to quantify the performance of the instrument. For narrow bandpass concentrators, the focused flux depends on the line width. For lines much narrower than the energy bandpass of the lens, the focused flux is proportional to the lens area A_{lens} times the peak reflectivity ε_{max} summed over all crystals:

$$N_{det} \propto A_{lens} \cdot \sum_n \varepsilon_{max,n} \equiv A_{eff,narrow} \tag{47}$$

For broadened lines and for continuum radiation, the detected flux is proportional to the diffraction efficiency averaged over the energy bandpass of the lens and summed over all crystals:

$$N_{det} \propto A_{lens} \cdot \frac{1}{\Delta E} \sum_n \int_{\Delta E} \varepsilon(E) dE \equiv A_{eff,broad} \tag{48}$$

where ΔE is the energy bandpass (FWHM) of the lens. The effective area $A_{eff,broad}$ will always be smaller than $A_{eff,narrow}$. For lines broader than the energy bandpass of the lens, the detected flux is reduced by the line fraction within the energy window.
The formulas for the calculation of line sensitivities were shown in section 4.5.5. For the limiting case of a background-free observation, the sensitivity is inversely proportional to the effective area

$$s_n \propto A_{eff}^{-1} \qquad (N_{bg} \longrightarrow 0) \tag{49}$$

For a background-dominated observation, the sensitivity is proportional to the square root of the effective background volume V_{eff} and the background energy window ΔE_{bg} divided by the effective area A_{eff}:

$$s_n \propto \frac{\sqrt{V_{eff} \Delta E_{bg}}}{A_{eff}} \qquad (N_{bg} \gg N_\gamma) \tag{50}$$

For narrow lines, the background energy window is the detector resolution. For broad lines, the background energy window is equal to the line width or the energy bandpass of the lens for the case that the line is broader than the lens bandpass.
For a space-based crystal lens telescope, the number of background counts is generally comparable to the number of source counts at the sensitivity limit, meaning that the sensitivity lies between the two cases of equations 49 and 50. Below, both the effective area A_{eff} as well as $A_{eff}/\sqrt{V_{eff} \Delta E_{bg}}$ of the telescope configurations will be compared.

6.2.2 Comparison of Possible Configurations

Three possible lens configurations are summarized in Tables 6, 7, and 8. All three lens configurations have a focal length of 16.6 m at 511 keV, increasing linearly with energy. The working energy

range is 200 to 1300 keV, the crystal material is Ge. All crystals focus the same energy, and need to be motorized to be able to change energy. The energy bandpass of the three lenses is fixed to 7 keV at 511 keV, increasing with the square of energy. At 1238 keV, the energy window is 40 keV. The focal plane detector is assumed to have an energy resolution of 2 keV.

Lens I (Table 6) is a 15-ring lens. The inner 8 rings are identical with the prototype lens configuration, but are at twice the radii, and thus have 4 times as much crystal area. The lens contains 2380 2 × 4 cm^2 surface crystals, the total area is 19040 cm^2. The weight of the crystals would be 320 kg. The lens diameter is 2 m. The mosaic width of the crystals increases for the outer rings, so that the energy bandpass is the same for all rings.

Lens II (Table 7) is the 11-ring lens described in [119]. The five inner rings are optimized for high energies (1.5-cm-thick crystals), the outer six rings are optimized for low energies (0.5-cm-thick crystals). The lens contains 723 2 × 2 cm^2 surface crystals, the total area is 2892 cm^2. The lens diameter is 0.8 m. The lens uses two detectors, detector 1 is at half the distance of detector 2. Detector 1 detects photons diffracted in 1st order from the 5 inner rings and photons diffracted in 2nd order from the 6 outer rings. Detector 2 detects photons diffracted in 1st order from the outer 6 rings. The 1st and 2nd order are for the same energy E_0, in contrast to the higher order diffraction of $n \cdot E_0$, which is diffracted by all crystals.

Lens III (Table 8) is a 16-ring lens with 2 detectors, using the same principle as Lens II. The inner 8 rings focus photons onto detector 1, whereas the outer 8 rings focus photons onto detector 2 in 1st order and onto detector 1 in 2nd order diffraction. The lens contains 2402 1 × 2 cm^2 surface crystals (excepting 3 rings with 1 × 1 and 1 × 1.5 cm^2 crystals), the total area is 4760 cm^2. The lens diameter is 1 m. The crystal thicknesses are optimized to maximize the rocking curve integral averaged over the working energy range of the telescope.

The effective areas are compared in Fig. 32a. For each configuration, two curves are shown: the upper curve is the narrow-line effective area (equation 47), the lower curve is the effective area averaged over the energy bandpass of the lens (equation 48). The energy bandpass as a function of energy is shown in Fig. 32b.

One can see that the 16-ring, 2-detector lens (lens III) has at most a factor of 2.1 less effective area than the 15-ring, 1-detector lens (lens I), even though the crystal area is 4 times smaller. This is due to the fact that the outer rings of lens I are rather inefficient: a crystal of the outermost ring is a factor of 75 less efficient than a crystal of the innermost ring. The 2-detector lenses (II and III) avoid this problem and have better mean efficiency. At 500 keV, the mean efficiency if 3.7% for lens I, 9.5% for lens II, and 10.5% for lens III. None of the configurations exceed an effective area of 1000 cm^2.

Also shown in Fig. 32 is $A_{eff}/\sqrt{V_{bg}\Delta E_{bg}}$ in units of $cm^{0.5}$ $keV^{-0.5}$ for narrow lines (plot c) and averaged over the energy bandpass of the lens (plot d). $(A_{eff}/\sqrt{V_{bg}\Delta E_{bg}})^{-1}$ is proportional to the telescope sensitivity and thus proportional to the minimal detectable flux. The effective background volume and energy resolution were estimated for a focal plane detector made up of HPGe elements, with the size of a single element equal to the focal spot size (90% intensity). The background volume was set to 2 elements, assuming an element length of 7 cm. The energy resolution was set to 3 keV at 1300 keV, increasing with the square root of the energy.

total crystal area: 19040 cm^2 number of crystals: 2380
lens diameter: 2 m focal spot (90% intensity): 3.31 cm
working energy: 200-1300 keV energy bandpass at 511 keV: 7 keV

ring number	radius [cm]	reflection plane [hkl]	T [cm]	crystal size [cm]	number of crystals	mosaic width ["]	ε_{max} (511 keV)
1	11.8	1 1 1	1.2	2 × 4	28	10	0.30
2	19.4	2 2 0	1.2	2 × 4	52	17	0.28
3	27.4	4 0 0	1.7	2 × 4	76	24	0.19
4	33.6	4 2 2	2.0	2 × 4	94	30	0.13
5	38.8	4 4 0	2.2	2 × 4	110	31	0.07
6	43.4	6 2 0	2.4	2 × 4	122	34	0.09
7	47.6	4 4 4	2.5	2 × 4	136	38	0.06
8	54.8	8 0 0	2.7	2 × 4	158	42	0.05
9	61.4	8 4 0	2.8	2 × 4	176	48	0.03
10	67.2	8 4 4	2.9	2 × 4	194	54	0.02
11	75.2	10 4 2	2.9	2 × 4	218	59	0.01
12	80.0	10 6 0	3.0	2 × 4	232	66	0.008
13	84.6	12 2 2	3.0	2 × 4	246	70	0.006
14	89.0	10 8 2	3.0	2 × 4	260	74	0.005
15	95.2	8 8 8	3.0	2 × 4	278	78	0.004

Table 6: *The configuration of lens I. The radius of each ring, the Miller indices of the diffraction plane, the crystal thickness T, the crystal surface area, the number of crystals per ring, the mosaic width in arc sec, and the peak efficiency at 511 keV are listed for each ring.*

Configurations II and III have smaller focal spots, but use two detectors. Nonetheless, the effective background volume of the 2-detector lenses is about half that of lens I. Below 230 keV, the energy bandpass of the lens is less than the detector energy resolution. This together with the large attenuation coefficient in the crystals at low energies lead to a poor sensitivity below 200 keV and limits the working energy range of the telescope.

total crystal area: 2892 cm^2 number of crystals: 723
lens diameter: 0.8 m focal spot (90% intensity): 1.62 cm
working energy: 200-1300 keV crystal mosaic width: 24 arc seconds

ring number	radius [cm]	reflection plane [hkl]	T [cm]	crystal size [cm]	number of crystals	ε_{max} (511 keV)	2nd order
1	5.9	1 1 1	1.5	2 × 2	14	0.25	
2	9.7	2 2 0	1.5	2 × 2	26	0.25	
3	13.7	4 0 0	1.5	2 × 2	38	0.20	
4	16.8	4 2 2	1.5	2 × 2	47	0.16	
5	19.4	4 4 0	1.5	2 × 2	55	0.13	
6	22.7	3 1 1	0.5	2 × 2	65	0.12	n
7	27.4	4 0 0	0.5	2 × 2	79	0.16 (0.03)	y
8	30.0	3 3 1	0.5	2 × 2	86	0.08	n
9	33.7	4 2 2	0.5	2 × 2	97	0.11 (0.02)	y
10	35.7	3 3 3	0.5	2 × 2	103	0.05	n
11	38.9	4 4 0	0.5	2 × 2	113	0.08 (0.01)	y

Table 7: *The configuration of lens II. The radius of each ring, the Miller indices of the diffraction plane, the crystal thickness, the crystal surface area, the number of crystals per ring, and the peak efficiency at 511 keV are listed for each ring. For those outer rings also used in 2nd order diffraction, the peak efficiency in second order is listed in parenthesis.*

total crystal area: 4760 cm^2 number of crystals: 2402
lens diameter: 1 m focal spot (90% intensity): 1.65 cm
working energy: 200-1300 keV crystal mosaic width: 25 arc seconds

ring number	radius [cm]	reflection plane [hkl]	T [cm]	crystal size [cm]	number of crystals	ε_{max} (511 keV)	2nd order
1	5.9	1 1 1	0.8	1 × 2	28	0.28	
2	9.7	2 2 0	0.9	1 × 2	52	0.27	
3	11.4	3 1 1	1.1	1 × 1	62	0.16	
4	13.7	4 0 0	1.0	1 × 2	76	0.19	
5	16.8	4 2 2	1.1	1 × 2	94	0.15	
6	19.4	4 4 0	1.2	1 × 2	110	0.12	
7	21.7	6 2 0	1.3	1 × 2	122	0.09	
8	23.8	4 4 4	1.3	1 × 2	136	0.07	
9	27.4	4 0 0	1.0	1 × 2	158	0.19 (0.04)	y
10	29.9	3 3 1	1.2	1 × 2	172	0.11	n
11	33.6	4 2 2	1.1	1 × 2	194	0.23 (0.07)	y
12	35.6	3 3 3	1.4	1 × 1.5	206	0.08 (0.01)	y
13	38.8	4 4 0	1.2	1 × 2	226	0.12 (0.02)	y
14	40.6	5 3 1	1.4	1 × 1.5	236	0.06	n
15	43.4	6 2 0	1.3	1 × 2	252	0.09 (0.01)	y
16	47.6	4 4 4	1.3	1 × 2	278	0.07 (0.01)	y

Table 8: *The configuration of lens III. The radius of each ring, the Miller indices of the diffraction plane, the crystal thickness, the crystal surface area, the number of crystals per ring, and the peak efficiency at 511 keV are listed for each ring. For those outer rings also used in 2nd order diffraction, the peak efficiency in second order is listed in parenthesis.*

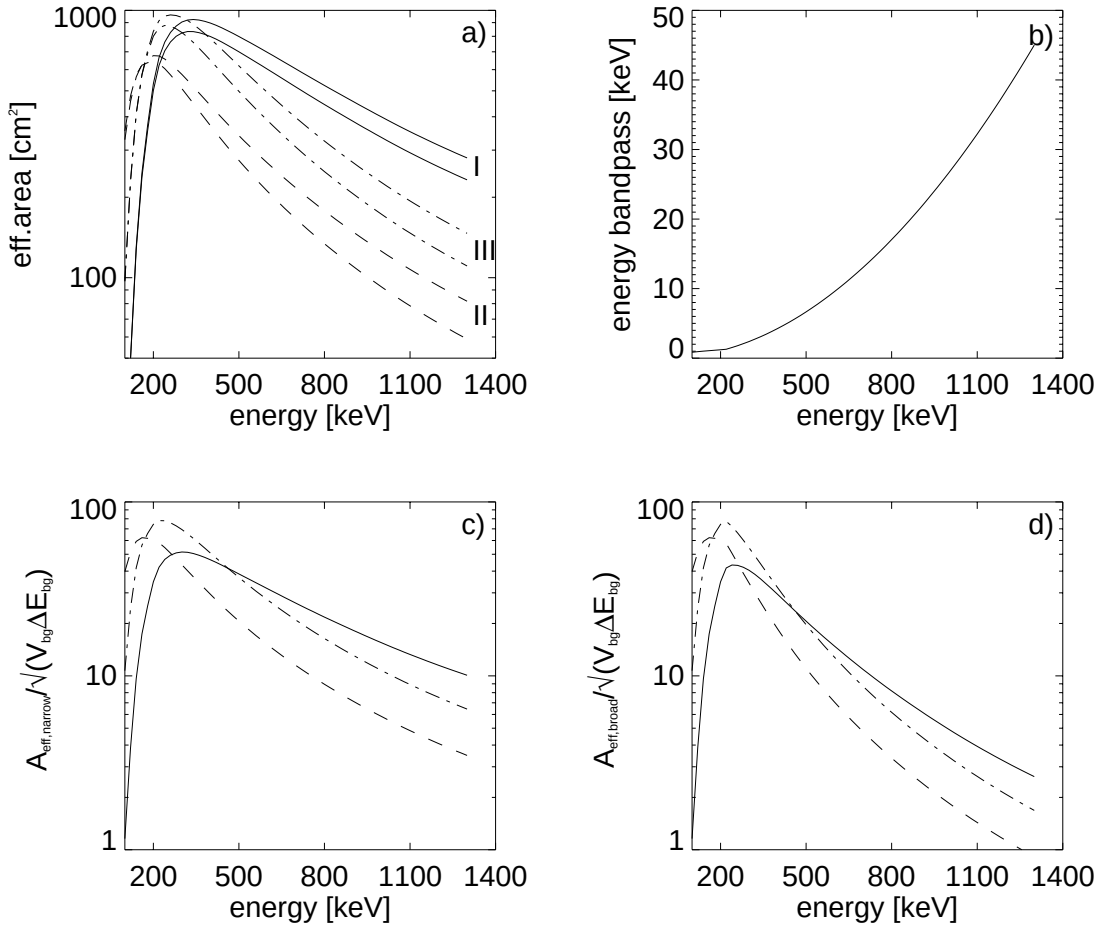

Figure 32: *Plot a shows the effective area as a function of energy for 3 different lens configurations. Configuration 'I' is the 15-ring, 1-detector lens from Table 6, configuration 'II' is the 11-ring, 2-detector lens from Table 7, and configuration 'III' is the 16-ring, 2-detector lens from Table 8. For each configuration, 2 effective area curves can be seen: the upper curve is the narrow line effective area of equation 47, the lower curve is the continuum effective area of equation 48. The continuum effective area is the effective area averaged over the energy bandwidth of the lens. This energy bandwidth is shown in plot b as a function of energy. Plots c and d show the effective area divided by the square root of the background volume and energy bandpass,* $A_{eff}/\sqrt{V_{bg}\Delta E_{bg}}$ *in units of* $cm^{0.5}\ keV^{-0.5}$*, as a function of energy for narrow lines (plot c) and for continuum radiation (plot d).* $(A_{eff}/\sqrt{V_{bg}\Delta E_{bg}})^{-1}$ *is proportional to the telescope sensitivity.*

7 Realization of One Ring of a Prototype Tunable Crystal Lens

The Bragg-relation $2d\sin\theta = nhc/E$ is valid only over a narrow range of angle and energy (and multiples of this energy). Typical energy bandpasses for a crystal lens telescope for on-axis radiation are 3 to 10 keV at 511 keV, increasing with the square of energy. The mosaic width of the crystals could be increased to have a larger energy bandpass, but this would degrade the sensitivity, as the integrated reflectivity is more or less constant. The energy that is focused by the lens can be changed:

- According to the Bragg-relation, the Bragg angle is energy dependent, decreasing with increasing energy. Thus, different energies can be focused if the orientation of the crystalline planes can be changed
- The focal length, i.e., the distance between the lens and the detector, grows linearly with energy, $f = \frac{r}{2\theta} \propto E$. Thus, when the crystals are reoriented to focus a higher energy, the detector must be moved farther away from the lens.

7.1 Range and Resolution Requirements

For the 8-ring crystal lens described in section 4.4 and a working energy range of 200 to 1300 keV, the change in the crystal orientation amounts to a few hundred micron assuming a few cm lever, whereas the detector-lens distance needs to be changed from 3 to 21 m.

The change in crystal orientation when moving from one energy to another is equal to the difference in Bragg angle for the two energies. The Bragg angle as a function of energy is shown in Fig. 33 for the eight crystalline planes of Ge used in the ground-based prototype. The Bragg angle is always smaller than 1.8 degrees. The change in Bragg angle is smaller for the crystalline planes of the inner rings than for the outer rings. The change in Bragg angle from 200 keV to 1300 keV is 0.47° for the (111) plane, and 1.51° for the (440) plane.

The crystals are oriented by pushing one side of a plate holding the crystal, with the other side of the plate fixed to the lens frame. Thus, the angular change of the crystalline planes can be described in terms of a translation of the actuator pushing the plate. This translation is shown as a function of energy for the same configuration as in Fig. 33 in Fig. 34. The curves assume a 2.5 cm lever, and the position at 200 keV was arbitrarily set to zero. The translation range needed for this lever is 200 μm for the (111) plane, and 660 μm for the (440) plane. The crystal orientation needs to be better than the mosaic width of the crystals. This implies an accuracy of a few arc seconds. For an accuracy of 5 arc seconds and a 2.5 cm lever, the translational precision is 0.6 microns.

The detector-lens distance only needs to be accurate to a few cm. At 200 keV, the focal spot for an on-axis point source increases in size by 1 mm for an offset of the detector-lens distance of 1.4 cm, at 1300 keV the offset is 9 cm.

The constraints for a tunable lens with working energy 200 to 1300 keV can be summarized as follows:

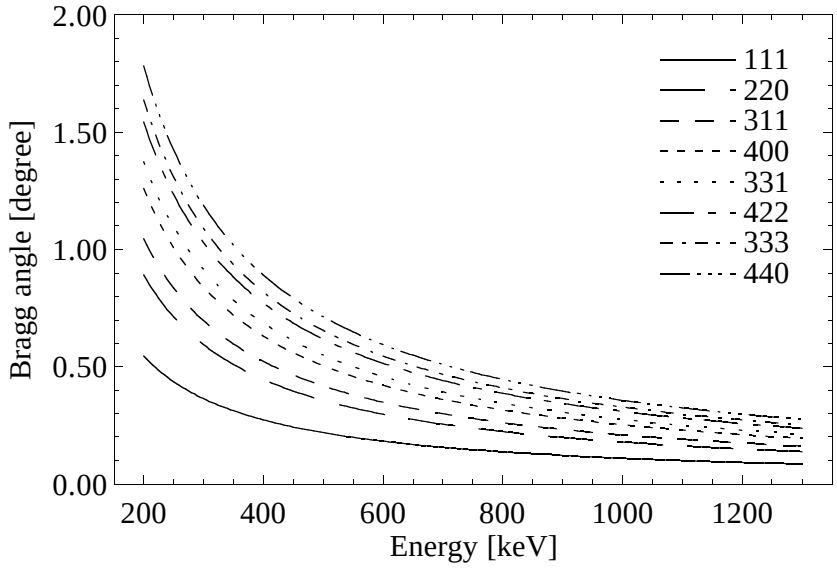

Figure 33: *The Bragg angle as a function of energy for the eight crystalline planes of the prototype lens. The (111) reflection plane is used in the innermost ring, the (440) reflection plane is used in the outermost ring.*

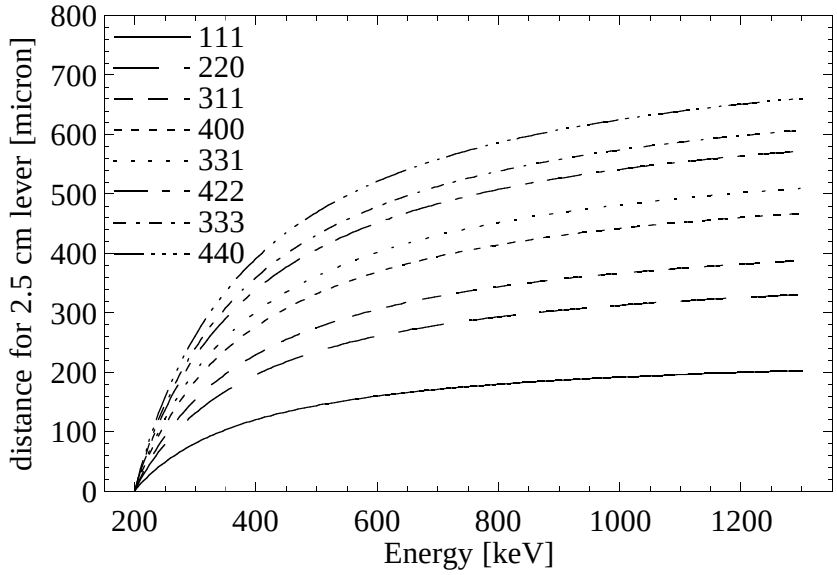

Figure 34: *The change in Bragg angle of the crystalline planes is plotted as a function of energy, assuming a 2.5 cm lever. The crystalline planes correspond to the eight planes of the prototype lens. The position at 200 keV was arbitrarily set to zero.*

- The dynamic range for the crystal orientation needs to be $\approx$ 700 microns for the energy range of 200 to 1300 keV, an 8-ring lens, and a 2.5 cm lever. This corresponds to an angular change of the orientation of the crystalline planes of up to 1.5°. The resolution should be $\ll$ 0.6 microns, corresponding to an angle of 5 arc seconds. The precision, repeatability, and stability need to better than 0.6 microns.

- The focal length is 3.2 m at 200 keV and 21.1 m at 1300 keV. Thus, the detector-lens distance needs to be changed with a dynamic range of 18 m. The positioning only needs to be accurate to a few cm. This can be seen from the fact that the focal spot for an on-axis point source increases in size by 1 mm for an offset of the detector-lens distance of 1.4 cm at 200 keV and 9.0 cm at 1300 keV.

7.2 Picomotor and Eddy-Current Sensor Performance Tests with Autocollimation

In order to achieve the above requirements for the crystal orientation, a combination of a piezo-based picomotor and an eddy-current sensor was tested. The picomotors tested were the New Focus Model 8351 and Model 8301 Picomotor, and the Kaman EASI9500 sensors 2U and 5U.
The picomotor motion is via the rotation of an 80-pitch screw. The screw is held by two threaded jaws connected to opposite sides of a piezoelectric transducer. A slow electrical signal causes the two jaws to slide in opposite directions, moving the screw. A fast electrical signal returns the jaws to their starting position without moving the screw due to the screw's inertia and low dynamic friction. Thus, pulses with slow (μs) risetime and fast (ns) falltime cause the screw to move in one direction, whereas pulses with fast risetime and slow falltime move the screw in the opposite direction. The amount of travel is limited by the length of the screw, and is 12.7 mm. The average picomotor step size is 10 to 20 nm, the maximal repetition rate is 1000 Hz. This gives a maximal velocity of 10 to 20 μm per second. The pulses, with $\approx$ 150 V amplitude, are created by the picomotor driver. The driver is interfaced to a PC via digital I/O lines. As the driver needs 0.2 ms duration step pulses synchronized with the internal driver clock as input, the PC step commands as well as the driver clock signal are fed into a synchronising circuit. The PC step command is a $0 \rightarrow 1 \rightarrow 0$ voltage change with <0.2 ms duration and $\geq$ 1 ms repetition rate.
The two picomotor models tested were different in size and in maximal load. For the 8301 Picomotor, the maximal load is 5 lbs, for the 8351 the maximal load is 1.5 lbs. A vacuum-compatible version of the 8301 is also available.
As the step size of the picomotor fluctuates (see below), a positioning cannot be achieved by counting motor steps. This makes it necessary to use the picomotor in combination with a sensor. Two non-contact eddy-current sensors were tested. These sensors consist of a potted coil comprising the sensor head. The coil inductance is about 10 μH for the 2U sensor, and 60 μH for the 5U sensor. The sensor head diameter is 2 mm for the 2U, and 4.8 mm for the 5U. The coil is part of an LC-circuit driven close to resonance. The driving frequency is 1 MHz for the 5U, and 0.5 MHz for the 2U. The sensors can measure the distance to a conductive plate via the magnetic coupling, which is a function of the plate distance. The oscillating $\vec{B}$-field of the coil induces an eddy-current

in the conductive plate, which in turn changes the impedance of the sensor circuit.
The functioning principle of the sensor can be understood in terms of an equivalent circuit where the conductive plate is characterized by the equivalent plate resistance R_p and equivalent plate inductance L_p, and the sensor circuit as an AC source with sensor resistance R_s and sensor inductance L_s. As the magnetic coupling M between the plate and the sensor depends on the plate-sensor distance, the impedance of the sensor circuit depends on R_p and L_p. The impedance Z can be written as

$$Z = \left[R_c + \left(\frac{\omega^2 M R_p}{R_p^2 + \omega^2 L_p^2}\right)\right] + i\omega \left[L_c + \left(\frac{\omega^2 M R_p}{R_p^2 + \omega^2 L_p^2}\right)\right] \tag{51}$$

with ω as the frequency.
The EASI9500 sensor electronics provide the oscillator and signal conditioning electronics. The temperature is determined by periodically applying a DC-voltage to the sensor. This allows an internal temperature compensation of the sensor distance. The sensor electronics is interfaced to a PC via RS-232. The sensor distance, temperature, and other variables can be queried.
In order to use the picomotors and sensors to orient the crystals, these are glued onto Al-plates, with one side of the plate fixed to the lens frame. The picomotor pushes the other side of the plate, and the sensor measures the distance to the conductive plate holding the crystal.
First tests of the feasibility of this system were done using a theodolyte in autocollimation. A 1-mm-thick Al-plate was fixed at one end to a mount. The 8301 picomotor was mounted to have a 45 mm lever to push on the Al-plate. The 2U and 5U sensor were mounted alongside the picomotor. A mirror was glued onto the Al-plate. The theodolyte, a Wild T2, was placed at 0.8 m distance. Autocollimation allows the precise measurement of the angle of the Al-plate. A light source illumates the reticle of the theodolyte eyepiece via a beam splitter. The cross-hair reticle pattern is projected onto the mirror, the returning reflected beam is diverted to the eyepiece. The deviation in angle from perpendicularity of the mirror is measured at the eyepiece, were both the reticle and its reflected image are seen. The reproducibility of a measurement with the theodolyte was determined to 1.2 arc seconds. The range of the autocollimation, 1.8 degrees, is determined by the fact that the reflected light from the mirror needs to enter the telescope aperture.
The measurements were done by moving the picomotor in increments, reading the sensor values, and independently determining the angle from the autocollimation measurement. There is some uncertainty in the conversion of the sensor distance to an angular distance due to the fact that the bending of the plate is not precisely localized. Fig. 35 shows the raw sensor output as a function of the angle measured with autocollimation for the 2U and the 5U sensors. Kaman specifies the range of the 2U as 0.5 mm, and the range of the 5U as 1.0 mm. For the 4.5 cm lever, this is 0.64° (2U) and 1.27° (5U) respectively. For the specified range, the resolution is 0.15 to 0.3 arc seconds per sensor unit for the 5U, and 0.07 to 0.25 arc seconds for the 2U. If the 2U range is extended to 1 mm, the resolution degrades to 1 arc second per sensor unit.
The sensor calibration was then used to test the motor resolution and reproducibility. The results of these tests can be summarized as follows:

- The mean step size is 15 to 22 nm per step. There is a difference in the mean step size for

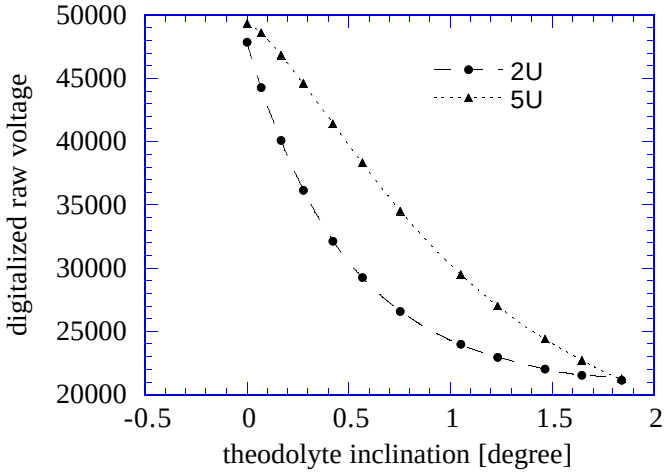

Figure 35: *The sensor output as a function of the angle as measured with a theodolyte in autocollimation. An angular change of 1.27° measured with the theodolyte corresponds to a distance change measured by the sensor of 1 mm. The points are the data, the curves are polynomial fits to the data points.*

forward and backward motion (Fig. 36). This could be due to the load, as the motor pushes against a plate fixed at one end.

- The step size fluctuates around the mean step size. This can be seen from the deviation of the curves in Fig. 36 from a straight line. The standard deviation is 31% of the mean step size for backward-moving steps. The fluctuations could be due to variations in the contact of the jaw and the screw due to lubricant, dust, etc. Thus, positioning cannot be achieved by simply counting motor steps.

- When moving only a few motor steps at once, the mean step size depends on the number of motor steps. This is shown in Fig. 37, where the mean stepsize for 30, 10, and 2 motor steps are compared. The mean step size for 30 steps is 21.4 nm, for 10 steps it is 17.8 nm, for 2 motor steps it is 14.1 nm. This difference could be due to the friction, in particular of the motor tip and the plate.

As the step size depends on the number of motor steps as well as the direction, the following algorithm was implemented to move the plate to a certain sensor value: Assuming that the mean step size for a large number of steps is $\bar{d}_f$ for forward motion and $\bar{d}_b$ for backward motion, and that the difference between the two is $F = \bar{d}_f/\bar{d}_b$, the number of motor steps to move is calculated using these values, as well as the momentary and the nominal sensor values together with the sensor calibration. After moving with the picomotor, the new and old sensor values are used to calculate a new mean step size. The fraction F is assumed to be independent of the number of steps. The sensor value is then compared with the nominal value, and the motor moves a number

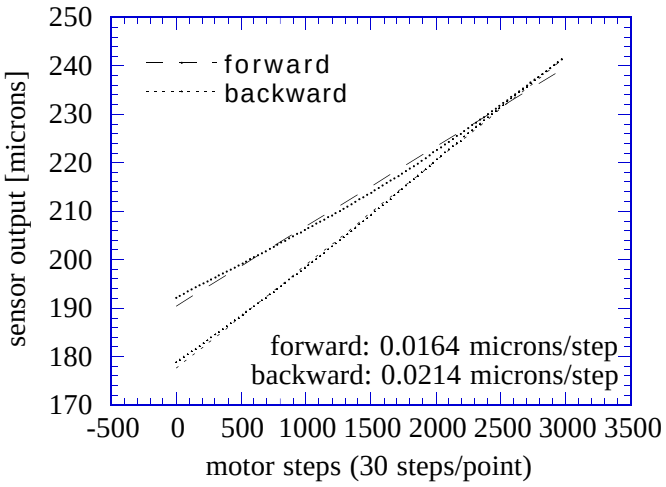

Figure 36: *The 5U sensor distance in microns is plotted as a function of motor steps for forward (long dashes) and backward (short dashes) motion of the motor. The sensor was read out every 30 motor steps. The mean motor step size derived from line fits (dotted lines) is 16.4 nm for forward motion, and 21.4 nm for backward motion.*

of steps calculated using the new mean step size. This continues iteratively until the position is within two sensor units, or ten iterations are exceeded.

The temperature dependence of the sensor output was tested between 10°C and 40°C using an oven. The sensor output changed with temperature by about +1 μm per °C over the entire temperature range for both the 2U and the 5U. The output drift with temperature depended on the sensor mounting, and is presumably due to the thermal dilation of the sensor and the surrounding material. For a 2.5 cm lever, a stability of the crystal positioning of 5 arc seconds requires a sensor stability of better than 0.5 μm. This makes it necessary to work in a temperature-stable environment as well as correcting the sensor output for the temperature.

The resolution of the picomotors of 15 to 22 nm per step, and the resolution of the eddy-current sensors with 15 to 60 nm per sensor unit is sufficient for the tunable lens. The range of the 2U is sufficient for the inner, but not for the outer rings. The 8351 tiny picomotor maximal load is sufficient for orienting the crystal, and is preferable to the 8301 due to its smaller size. For the motorization of the innermost ring of a lens, the 2U sensors were chosen due to their smaller size.

7.3 Buildup of the Tunable Crystal Lens

In order to realize a protoype tunable lens, a new lens frame was machined at Argonne National Laboratory for the same ring configuration as the ground-based prototype of section 4.4. The lens frame is 2.54 cm thick, with a 45-cm diameter, and is made of the titanium alloy Ti6Al4V. There are 8 rings for holding the crystals, and tapped and clearanced holes for mounting the plates

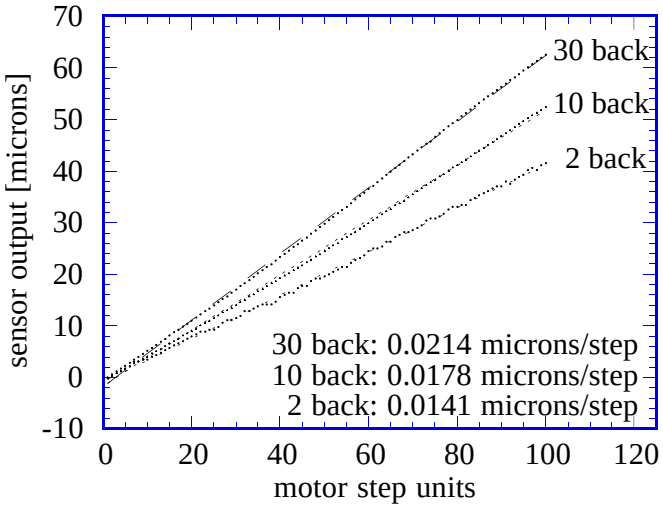

Figure 37: *The 5U sensor distance in microns is plotted as a function of motor step units, for 30 motor steps per unit (30 back), 10 motor steps per unit (10 back) and 2 motor steps per unit (2 back). The "10 back" points were multiplied by 3, and the "2 back" points by 15, so that an identical mean step size would cause the curves to coincide. The points were arbitrarily set to zero at motor step unit 0. The measurements were done at mid-range of the sensor. The mean motor step size derived from line fits (dotted lines) is 21.4 nm for 30 motor steps, 17.8 nm for 10 motor steps, and 14.1 nm for 2 motor steps.*

holding the crystals.

The innermost ring, using the (111) reflection plane, was equipped with 16 wedged 1 cm^3 crystals. For each crystal, a picomotor (New Focus 8351) and eddy-current sensor (Kaman 2U) were used to motorize the crystal orientation (Fig. 38). The crystals were glued onto Al plates, with one side of the plate fixed to the lens frame, and the other side being pushed by the picomotor. The picomotors and sensors were mounted onto Al rings which were then fixed to the lens frame.

The crystals were cut from a 1-cm-thick slab of a 7.5-cm-diameter Ge crystal whose top surface was aligned with the (111) plane. The (220)-surface had been oriented by rotating the crystal in an X-ray spectrometer. The (220)-face was polished, and three of the 4 corners of the (111) face were marked for orientation. The crystals were left unetched after cutting. As the cutting of the crystals was along the (220) plane, not all the crystals had the same miscut, i.e. the same offset between the surface and the crystalline planes. The miscut is in general less than 0.5°. To wedge the crystals, plastic sheets 0.2 mm thick were folded and inserted into the two 0.4-mm-wide and 8-mm-long slots cut into the crystal. The crystals were then cemented onto Al-plates.

Two different types of Al-plates were used, designed to hold one or two crystals. Excepting section 7.9, all measurements below were carried out with only one crystal glued onto each plate. The plates were 0.8 mm thick. The plates were designed to minimize the strain on the crystal, with

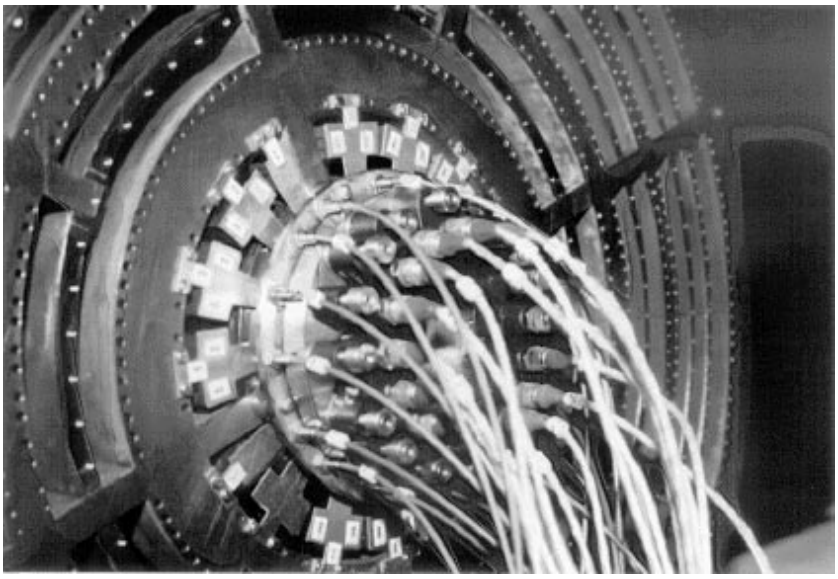

Figure 38: *A photo of the prototype tunable lens. The innermost (111)-reflection ring is equipped with 16 Ge crystals mounted on Al-plates. Each plate is fixed at one end to the lens frame. A picomotor pushes on the other side of the plate to position the crystal. The eddy-current sensor is mounted next to the picomotor. The Ge-crystals are on the back-side of the Al plates and cannot be seen in the photo.*

most of the bending occuring in a thin neck above the region of the crystal. For tests with the double-crystal plates and strain measurements, see section 7.9.

The 16 picomotors and the 16 sensors were mounted separately in aluminum rings, which were then fixed onto the lens frame. The sensors are fixed at 2.2 cm from the pivot, where the pivot is approximated by the middle of the thin neck of the plate. The motor is fixed at 2.9 cm from the pivot. A 1 arc second change in the crystal orientation is then a distance change of 140 nm of the picomotor.

Each picomotor and sensor could be individually adressed and commanded via computer control. The picomotors driver creates the output pulses for the motors. The driver was commanded by PC via a digital I/O board (National Instruments AT-DIO-32F) that creates step and direction pulses. These are then synchronized before being inputed to the driver. The sensor electronics is interfaced to the PC via RS-232. As the sensor electronics and the picomotor driver are made for the command of a single picomotor or sensor, two multiplexing circuits, one for the sensors and one for the motors, were built. The circuits use conventional relays to switch between motors/sensors. The motor multiplexing circuit inputs the driver output step and direction commands, and has 16 outputs going to the individual picomotors. The sensor multiplexing circuit is analogous, with the sensor electronics as input, and 16 outputs going to the individual sensors. Relays were chosen for the picomotors due to the high voltage of the output signals. For the sensors, it was important to

minimize the amount of resistance and capacitance added to the circuit.

7.4 Test Setup

The prototype tunable lens was tested with a setup similar to that used to test the lens with fixed crystal inclinations (section 4.4). The lens was illuminated with gamma-ray line sources with energies ranging from 276 keV to 662 keV, and the focused radiation was detected with a single HPGe detector. The HPGe detector was surrounded by a BGO anticoincidence shield. The lens was set on 2 translation stages, and could be rotated about 3 axes. A Pb-shield in front of the lens could be used to illuminate single crystals. The experiment was computer-controlled using a Pentium 90 MHz PC. The system setup is shown in Fig. 39, a block diagram of the electronics is shown in Fig. 40. The gamma-ray sources were placed at ≈ 25 m from the lens, the detector was placed at distances varying from 5 to 20 m.

For the first prototype lens, where the crystal inclination was fixed, for each energy there was one pair (B,G) for the source-lens and the detector-lens distance (see section 4.4). This type of focusing is only possible for sources with finite distance. In contrast, the tunable lens tests used gamma-ray line sources with a range of energies, all at the same distance to the lens. As the focal length F and the source-lens distance G are fixed, equations 27 and 28 determine the detector-lens distance B and the crystal inclination α. Table 9 lists the focal length, the source-lens distance, the detector-lens distance, and the crystal inclination for the gamma-ray lines used for the tests.

Energy (keV)	Source	Focal Length (m)	Source-Lens (m)	Lens-Detector (m)	Crystal Incl. α (degrees)
276	^{133}Ba	4.48	24.45	5.50	0.25
303	^{133}Ba	4.92	24.45	6.16	0.22
356	^{133}Ba	5.78	24.45	7.57	0.16
383	^{133}Ba	6.24	24.45	8.37	0.14
662	^{137}Cs	10.92	24.75	19.54	0.02

Table 9: *The focal length, the source-lens distance, the detector-lens distance, and the crystal inclination α for the gamma-ray lines used for the tests. The definition of the crystal inclination α is shown in Fig. 19.*

Two gamma-ray sources were used to test the tunable lens: a 95 mCi ^{137}Cs source with a line energy of 662 keV, and a 31.2 mCi ^{133}Ba source with line energies of 276, 303, 356, and 383 keV. The Cs-source is 4 mm long, and has a 3 mm diameter. The Ba-source is 7.62 mm long, and has a 2.72 mm diameter. The branching ratios of the line energies are 84.8% for the 662 keV line, 4.1% for the 276 keV line, 11.5% for the 303 keV line, 45.9% for the 356 keV line, and 7.1% for the 383 keV line.

A collimator is placed in front of the source to define the angular extent of the radiation. For safety purposes and to define the path of the radiation, a system of Al-tubes with successively

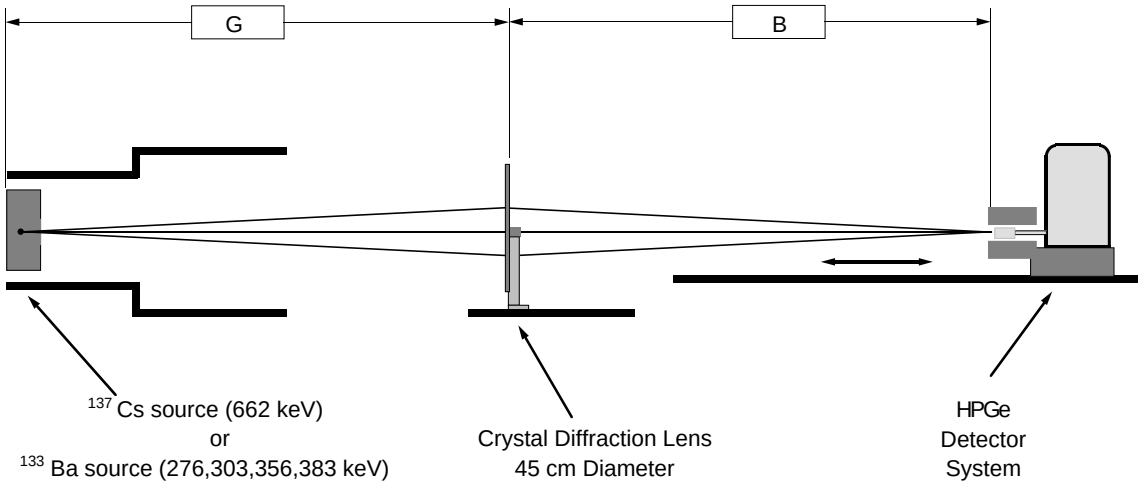

Figure 39: *The setup of the tunable crystal lens tests is shown. The gamma-ray line sources were placed at about 25 m from the lens. The HPGe detector was placed at distances ranging from 5 to 20 m, depending on the energy of the focused radiation.*

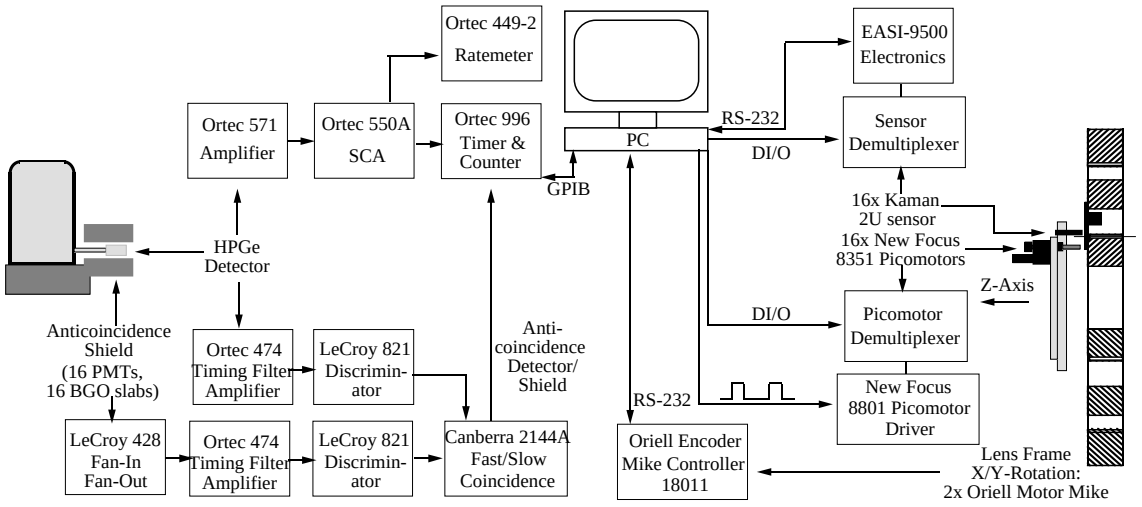

Figure 40: *A block diagram of the electronics of the tunable crystal lens setup is shown.*

larger diameters leads from the source to the lens. For testing and modifications of the detector and the anticoincidence shield, weak reference sources of ^{133}Ba and ^{137}Cs were used.

To describe the lens rotations, the following coordinate system is used. The z-axis points from the source to the detector and defines the optical axis of the lens. The y-axis is the vertical, and the x-axis is the horizontal. The rotation about the z-axis is the ϕ-rotation, the rotation about the x-axis is the χ-rotation, and the rotation about the y-axis is the ψ-rotation. The lens can be translated along the x- and the z-axis using an Aerotech Unidex11 Motion Controller. Using an Oriell Mike Controller and two Mike Actuators, the entire lens can be rotated about the x- and the y-axes. The ψ-rotational position is read out by a Newport PM500C Precision Motion Controller. The range of the actuators allows a rotation of $\pm 1.1^\circ$, the resolution is 0.4 arc seconds. The lens can be manually rotated about the z-axis. The Mike Controller and both Motion Controllers are interfaced to the PC via RS-232.

In order to expose only a single crystal to the source, a 5-cm-thick round Pb-shield the same size as the lens diameter can be translated into place in front of the lens. The shield has a 1-cm-wide slit, and can be rotated about the z-axis. The center of the shield contains a brass rod with 0.5 cm diameter, which can be removed when aligning the system with the help of a laser. To view a single crystal, the shield or the lens are rotated about the z-axis so that the crystal is aligned with the slit of the shield. The slit is then covered with lead excepting the region of the crystal.

The detector is a p-type closed-end coaxial HPGe detector (Ortec GEM-X). The crystal is 6 cm long, and has a 6 cm diameter. The length of the 1-cm-diameter central bore was customized to 3 cm. The detector bias is 2000 V. The detector signal is amplified and processed using standard NIM modules. The count rate in a Single Channel Analyzer (SCA) window is inputed to the PC via GPIB.

The anticoincidence shield consists of 16 slabs of BGO forming a cylinder around the detector. Each slab is separately read out by a photomultiplier tube. The HV is individually adjustable for each tube using a LeCroy HV4032A HV power system, and ranges from 860 V to 940 V. The signals of the individual photomultipliers are summed, amplified, shaped, and then fed into a LeCroy 821 Quad Discriminator with -300 mV threshold. The discriminator output, as well as the amplified detector signal, is sent to a fast/slow coincidence, which creates the anticoincidence signal for the SCA. Variable delays are used to adjust the timing between the detector and the shield signal.

The data acquisition program was written using the National Instruments LabWindow/CVI Version 3.0.1 software. The package incorporates routines for the GPIB and the RS-232 protocol, and allows the construction of a graphical interface with pushbuttons, displays, and graphs. The data acquisition program was extended from existing software written by Tim Graber and Patricia Fernandez at Argonne National Laboratory. The program allows the user to choose scan parameters (see section 7.5), such as the range, step size, accumulation time per point, and gives a graphical display of detector counts versus angle updated with each point during the scan. The program allows a fit of a Gaussian and a constant background to the scan result. The lens can be rotated or translated by entering the number of steps to move or the final value. The momentary sensor values for a chosen sensor is displayed, and individual crystal positions can be changed by entering a new sensor value or the number of motor steps to move.

7.5 Description of Scans

To align, calibrate and test the system of source, lens, and detector, a variety of so-called scans were performed. During a scan, the lens inclination or one or all of the crystal inclinations are changed in small increments around the Bragg angle, and the detector counts in a narrow energy window around the gamma-ray line are accumulated for a fixed time at each step. The lens inclination can be changed by rotating the lens frame around the vertical y-axis (so-called H-Scan) or the horizontal x-axis (so-called V-Scan) using the Mike Actuators. For H- or V-Scans, the orientation of the crystals is fixed. The crystal orientation of a single crystal (so-called single crystal M-Scan) or of all crystals (so-called all-crystal M-scan) can be changed with the picomotors and eddy-current sensors. During M-scans, the lens frame position is fixed. Typical peak count rates for a single crystal are 0.5 to 1 Hz. Typical scan values are a stepsize of 4 arc seconds, a scan range of 160 arc seconds, and an accumulation time of 3 minutes. Thus, a typical scan takes a few hours to complete. The scan result, a curve of the detector count rate as a function of angle, is roughly Gaussian in shape. This is the *rocking curve*, so-named as it is obtained by rocking the crystal about the angle of the Bragg-reflection.

7.6 Alignment of the Source, Lens and Detector

The gamma-ray source, the lens center, and the detector center need to be along a line, which defines the optical axis. Furthermore, the plane of the lens frame needs to be perpendicular to the optical axis.

The initial alignment of the source, lens, and detector is done by shooting a laser beam from the position of the detector through the center of the lens and the center of the Pb-shield onto the Pb-housing of the closed source. Both the lens and the Pb-shield have a few-mm-diameter brass plug in the center which can be removed.

In order to align the lens perpendicular to the optical axis, four scans of one crystal are performed. The four scans are done by rotating both the crystal and the Pb shield about the z-axis (the ϕ rotation), so that the crystal is illuminated by the source at positions $\phi = 0°, 90°, 180°$, and $270°$. At the positions $\phi = 0°$ and $180°$, a V-scan is performed, at the positions $\phi = 90°$ and $270°$, an H-scan is performed. With χ_1, ψ_1, χ_2 and ψ_2 as the angles of the peak count rate in the detector for the scans at $\phi = 0°, 90°, 180°$, and $270°$, the lens frame is perpendicular to the optical axis when rotated to $(\frac{\chi_2 - \chi_1}{2}, \frac{\psi_2 - \psi_1}{2})$.

The plane of the lens frame is monitored with a mirror mounted in the middle of the lens frame. The mirror is adjustable about three points. By bouncing a laser beam off the mirror while turning the lens about the z-axis, the mirror is adjusted to be parallel with the rotation axis of the lens. Assuming that the rotation axis is perfectly perpendicular to the lens frame, the mirror plane then defines the lens plane.

7.7 Tuning the Lens to the First Energy

After the alignment, the individual crystals need to be oriented so that the Bragg-condition is fulfilled. After the position for all crystals for one energy has been found, and the sensors and

motors have been calibrated, the positions for a different energy can be calculated.
In order to find the correct position of all the crystals for the first energy, the following procedure was used: after the correct inclination for one crystal has been found, the laser reflection off the polished crystal face is noted for the correct inclination. For this, the lens is rotated about ϕ so that this crystal is in the top vertical position. Each crystal is then rotated about ϕ to the top vertical position, and the crystal orientation is changed with the picomotor so that the laser reflection is at the same height. This procedure is precise within the miscut differences of the crystals. A V-scan over a large range of angle, with a stepsize of 30 arc seconds (the FWHM of the reflection) and a short integration time is performed to find the peak position of the crystal.

7.8 Calibration of the Sensors and Picomotors

In order to use the picomotors and eddy-current sensors to change the energy focused by the lens, it is necessary to know the crystal orientation as a function of sensor readout, and to know the mean motor step size.
Three procedures were used to calibrate the sensors and picomotors:
A first coarse calibration was achieved with the help of a laser reflection bounced off the reflecting back face of the crystal viewed at 15 m distance. Each crystal was successively rotated around ϕ to the top vertical position. Moving the crystal with the picomotor 3000 steps at a time, 6 to 12 points over the entire sensor range were acquired. From the laser and reflection distance, an absolute angle was calculated for each point. For each crystal, the angle as a function of motor steps and as a function of sensor readout were fitted to a line. This gave an averaged value of the mean motor step size and the sensor resolution. The values varied for each crystal. Both the mean motor step size as well as the sensor resolution ranged from 0.05 to 0.2 arc seconds.
A more precise and automated calibration procedure using a single line energy was realized as follows: each crystal was again rotated into the top vertical position. A series of V-scans were performed, moving the picomotor in increments of $\approx 0.1^\circ$ between each V-Scan. The lens was rotated about the x-axis by -0.1° before each scan to compensate the picomotor movement. As the x-axis rotation (the χ rotation) is calibrated, the picomotors and sensors can be calibrated relative to the χ rotation. For each crystal, the sensor readout as a function of the peak position of the V-Scan in χ was plotted. The deviation of the data points from a linear fit was < 25 arc seconds for all crystals, the deviation from a scond-order polynomial fit was within the errors (2-3 arc seconds, determined by the error of the peak position of the scan) of the measurement. Fig. 41 shows the calibration results for sensor 13.
The picomotors were calibrated by reading the sensor value in increments of 200 motor steps over the entire sensor range, both forwards and backwards. As seen in the preliminary tests (section 7.2), the mean motor step size fluctuates, and there is a systematic difference in the mean step size for forward and backward-moving steps. The standard deviation σ of the step size ranges from 5% to 11%. The sensor calibration values, as well as the mean step sizes for the picomotors, are shown in Table 10.
The third calibration procedure uses several line energies. The lens is aligned perpendicular to the optical axis, and picomotor M-scans are done with each crystal individually at each energy to

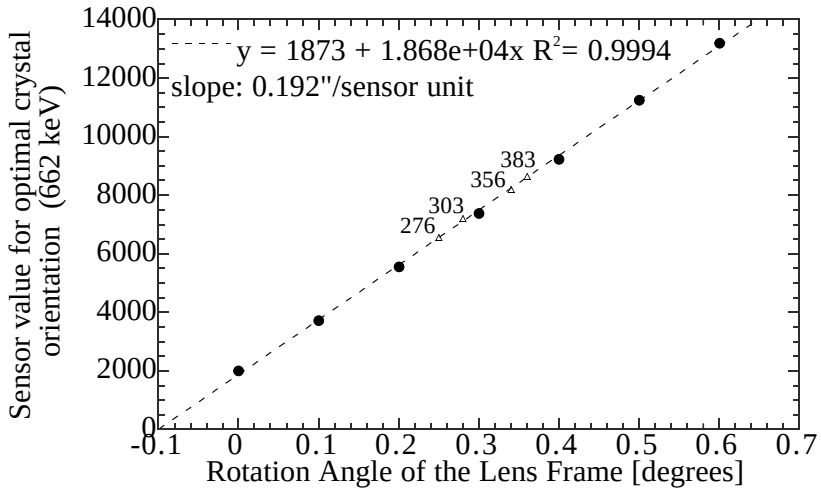

Figure 41: *The calibration data for sensor 13. The sensor value for the scan peak position is plotted as a function of the rotation angle of the lens (filled circles). The scans were done rotating the lens in increments of 0.1° over the entire sensor range. These measurements were done with the 662 keV line source. The dotted line is a line fit to the calibration points. Also plotted are the calibration points from the scan peak positions for the Ba-lines at 276, 303, 356, and 383 keV.*

find the sensor value of the peak position. With the inclinations of table 9, one can then derive a curve of the sensor readout as a function of the crystal orientation. For the sources used, this only gave a calibration over 0.23° in α, so only 1/4 to 1/2 of the sensor range. An error of the source-lens distance of 1 cm translates into an angular error of the calibration of 0.22 arc seconds. The calibration results using the Ba-source lines at 276, 303, 356, and 383 keV are shown in Fig. 41. Both the calibration using one line energy and the calibration using several energies rely on a coarse calibration, as done using the laser reflection off the polished face of the crystal. Calibration errors are due to errors in distance measurements. Any errors in the lens rotation calibration introduce a systematic error of the sensor calibration using one line energy.

7.9 Crystal Plate Tests

The plate holding the crystal should be designed in a way to minimize strain on the crystal, i.e., most of the bending of the plate should occur close to the mounting holes. With T as the plate thickness and b as the plate width, the amount of bending per unit force is $\propto T^{-3}b^{-1}$ and the material strain is $\propto T^{-2}b^{-1}$. Thus, it is advantageous to make the part of the plate close to the mounting holes thinner and narrower than at the position of the crystal.
All measurements and results described in section 7.10 used plates as shown in Fig. 42 a) and b). The plates had a uniform thickness of 0.8 mm, and only one crystal was glued onto each plate.
It would be desirable to have more than one crystal on a plate, in order to reduce the number of

Crystal Number	Arcseconds/ Sensor unit	Sensor Range (degree)	Arcseconds/ motor step (forw.)	Arcseconds/ motor step (backw.)
1	0.158	0.87	0.133	0.200
2	0.120	1.03	0.186	0.202
3	0.130	0.44	0.079	0.093
4	0.120	0.72	0.130	0.138
5	0.167	0.90	0.162	0.193
6	0.160	0.89	0.063	0.110
8	0.157	0.87	0.111	0.130
9	0.169	0.94	0.094	0.130
10	0.115	0.64	0.116	0.128
11	0.091	0.51	0.181	0.228
12	0.117	0.65	0.186	0.196
13	0.192	1.07	0.176	0.445
14	0.200	1.11	0.132	0.155
15	0.093	0.52	0.157	0.162
16	0.144	0.80	0.116	0.193

Table 10: *The calibration values of the picomotors and the sensors are listed. The sensor resolution assumes a linear fit to the calibration data. The motor step sizes quoted are mean values. Crystal 7 is not listed, as it was used to test different sensor types.*

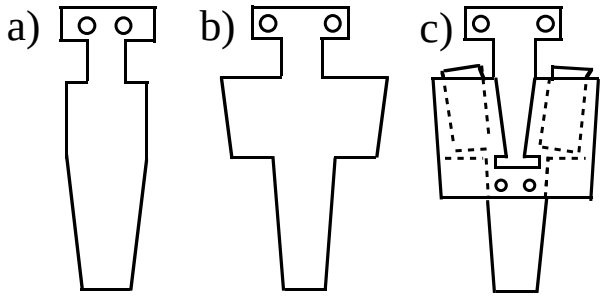

Figure 42: *The crystal plates used for the tunable crystal lens are depicted. A top view of a single-crystal plate (a) and a double-crystal plate (b) are shown. The plates are 0.8 mm thick. Also shown is a double crystal plate tested with 2 crystals (c): the crystals are glued onto a separate Al-plate that is then screwed onto the double-crystal plate. Two shims are used to adjust the relative inclination of both crystals.*

picomotors and sensors and thus the cost and complexity of the system. With this aim, a 2-crystal plate designed by Robert Smither was tested (Fig. 42 c). The differing miscuts and the glueing process make it necessary to adjust one crystal orientation with repect to the other to align the

Relative Plate Inclination	FWHM of Rocking Curve (arc sec)	Peak Count Rate (cps)
0.0°	41.8 ± 1.2	0.90 ± 0.03
0.2°	37.0 ± 0.8	1.13 ± 0.04
0.4°	34.1 ± 0.6	1.21 ± 0.04
0.6°	32.7 ± 0.6	1.34 ± 0.04

Table 11: *The rocking curve width and peak count rate for M-scans of the double crystal plate shown in Fig. 42c. The plate orientation was increased by 0.2° between each scan, and the lens was rotated -0.2° about the χ-axis to compensate.*

orientation of both crystals within a few arc seconds. This is achieved with 2 adjustable wedges, which are glued into place after alignment. The stability of the relative adjustment between the two crystals was tested by a series of M-scans. The plate orientation was increased by 0.2° between each scan, and the lens was rotated $-0.2°$ about the χ-axis to compensate. The results are shown in Table 11. One can see that the relative orientations of the two crystals drift by a few arc seconds over the range of 0.6°, leading to a change in the width and the peak count rate of the scans. The effect may be smaller if the crystals are not wedged.

7.10 Measurements and Results

The lens crystals were oriented to focus the 662 keV radiation carrying out individual scans in angle using the picomotors (M-scans). During a single-crystal M-scan, all other lens crystals were detuned, i.e., offset from the correct inclination. Individual scans result in Gaussian-shaped curves with a width of 31-40 arcseconds FWHM and peak count rates of 1.0-1.7 Hz. With the Ba source in place, the lens was subsequently tuned to 276, 303, 356, and 383 keV by doing single-crystal scans with the same procedure as above.

The sensor calibration and the positioning capability were verified by performing an all-crystal M-scan using the 662-keV radiation. For this scan, all the crystal orientations are changed in increments of $\Delta\alpha$ at each scan step, each crystal being reoriented using the sensor and motor for that crystal. The sensor calibration is used to calculate the sensor value for each crystal at each scan step. For a spaceborne instrument observing a point source, this corresponds to a scan in energy while observing the source on-axis. The result is shown in Fig. 43. If the Gaussian fit of a single-crystal scan is $\dot{N}(\alpha) = A \cdot exp(-\frac{\alpha^2}{2\sigma^2})$ with $\dot{N}(\alpha)$ as the count rate as a function of inclination offset, A as the peak count rate, and σ as the width, then the scan moving all crystals is simply the sum of the Gaussians:

$$\dot{N}_{tot}(\alpha) = \sum_k A_k exp(-\frac{\alpha^2}{2\sigma_k^2}) \tag{52}$$

with k being the index of an individual crystal and the sum being over all crystals. This sum of Gaussians, assuming perfect alignment of all crystals, is the dashed curve seen in the plot.

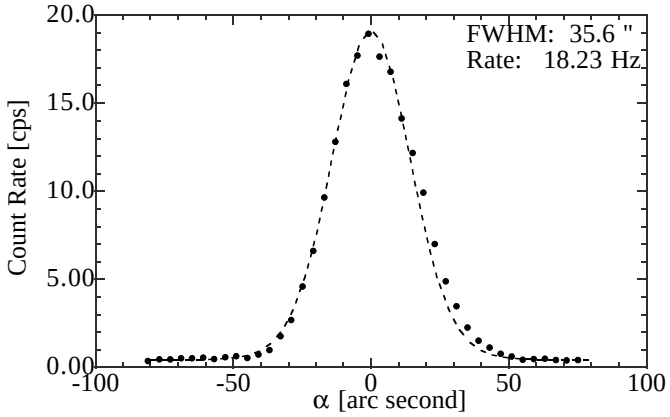

Figure 43: *The figure shows a scan at 662 keV changing the orientation of all the crystals by the same amount $\Delta\alpha$ at each scan step. The peak rate and the FWHM in arc seconds (") are also shown. The dashed line is the scan result calculated using the Gaussian fits to the individual crystal scans and assuming that all the crystals are perfectly aligned. For this scan, the calculated curve is the sum of the individual Gaussians, assuming they are all centered at the same point.*

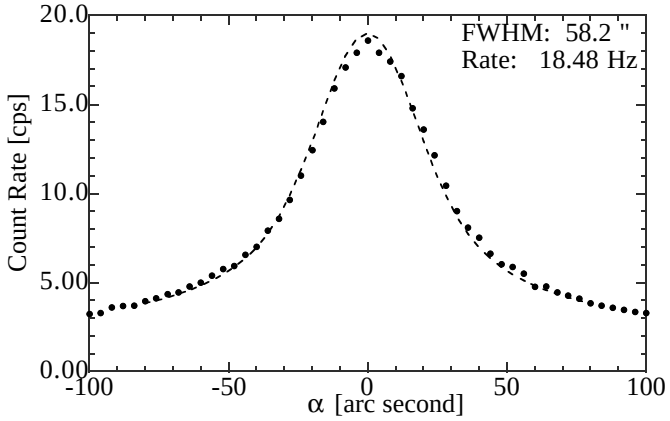

Figure 44: *The figure shows a scan rocking the entire lens around an axis perpendicular to the lens axis using the 662 keV Cs source. The peak rate and the FWHM in arc seconds (") are also shown. The dashed line is the scan result calculated using the Gaussian fits to the individual crystal scans and assuming that all the crystals are perfectly aligned. For this scan, the change in rotation angle equals the orientation change of the crystalline planes only for those crystals with lattice normal $\hat{n}$ perpendicular to the rotation axis; the change in orientation of the planes for those crystals with lattice normal $\hat{n}$ parallel to the rotation axis is negligible. The variation in crystal orientation for different crystals around the ring leads to the broad wings seen.*

This can be compared to a scan in which the crystal orientations are fixed to focus the 662-keV line radiation and the lens frame is rotated around the x-axis, perpendicular to the optical axis (Fig. 44). For a spaceborne instrument observing a point source, this corresponds to a sweep of the optical axis of the lens along a line in space that intersects the source. With the same notation as above, the scan rotating the entire lens can be described in small angle approximation by:

$$\dot{N}_{tot}(\alpha) = \sum_k A_k exp(-\frac{(\alpha cos\phi_k)^2}{2\sigma_k^2}), \tag{53}$$

where ϕ_k is the azimuthal angle of the crystal on the lens frame. This curve, assuming perfect alignment of the crystals, is shown as the dashed curve in the plot. The comparison of the curves with the data shows that the lens crystals are tuned to better than a few arc seconds. The broad wings of the scan rotating the entire lens correspond to the off-axis reponse of the lens to a monoenergetic point source. The ratio of the widths (FWHM) of the 2 scans is 1.63, theoretically one expects 1.64.
Several measurements were performed to check the long term stability of the sensor calibration and the system stability.

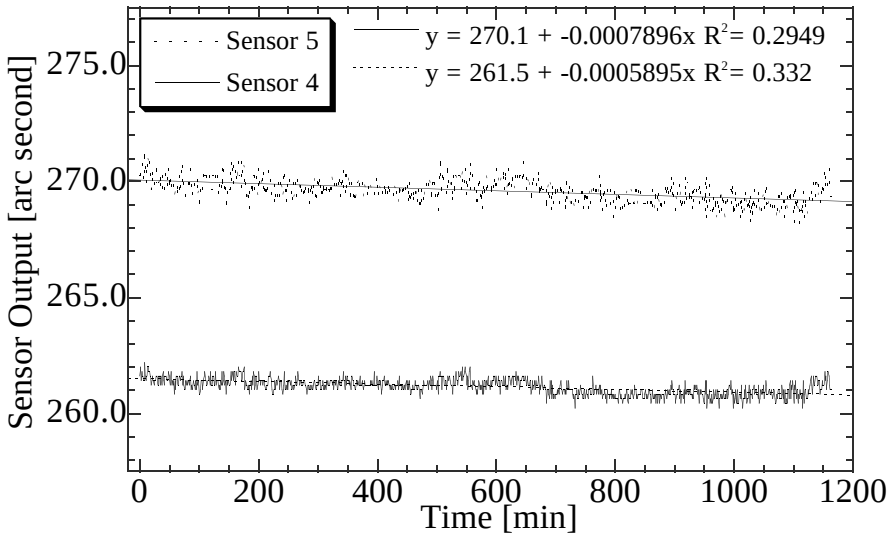

Figure 45: *The sensor stability was measured by reading out the sensor values every 60 s over a period of 20 h. Shown are the results for two of the sensors, along with a linear fit to the data points.*

To test the sensor stability, all sensor values were read out every 60 s over a period of 1.7 days for a fixed lens position. The temperature stability during the measurement was better than 0.5 degrees. The results for 2 sensors are shown in Fig. 45. For each sensor, the mean sensor value $< d >$ and the standard deviation $\sqrt{\sum (d_i - < d >)^2/(n-1)}$ of the resulting distribution of sensor values was calculated (d_i are the individual sensor values and n is the number of points). The standard

deviation ranged from 0.7 to 1.2 arc seconds for all crystals. A linear fit to the sensor values as a function of time shows a long term drift of 1 arc second per 12-25 hours, with the drift direction being the same for all crystals.

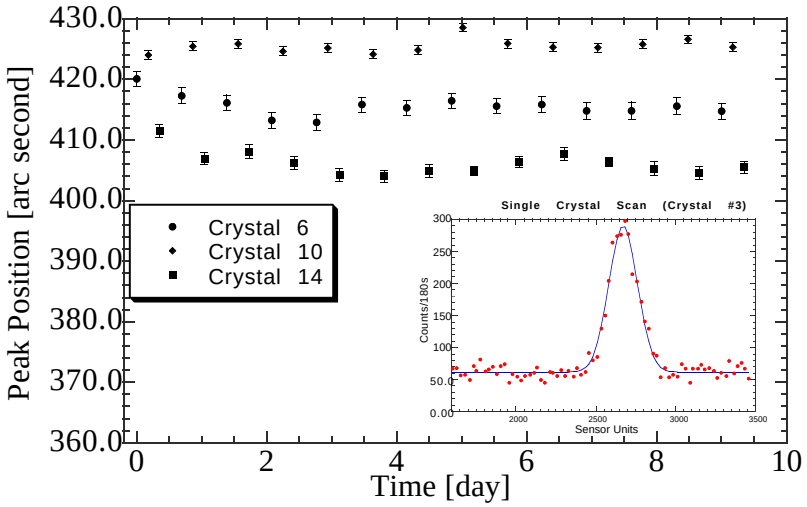

Figure 46: *The peak position of single-crystal M-scans for 3 crystals executed over a period of 10 days. The inset shows the data points of a single scan, and the fit function used to determine the peak position and the error.*

Using the sensor calibration, it was verified that the sensor value for the optimal orientation to focus a certain energy remains stable with time. This was done by consecutive single-crystal M-scans at 662 keV for three crystals over a period of 10 days. This resulted in a total of 14 M-scans for each crystal. Again, the sensor value for each scan point was calculated using the sensor calibration, and all other crystals were detuned during a scan of one crystal. The peak position of the three crystals as a function of time is plotted in Fig 46. The resulting scans were fitted with the sum of a Gaussian and constant background (inset of Fig. 46). Using the peak position and error (0.7-1.3 arc seconds) from the fit, the standard deviation of the peak position was determined to 1.7, 1.1, and 2.0 arc seconds for the three crystals. A linear fit to the peak position as a function of time gives a drift of 0.1 to 0.3 arc seconds per day.

The sensor calibration stability and system stability was also demonstrated by changing the orientation of all crystals to alternately focus two line energies of the Ba source. Consecutive all-crystal M-scans alternating between 303 and 356 keV were performed over a period of 10 days. Each scan was done by moving all the crystals with the picomotors in increments of $\Delta\alpha$ at each scan step. The sensor values for each crystal at each scan step were determined using the sensor calibration. The scans were again fitted with the sum of a Gaussian and a constant background. Fig. 47 shows the total count rate as determined from the fit as a function of time. Both the peak count rate, as well as the width of the scans, remains stable with time.

By slightly detuning the lens crystals, it is possible to broaden the angular acceptance of the lens.

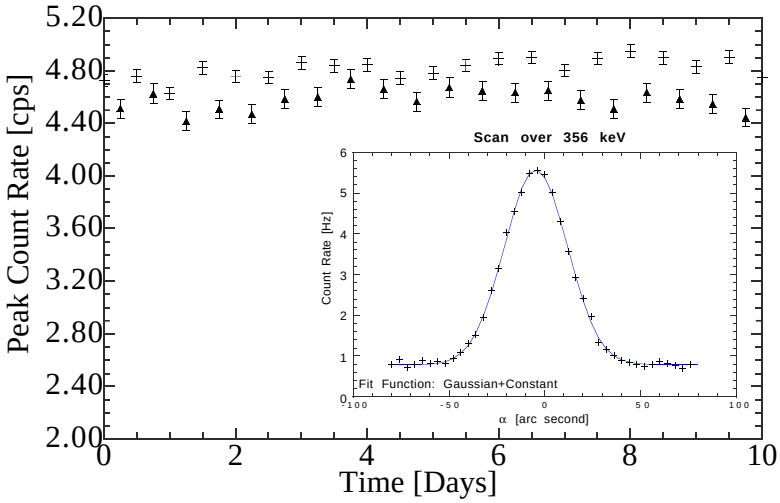

Figure 47: *The evolution in time of the peak count rate for all-crystal M-scans alternately done at 303 and 356 keV is depicted. The crosses correspond to 356-keV scans, the triangles to 303-keV scans. The count rate and error bars of the 303-keV scans have been multiplied by two for better depiction. Each point is the fit result of an individual scan, which is shown in the inset.*

Scanning all crystals in angle simultaneously without detuning the crystals leads to a Gaussian-shaped curve with a FWHM of 36 arc seconds (Fig. 48, filled diamonds). With the crystals detuned with values ranging from -30 arc sec to +30 arc sec, the angular response can be made to be more flat-topped with a FWHM of 80 arc sec (Fig. 48, hollow squares). The integral of the two scans remains unchanged; the peak count rate is decreased by a factor of 2.0. For a spaceborne telescope observing an on-axis point source, this broadening of the angular acceptance would correspond to an increase in energy bandwidth that the lens focuses (with decreased maximum efficiency). This could be advantageous when imaging very broadened gamma-ray lines, e.g., from supernovae of type Ia, as well as when it is desirable to have a more uniform efficiency over the entire energy bandpass of the lens.

7.11 Conclusions

For a spaceborne instrument, the crystals need to be oriented to better than 15 arcseconds. This implies that the system of picomotors and eddy-current sensors must orient individual crystals to better than 15 arcseconds and that the calibration has to remain stable over time. The measurements done here, assuming the implementation of an optical system to periodically check the sensor calibration, show that the sensors and picomotors could fulfill these requirements. The sensor resolution and motor step size of 0.1-0.2 arcseconds allow sub-arc second precision in the crystal orientation. The sensor range of 0.5 to 1 degrees is sufficient for the inner rings of the lens. For the outer rings, which require a range up to 1.5 degrees, a Kaman sensor (5U) with larger

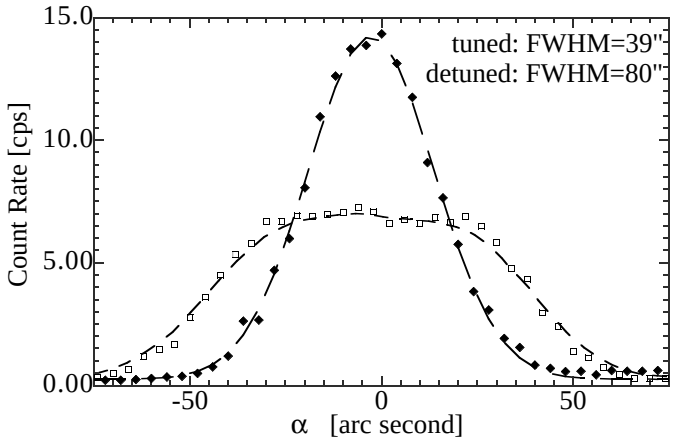

Figure 48: *The count rate as a function of angle for the 662-keV line radiation is shown for scans that change the orientation of all crystals at each scan step. The scan results with slightly detuned crystals (hollow squares) and with tuned crystals (filled diamonds) are shown.*

dynamic range and similar resolution is readily available. The sensor stability has been measured to be better than 2 arc seconds over a period of two days. Measurements of the optimal orientation for single crystals have shown a stability better than a few arc seconds over a period of 10 days. The system stability was also tested by orienting all crystals alternately between two energies, and verifying that the count rate of the focused line energy remains stable with time. The ability to increase the energy bandwidth by slightly defocusing the lens crystals was demonstrated.

A possible scheme to mount picomotors and edyy-current sensor for all eight rings of the lens is shown in [93].

The tunable lens realized here would need to be modified for a spaceborne lens. The design would need to be optimized in terms of weight and power consumption, and would need to be ruggidized to withstand launch vibrations. In order to minimize the time needed to move from one energy to the next, one could envisage a scheme whereby each ring of crystals is moved simultaneously. The travel is different for each ring (see Fig. 34). Afterwards, each crystal would be fine-positioned using the sensor. Assuming a 2.5 cm lever, a picomotor step size of 15 nm, and a maximum speed of 1000 steps per second, the outermost (440) ring would need 45 s to move from 200 keV to 1300 keV.

Kaman has proposed the development of a "single-chip" sensor, with the coil and signal conditioning electronics mounted on a single ceramic chip of size $12 \times 45 \times 6$ mm^3. The chip would use a 1 MHz clock and a regulated 5 V signal as inputs, outputs would be analog voltages for the distance and the temperature. This would facilitate the multiplexing of several hundred sensors.

8 Measurement of Crystal Diffraction Efficiencies using Synchrotron Radiation

8.1 Introduction

Whenever charged particles undergo an acceleration, they emit electromagnetic radiation. For relativistic electrons or positrons subjected to an acceleration perpendicular to their velocity, the emitted radiation is called synchrotron radiation.

The Advanced Photon Source (APS) Synchrotron at Argonne National Laboratory is a third-generation synchrotron that stores positrons with 7 GeV energy in a storage ring. A 200-MeV electron LINAC, a 2-radiation-length-thick tungsten converter target followed by a 450-MeV positron LINAC and an injection synchrotron serve to accelerate the positrons to 7 GeV energy, after which they are injected into the storage ring. The nominal beam current is 100 mA, corresponding to $2.3 \cdot 10^{12}$ stored positrons. A comprehensive list of APS parameters can be found in [120].

The storage ring has a circumference of 1104 m and has 40 periodic sectors. 34 of these sectors can be used for insertion devices, i.e., undulators and wigglers, and there are 34 bending magnets. The APS dipole magnets have a bending radius of 39 m and a magnetic field strength of 0.6 T. The critical energy is 19.5 keV.

The efficiency of the prototype crystal lens was low, ranging from 3% to 6% over the energy range of 303 keV to 662 keV (section 4.4). This was due to the mismatch between the narrow mosaic width of the crystals (a few arc seconds) and the angular extent of the source as seen by the crystal (80 to 200 arc seconds). Calculations using the Darwin mosaic model show that much higher efficiencies are expected for parallel incident gamma-rays, which is the case for an astrophysical point source. Due to the wedging of the lens crystals, and the finite source distance from the lens, an extrapolation of the diffraction efficiency for astrophysical sources from these measurements is difficult. Furthermore, the lens was illuminated with gamma-ray line sources. However, the continuum response of a crystal is important in terms of understanding the telescope response to an astrophysical source.

In order to overcome these problems, two experiments were carried out at the APS sector 1 bending magnet beamline in April/May 1997 and in September 1997. Absolute diffraction efficiencies were determined for non-wedged Ge (111) and Ge (220) crystals (section 8.3.1), and relative efficiencies were measured for 2nd and 3rd order diffraction (section 8.3.2). The dependence of the diffraction efficiency on the mosaic width was measured over a range of widths from a few arc seconds to 0.4° (section 8.3.3). These measurements served to verify the Darwin mosaic model used to calculate the telescope performance. The effect of surface damage induced by cutting the crystals on the diffraction efficiency was determined (section 8.3.4). Finally, the effect of the wedging on the diffraction efficiency was measured (section 8.3.5).

Synchrotron radiation has major advantages for the determination of diffraction efficiencies and crystal characteristics:

- Synchrotron radiation is a continuum. Using gamma-ray sources, only the efficiency for line radiation can be determined.

- The angular divergence of the beam is small, and can be defined by slits upstream of the experiment. The high brilliance allows the use of small slit sizes, and thus small angular divergence. The measurements described below were made using beams with 1 to 5 arc seconds angular divergence. It is important to note that the intrinsic width of the vertical component of the beam decreases with energy, and is 8.8 arc seconds FWHM at 200 keV and 5.4 arc seconds at 500 keV.

- The small beam size can be exploited to measure crystal characteristics over the face of a crystal. Mosaic widths and efficiencies can be determined as a function of position of the crystal. These measurements were done with a 0.4 × 0.4 mm^2 beam size.

- The high brilliance of the synchrotron beam and the high positron energy allow measurements at gamma-ray energies. At APS, it was possible to measure up to 500 keV using the bending magnet synchrotron flux. For energies much larger than the critical energy, the energy-dependence of the on-axis flux in ph/(s $mrad^2$ 0.1%bw) is

$$\frac{d^2F}{d\theta d\psi} \propto E \cdot e^{-E/E_c} \tag{54}$$

  with E_c as the critical energy. The calculated and measured bending magnet flux for a 4.2 mm × 0.6 mm slit placed at 30 m from the source is shown in Fig. 49. Assuming 100 mA beam current, the bending magnet flux is $1.2 \cdot 10^8$ ph/(s 0.1%bw) at 200 keV, falling off by approximately two orders of magnitude per 100 keV increase in energy.

8.2 Experimental Setup

The experimental setup is shown in Fig. 50. The experiment consisted of an 0.5-inch-thick water-cooled copper block to absorb low-energy photons, a first crystal, a tungsten beam stop, a Pb-block to absorb small-angle scattered photons, a second crystal, and an HPGe detector. Upstream slits at 23.5 m from the radiation source are used to define the beam size and the angular divergence. Upstream filters of 600 microns of copper reduce the low-energy background.
The first and second crystals are a double crystal monochromator. The distance between the 1st and 2nd crystal was 157 cm. The efficiencies for the Ge (111) and the Ge (220) diffraction planes were measured using both crystals. The relative efficiency of Ge (333) compared to Ge (111) as well as the relative efficiency of Ge (440) to Ge (220) was measured only using the first crystal. Using the coordinate system shown in Fig. 50, both the first and the second crystal could be translated along the x- and y-axes. The HPGe detector could be translated in three directions using the translation stages of the optical table. With θ as the rotation about the x-axis, ϕ as the rotation about the y-axis, and χ as the rotation about the z-axis, the first crystal could be rotated about θ, the second crystal had a θ stage as well as χ, ϕ rotation stages. The θ stage is used to adjust the Bragg angle, whereas the χ and ϕ rotations are needed to align the second crystal perpendicular to the beam direction. The resolution of the rotation stages of the second crystal was 0.0144 arc seconds in θ and 0.144 arc seconds in ϕ and χ for the April/May experiment and 0.45 arc seconds in θ and 9.0 arc seconds in ϕ and χ for the September experiment.

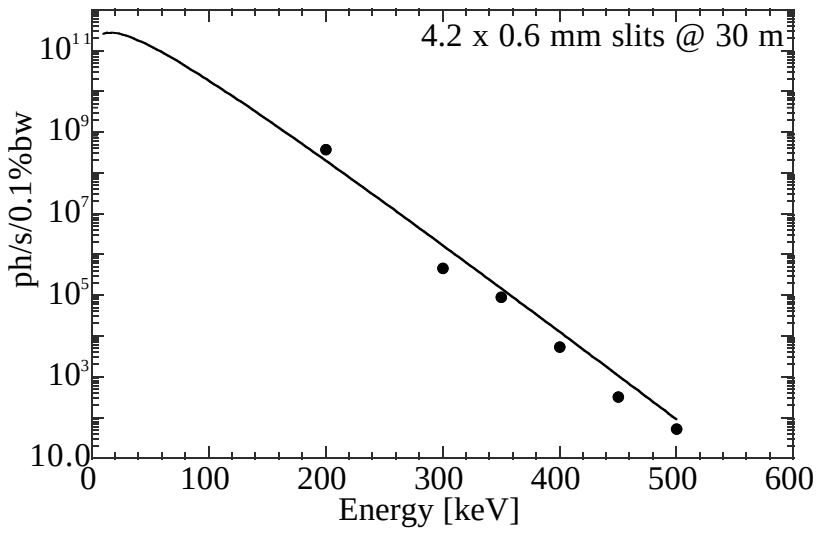

Figure 49: *The bending magnet flux at the Advanced Photon Source (APS) synchrotron is shown as a function of energy for a beam current of 100 mA. The flux is in units of photons per second and per 0.1% bandwidth. The curve is calculated using srixop, a modified version of the xop-program written by Jonathan Lang at APS, and assumes a slitsize of 4.2 mm in the horizontal and 0.6 mm in the vertical at a distance of 30 m from the source. The filled circles are data points, corrected for multiple absorbers.*

All crystals used were Ge, and the diffraction was in Laue geometry. All measurements were done using crystals of the same material as the lens crystals, except in section 8.3.3, the measurement of diffraction efficiencies as a function of mosaic width. All crystals were unwedged, except in section 8.3.5, the measurement of the wedged crystal.

A 6-cm-diameter p-type coaxial HPGe-detector at 244 cm from the first crystal together with tungsten collimators was used to measure the diffracted and transmitted flux of the crystals. In order to minimize dead time and pileup, Pb-absorbers of thickness varying from 1 to 9 mm were placed in front of the detector to keep the total count rate below 15 kHz. The detector was translated at each measurement so that the beam hit the same part of the detector. The detector signal was read out with a 12-bit resolution ADC, the resolution of acquired spectra was 0.27 keV per channel. A Ba-reference source, with lines at 276, 303, 356, and 383 keV was fixed to the side of the detector during the entire measurement in order to monitor the energy calibration and the energy resolution.

The read-out electronics were VME-based. The experiment was computer-controlled using EPICS, (Experimental Physics Industrial Control System), a set of software tools and applications developed by Los Alamos National Laboratory and Argonne National Laboratory.

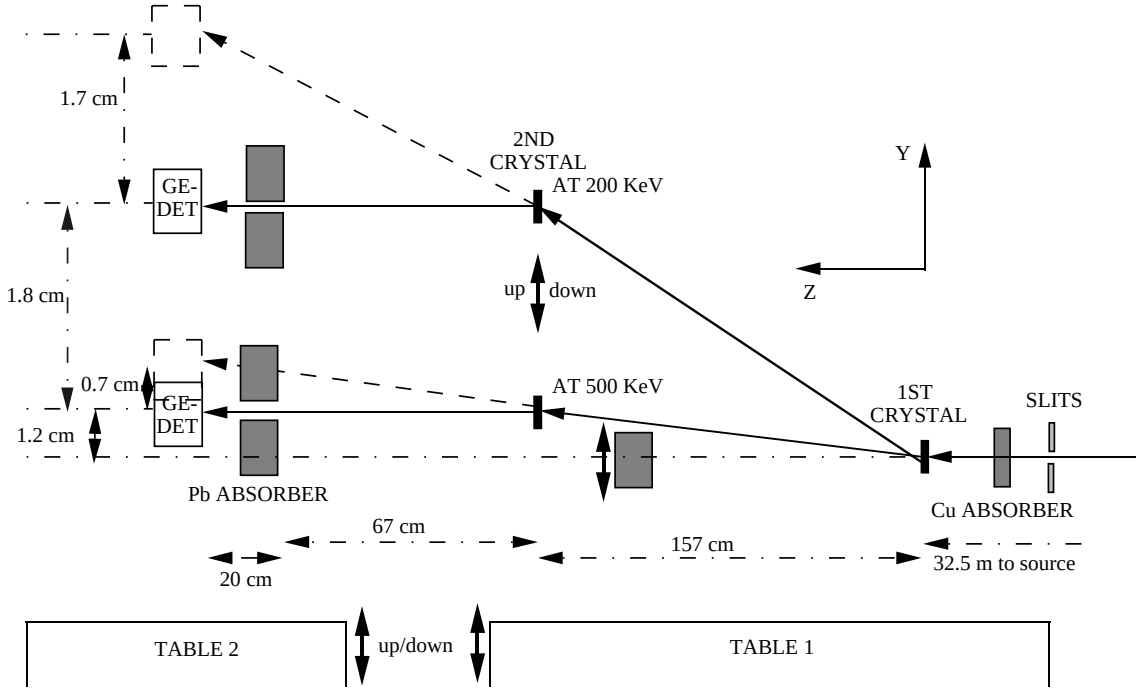

Figure 50: *The experimental setup of the synchrotron experiments. Two optical tables are used. The first table holds absorbers, the first crystal, a beam stop, and the second crystal. The detector is on the second table. The distances between first and second crystal and the detector are shown. Also shown are the vertical displacement of the detector and the second crystal for the singly diffracted and doubly diffracted beam, both at 200 keV and at 500 keV.*

8.3 Diffraction Efficiency Measurement

To measure the diffraction efficiency as a function of energy, a double-crystal setup was used. The measurements were performed for a set of (111) crystals and a set of (220) crystals.

At each energy, the first crystal was adjusted in the Bragg angle θ to select a narrow band of energies. The singly diffracted energy spectrum was measured using the detector and a multichannel analyzer (MCA). After accumulating the MCA spectrum of the singly diffracted beam, the second crystal was centered on the diffracted beam of the first crystal. A rocking curve of the second crystal at the Bragg angle was taken. Finally, an MCA spectrum of the doubly diffracted beam with the second crystal adjusted to the peak of the rocking curve was accumulated. The MCA energy spectra of the singly diffracted and the doubly-diffracted beam as well as the rocking curve are shown in Fig. 51 for the (111) diffraction at 300 keV.

These measurements were repeated at several energies from 200 to 500 keV. The second crystal and the detector were translated at each measurement so that the beam was always diffracting off the same part of the crystal and hitting the same spot on the detector.

The ratio of doubly-diffracted to singly-diffracted flux measures the acceptance of the 2nd crystal

to those photons diffracted by the first crystal. The peak efficiency for photons with zero angular divergence can then be determined with a ray-tracing simulation. The mosaic width of the crystals can however be determined by the energy width of the singly-diffracted and the energy width of the doubly-diffracted flux. The rocking curve width is the convolution of the mosaic width of both crystals and thus provides redundant information.

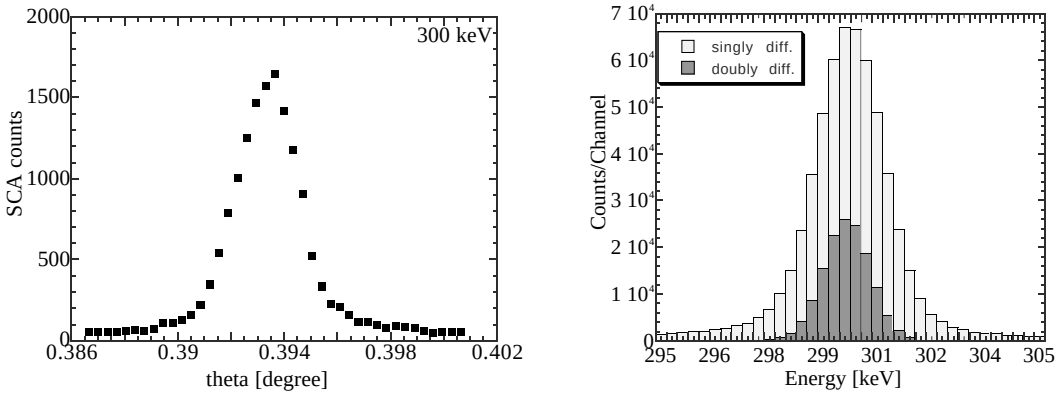

Figure 51: *A sample of the raw data taken during the experiment. The left-hand plot shows a rocking curve of the second crystal at 300 keV. The right-hand plot shows the energy spectra of the singly diffracted and doubly diffracted beam.*

8.3.1 Ge (111) and Ge (220)

The (111) measurement was carried out with two 3-mm-thick crystals. MCA spectra and rocking curves were measured from 200 to 500 keV in steps of 50 keV.

Figure 52 shows the FWHM of the energy spectra of the singly diffracted and doubly diffracted flux as a function of energy. The energy bandwidth of the singly diffracted beam ranged from 1.0 to 5.3 keV for 200 to 500 keV; for the doubly diffracted beam, the values ranged from 0.5 to 3.6 keV. These values have been deconvolved with the detector energy resolution, which was measured using reference sources of ^{133}Ba and ^{137}Cs. The detector resolution was fitted with $\Delta E_{det} = \sqrt{(N + CE)}$, with N as the noise term, and C as the instrinsic resolution, dependent on the Fano-factor and the energy per electron/hole pair. The measured MCA energy widths were always larger than the detector resolution. The energy bandwidth of the reflection was determined by $\Delta E = \sqrt{(\Delta E^2_{meas} - \Delta E^2_{det})}$ with ΔE_{meas} as the measured width.

By integrating the MCA counts of the singly-diffracted and doubly-diffracted flux, the ratio of doubly-diffracted to singly-diffracted counts was determined. This ratio is plotted in Fig. 53, and ranges from 27% to 31%. In order to make the measurement independent of the crystal thickness, the values corrected for the absorption in the crystal, i.e. multiplied by $1/exp(-\mu T)$, are also

plotted. μ is the total absorption coefficient, and includes both the photoelectric effect and the Compton effect. The corrected values range from 31% to 36%. The rocking curve widths of the second crystal ranged from 8.4 to 10.6 arcseconds.

The same measurement was performed using two 10.06-mm-thick Ge-crystals, and diffracting off the (220)-planes. The measurements were performed from 230 keV to 410 keV in steps of 30 keV. The ratio of the doubly-diffracted to singly-diffracted flux is shown in Fig. 53, and ranges from 21% to 26%. The ratio corrected for absorption in the crystal is also plotted, and ranges from 39% to 49%. The effect of the absorption is greater for the (220) measurement than for the (111) measurement, as the (220) crystal was three times thicker than the (111) crystal. Also, one can see that the (220) crystal is more efficient than the (111) crystal if absorption is neglected. The rocking curve width was 5.5 ± 0.2 arc seconds at all energies. The width of the MCA spectrum of the singly diffracted flux ranged from 1.2 keV at 230 keV to 2.4 keV at 410 keV.

To model these results, a Monte Carlo ray-tracing simulation was written. To simulate the MCA curve of the singly diffracted beam, photons random in angle over the range of the slit and random in energy over an energy window larger than the crystal acceptance were generated. Both the energies and angles were generated from a flat distribution. The first crystal is fixed in inclination to reflect the energy $E_\circ$ for parallel incoming photons. The diffraction efficiency was calculated using the Darwin model, i.e., equations 15 and 20.

The energy spectrum was determined by averaging the efficiencies for 30000 photons per 0.25 keV energy bin. To simulate the MCA response of the doubly diffracted beam, the same procedure was used, but now the total diffraction efficiency is the product of both crystals:

$$\begin{aligned} \varepsilon(\theta - \theta_b) = & [0.5 \cdot exp(-\mu T_1) \cdot (1 - exp(-2\alpha_1 T_1))] \cdot \\ & [0.5 \cdot exp(-\mu T_2) \cdot (1 - exp(-2\alpha_2 T_2))] \,, \end{aligned} \tag{55}$$

with T_1 and T_2 as the crystal thicknesses and whereby the two crystals can have different mosaic widths. The best agreement for the (111) data was found for a first crystal of 5 arc second mosaic width (FWHM) and a second crystal of 3 arc second mosaic width. The result of these simulations is shown as the solid and dashed lines in Fig. 52 and Fig. 53. The simulation also reproduces the measured rocking curve widths within 6%. The simulation gives a peak efficiency of the second crystal to monochromatic radiation with zero angular divergence of 37% at 200 keV rising to 43% at 500 keV assuming a 3 arc sec mosaic width.

The results of the ray-tracing simulation for the (220) measurement are shown as the solid and dashed line in Fig. 53. The MCA widths were too small to allow a reliable determination of the mosaic widths. The crystals were assumed to have identical mosaic widths, and the width was adjusted to reproduce the measured rocking curve width of 5.5 arc seconds. The best agreement was found for a mosaic width of 3 arc seconds. Assuming the crystals have identical mosaic width, the flux ratio of Fig. 53 is not very sensitive to the mosaic width. The ray-tracing simulation gives a peak efficiency of the second crystal to monochromatic radiation with zero angular divergence of 20% at 200 keV rising to 32% at 500 keV assuming a 3 arc sec mosaic width.

From equation 26, one would expect the energy bandpass to increase with the square of energy. The data do indeed show this general behaviour. The ray-tracing simulation shows a slight deviation

due to saturation effects which broaden the energy bandpass at low, but not at high, energy. Equation 26 also implies that the energy widths of the (111) and the (220) crystals should scale as the ratio of the crystalline plane spacing

$$\frac{\Delta E_{111}}{\Delta E_{220}} = \frac{\sqrt{h_{220}^2 + k_{220}^2 + l_{220}^2}}{\sqrt{h_{111}^2 + k_{111}^2 + l_{111}^2}} = \frac{\sqrt{8}}{\sqrt{3}} = 1.6 \tag{56}$$

if the mosaic widths are assumed to be identical. The MCA widths of the (220) measurement are indeed narrower than for the (111) measurement.

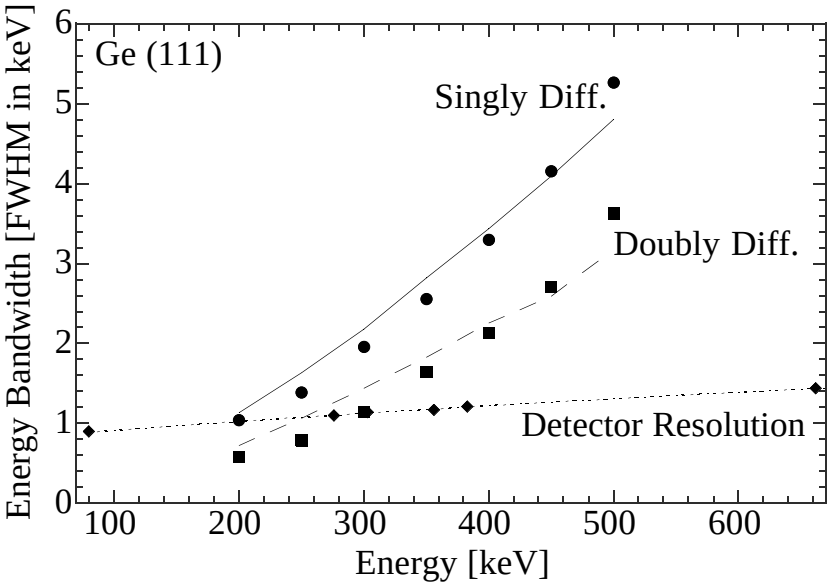

Figure 52: *The figure shows the FWHM of the energy spectra of the singly diffracted (filled circles) and doubly diffracted beam (filled squares) as a function of energy for the Ge (111) measurement. The data points have been deconvolved with the detector resolution (filled diamonds), which was determined separately using reference sources. The curves for the singly and doubly diffracted energy widths are the result of a ray-tracing simulation, and assume a first crystal with a 5 arc second mosaic width, and a second crystal with a 3 arc second mosaic width. The dotted curve is a fit to the detector resolution assuming* $\Delta E = \sqrt{N + C \cdot E}$.

8.3.2 Ge (333) and Ge (440)

According to equation 15 and 20, the diffraction efficiency depends on the crystalline plane used for the diffraction. Assuming the same mosaic width and the same photon energy, the ratio of the diffraction probability per unit thickness α for two different crystalline planes (hkl) and $(h'k'l')$ is given by

$$\frac{\alpha_{hkl}}{\alpha_{h'k'l'}} = \frac{F_{hkl}^2}{F_{h'k'l'}^2} \cdot \frac{sin(2\theta_{h'k'l'})}{sin(2\theta_{hkl})} \tag{57}$$

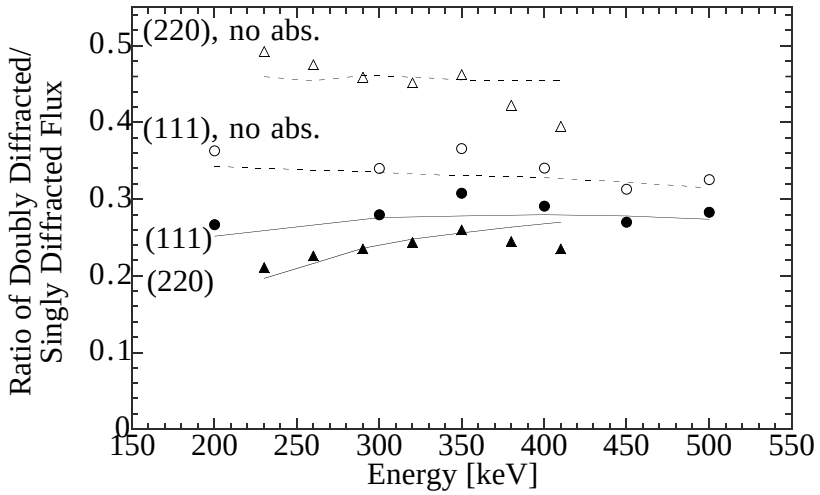

Figure 53: *The ratio of the doubly diffracted flux to the singly diffracted flux is plotted as a function of energy both for the 3-mm-thick Ge (111) crystal (filled circles) and the 10-mm-thick Ge (220) crystal (filled triangles). Also shown is the ratio if there were no absorption in the crystal. One can see that the (220) crystal (open triangles) is more efficient than the (111) crystal (open circles) if the ratios are corrected for absorption. The solid and dotted curves are the results of a ray-tracing simulation.*

In particular

$$\frac{\alpha_{220}}{\alpha_{440}} = 4.31 \tag{58}$$

and

$$\frac{\alpha_{111}}{\alpha_{333}} = 7.49. \tag{59}$$

These relations can be verified by looking at higher order reflections: a (220)-crystal also diffracts along the (440) planes (second order), and a (111)-crystal diffracts along the (333)-planes (third order). Thus, the ration of the efficiencies of the (220)/(440) planes as well as the (111)/(333) planes can be measured using the same part of one crystal, so the above assumption of identical mosaic width holds.

The (220) to (440) flux ratio was measured from 260 keV to 410 keV in steps of 30 keV. This was done by measuring the energy spectrum of the diffracted flux of a 10.06-mm-thick Ge crystal mounted in the 1st crystal position of Fig. 50. No second crystal was mounted. Pb-absorbers of thicknesses between 1 and 10 mm were used to avoid pileup in the detector. The attenuation of these absorbers was measured directly at each energy by varying the total absorber thickness. The measurements were repeated with beam divergences ranging from 1 to 7 arc seconds

The energy spectra were fitted with the sum of a quadratic and a Gaussian to determine the width and the integral count rate. The count rates were afterwards normalized to 100 mA beam current and to identical Pb-absorber thickness. As the peak energies for a (220) and a (440) flux

measurement were slightly different ($\leq$2 keV), the ratios were corrected according to the calculated synchrotron flux incident on the crystal.

The determined ratios for the (220) to (440) flux are summarized in Fig. 54. The ratios range from 2.4 to 2.6, and are independent of the angular divergence of the beam. The expected ratio was calculated using the ray-tracing program described in section 8.3.1. The data points are best fitted by a crystal with 4 arc seconds mosaic width. For the efficiency measurements, the best fit was 3 arc seconds for the same crystal. The calculated increase of the flux ratio with energy is due to saturation at low energies: for large values of α, the integral $\int \varepsilon(\theta - \theta_b)d\theta$ only increases marginally with increasing α. However, the data points show little evidence for an increase of the flux ratio.

The ratio of the (111) to (333) flux was measured at 290 keV using a 2.48-mm-thick Ge crystal. The measured ratio was 6.9. The calculated value is 6.6 assuming a mosaic width of 4 arc seconds, and 7.4 assuming a mosaic width of 5 arc seconds.

It is important that the flux ratio of higher order reflections depends on the crystal mosaicity as well as the type of incident radiation. For monoenergetic radiation with arbitrary angular divergence, from equation 15 one obtains that the ratio of the (220) to (440) flux,

$$\frac{\varepsilon_{220}}{\varepsilon_{440}} = \frac{\int (1 - e^{-2\alpha T})d\theta}{\int (1 - e^{-(2\alpha/4.31)T})d\theta}, \tag{60}$$

is 1 in the limit of large α (small mosaic width) and 4.31 in the limit of small α (large mosaic width). For continuum radiation, the same is true, excepting that the limiting ratio for large mosaic width is $2 \cdot 4.31 = 8.62$, as the energy bandpass for the (220)-reflection is twice as large as for the (440)-reflection. In reality, the Darwin theory breaks down at small mosaic widths, and the limiting ratio for large α is determined by the ratio of the Darwin widths. For the (111) to (333) reflection, the limiting ratio is 7.49 for line radiation and $3 \cdot 7.49 = 22.5$ for continuum radiation, as the energy bandpass for the (111) reflection is three times that of the (333) reflection.

8.3.3 Dependence of the Diffraction Efficiency on the Mosaic Width

According to the Darwin model, the peak diffraction efficiency decreases as the mosaic width of the crystal increases. From equation 15, the peak efficiency ε_{max} and the rocking curve integral I as a function of mosaic width σ are

$$\varepsilon_{max}(\sigma) = A(E)\left(1 - e^{-B(E,(hkl))/\sigma}\right) \tag{61}$$

$$I(\sigma) = \int \varepsilon(\theta - \theta_b, \sigma)d\theta \tag{62}$$

with $A(E)$ as an energy dependent, and $B(E,(hkl))$ as an energy and diffraction plane dependent constant.

The peak efficiency and the rocking curve integral were measured for a large range of mosaic widths using a 2.46-mm-thick Ge crystal that had been squeezed and heated in order to increase the mosaic width. A pressure of 625 lb at 500 degrees Celsius was applied to the crystal for a duration of 5 h. After squeezing, a topograph of the crystal was measured: The crystal was mounted to diffract

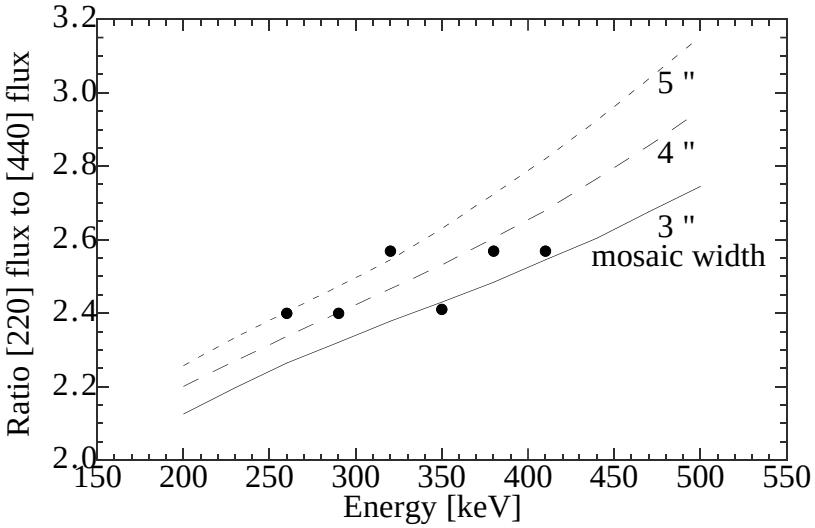

Figure 54: *The ratio of the flux diffracted off the (220) planes to the flux diffracted off the (440) planes as a function of energy is plotted. The (220) and the (440) flux are diffracted off the first crystal, no second crystal is used. The curves are the results of a ray-tracing simulation assuming a crystal with a 3 arc second (solid line), 4 arc second (long dashes), and a 5 arc second (short dashes) mosaic width.*

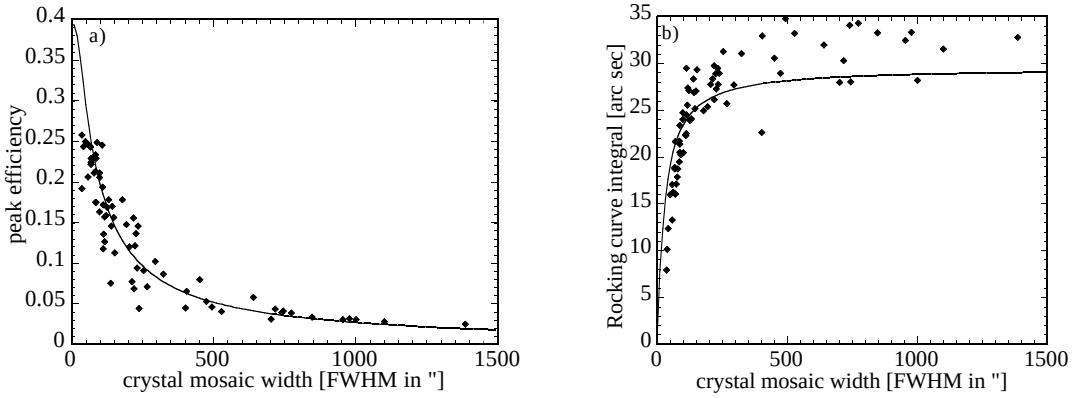

Figure 55: *The peak efficiency (plot a) and the rocking curve integral (plot b) are shown as a function of mosaic width. The data points (filled diamonds) are from 72 rocking curves evenly spaced over the surface of a 2.46-mm-thick Ge (111) crystal after heating and squeezing the crystal. The measurements were done at 200 keV. The solid curves are calculated using the Dawin model.*

along the (111)-planes as the second crystal of a double-crystal monochromator. The first crystal was a 2.88-mm-thick (111) crystal with a mosaic width of a few arc seconds. At 200 keV, 72 rocking curves of the second crystal evenly spaced over the 10×10 mm^2 crystal surface were measured. The synchrotron beam size was 0.4×0.4 mm^2 at the height of the crystal, corresponding to an angular beam divergence of 3 arc seconds. The mosaic width of the rocking curves varied strongly with position, and most of the rocking curves were non-Gaussian. For each curve, the count rate was background-subtracted, normalized to a beam current of 100 mA, and divided by the normalized transmitted flux of the 1st crystal. The rocking curves are thus measured in terms of efficiency. The maximum efficiency, full width at half maximum (FWHM) and the integral of each rocking curve were then determined.

Fig. 55 shows the maximum efficiency (plot a) and the integral (plot b) of the rocking curves as a function of their width. Superimposed on the data are the curves obtained using equations (61) and (62). For the 2.46-mm-thick crystal and (111) diffraction at 200 keV, the constants of equation (61) are $A = 0.393$ and $B = 29.9$. The data follow the Darwin model curve quite well. Fluctuations could be due to the non-Gaussian nature of the curves.

8.3.4 Effect of Surface Damage on the Diffraction Efficiency

The cutting of a crystal induces surface damage which increases the mosaic width. This is generally removed by etching, i.e., chemically removing the crystal surface, as well as by polishing. To determine the effect of the surface damage on the diffraction at energies of several hundred keV, we performed a topograph of a (111) crystal before and after etching. The crystal was mounted as the second crystal of a (111) double crystal monochromator. The first crystal was a 2.88-mm-thick (111) crystal with a mosaic width of a few arc seconds. Both topographs were performed by measuring one hundred rocking curves evenly spaced over the 10×10 mm^2 crystal surface. This was done at 290 keV with a 0.4×0.4 mm^2 beam size. The crystal was etched in a solution of 85% HNO_3 and 15% HF (48% conc.) for 10 minutes. The thickness was 2.84 mm before etching and 2.46 mm after etching. For each curve, the count rate was background-subtracted and normalized to 100 mA beam current. The FWHM and peak count rate were then calculated.

The width as a function of position is shown in Fig. 56 for the unetched crystal, and in Fig. 57 for the etched crystal. For the etched crystal, the point with a width of 9 arc seconds is presumably due to low counting statistics, as most of the beam was not hitting the crystal. The maximal count rate for this scan was only 100 counts, whereas scans in the center of the crystal had a maximum count rate of about 3000 counts. The large widths at the edge of the unetched crystal are real, with the maximum ranging from 1000 to 1500 counts.

The results are summarized in Table 12. Listed are the mean FWHM and the mean peak count rate of the rocking curves. These are listed separately for the 36 rocking curves at the edge of the crystal and the 64 rocking curves of the inner part of the crystal. For the rocking curves at the edge of the crystal, the beam illuminated approximately the first 200 micron at the edge of the crystal. The listed FWHM values are the convolution of the 1st and 2nd crystal widths. However, the differences in the FWHM are only due to the etching. The unetched crystal shows a significant broadening of the rocking curves at the edge of the crystal. This reflects the fact that

the beam passes through more of the damaged part of the crystal. For the etched crystal, there is no broadening at the edge. For the unetched crystal, the curves in the inner part of the crystal are broadenend due to the beam passing through the two damaged surfaces of the crystal. This leads to a mean increase in width of 1.7 arc seconds compared to the etched crystal. The fluctuations of the unetched crystal are larger than for the etched crystal, showing that the surface damage is inhomogeneous.

	$< fwhm >$ [arc sec]	$\sigma_{<fwhm>}$ [arc sec]	$< \dot{N} >$ [Hz]	$\sigma_{<\dot{N}>}$ [Hz]
unetched, excluding edge	7.39	1.23	3371	365
unetched, edge	12.68	3.97	1690	900
etched, excluding edge	5.69	0.21	3171	218
etched, edge	5.75	0.81	703	538

Table 12: *The mean FWHM* $< fwhm >$ *and the mean peak count rate* $< \dot{N} >$ *and the standard deviation* $\sigma_{<fwhm>}$ *and* $\sigma_{<\dot{N}>}$ *of these values are listed for the (111)-crystal before and after etching. The values are listed separately for rocking curves excluding the edge and for rocking curves taken at the edge of the crystal.*

8.3.5 Increase of the Diffraction Efficiency for a Source at Finite Distance due to Crystal Wedging

For the crystal lens tests, the crystals were wedged in order to better match the angular divergence of the source to the crystal mosaic width. Wedging is only necessary when focussing radiation from a source at finite distance.

In order to better understand the effect of the wedging, we measured rocking curves of a wedged crystal using synchrotron radiation. A 10.06-mm-thick (220) first crystal was used to monochromatize the beam, and the wedged crystal was mounted as the second crystal. The diffraction of the wedged crystal was along the (220) planes, whereas when mounted on the lens this crystal would diffract along the (111) planes.

With the wedges more or less coaligned with the y-axis, rocking curves of the wedged crystal were performed in steps of 1 mm in y. An energy spectrum of the transmitted beam of the first crystal was used to determine the absolute efficiency of the rocking curves. The synchrotron beamsize was 0.4×0.4 mm^2. Fig. 58 shows the geometry and two of the rocking curves measured. Rocking curve "1" below the wedged region is flat-topped with a FWHM of 30 arc seconds. Rocking curve "2" shows 3 separate peaks corresponding to the three segments of the crystal. The wedging is not perfect, as the three segments are not equally spaced. The width of these segments decreases from 5 (at the base of the wedges) to 3 arc seconds at the top of the wedges. The separation of

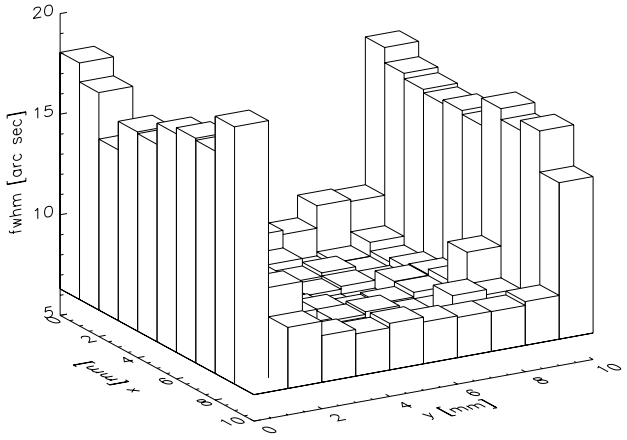

Figure 56: *The FWHM of 100 rocking curves measured over the 10 × 10 mm^2 face of an unetched 3-mm-thick (111) crystal. The measurement was carried out at 290 keV with an 0.4 × 0.4 mm^2 beam size.*

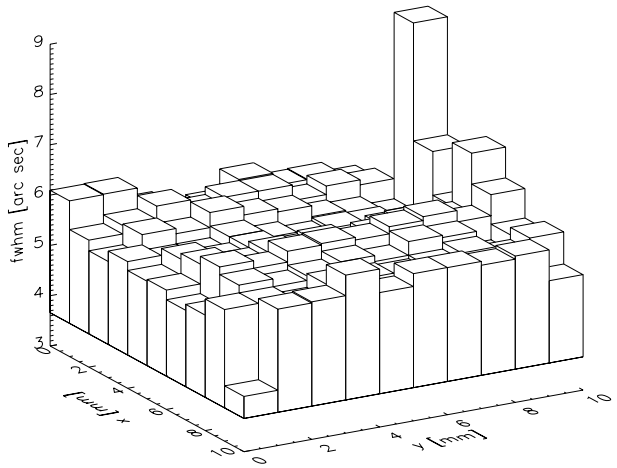

Figure 57: *The FWHM of 100 rocking curves measured over the 10 × 10 mm^2 face of the same crystal as in Fig. 56, but after etching the crystal. Note the difference in y-axis to that of Fig. 56. The measurement was carried out at 290 keV with an 0.4 × 0.4 mm^2 beam size.*

the first two segments is 19 arc seconds, the separation of the second and third is 10 arc seconds, decreasing to 6 arc seconds at the top of the crystal. These rocking curves show that the wedges effectively bend the crystal below the wedged region. The increase in the peak width of the single segments close to the base can be interpreted as strain due to the bending. For the source at 24.75 m, the source subtends an angle of 80 arc seconds over the crystal. Thus, the measured wedging is not optimal, as the bending was only 30 arc seconds wide. This type of bending made a major improvement in the diffraction efficiency of the crystal when used in the crystal lens.

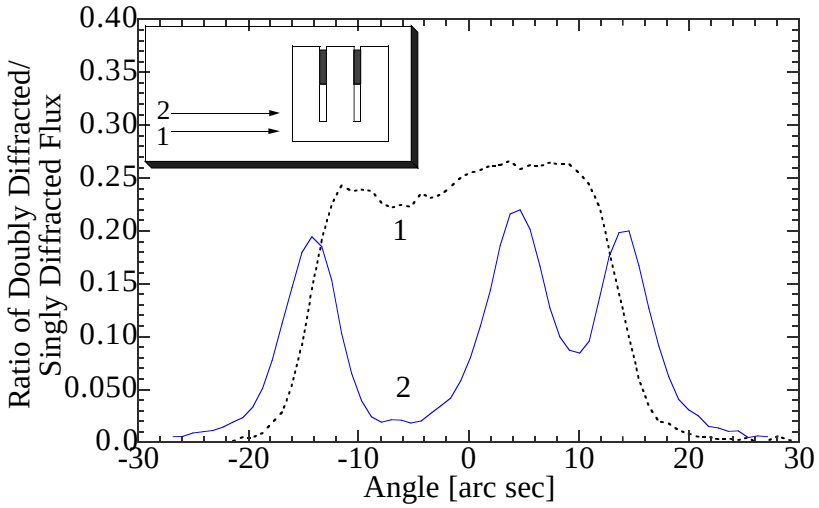

Figure 58: *The figure shows two rocking curves of a wedged crystal measured at 290 keV with synchrotron radiation. The inset shows the geometry of the synchrotron radiation and the wedged crystal, and the points where the two curves were measured. Rocking curve 1 shows a flat-topped curve with a FWHM of 30 arc seconds. Rocking curve 2 shows three distinct segments, with an angular separation of 19 arc seconds and 10 arc seconds respectively.*

8.4 Conclusions

Using synchrotron radiation, it was possible to show that the low diffraction efficiency obtained during the crystal lens tests was due to the mismatch between the large angular divergence of the source over the face of the crystal (80 to 200 arc seconds) and the crystal mosaic width (a few arc seconds), and that much higher efficiencies are obtained for incoming radiation with small angular divergence.

Three different types of efficiency measurements were carried out. A double crystal setup together with an HPGe detector was used to determine the efficiency of the (111) and the (220) planes for energies ranging from 200 to 500 keV. As the mosaic width of the two crystals was comparable, the ratio of the doubly-diffracted to singly-diffracted flux measures the acceptance of the 2nd crystal to those photons diffracted by the first crystal. The peak efficiency for photons with zero

angular divergence can then be determined with a ray-tracing simulation. The mosaic widths of the crystal are determined by the energy widths of the singly-diffracted and doubly-diffracted energy spectrum as well as the rocking curve width. The ratio of the double-diffracted to single-diffracted flux ranged from 20% and 31% for the Ge (111) and (220) planes from 200 keV to 500 keV. The angular divergence was 3 arc seconds at the height of the first crystal. Neglecting the absorption in the crystal, the ratio of the double-diffracted to single-diffracted flux ranges from 31% to 49%. Using a ray-tracing simulation and the Darwin model to calculate the diffraction probability, the peak efficiency of these crystals to monochromatic radiation with no angular divergence would range from 20% to 43% for the energy range of 200 to 500 keV. The second type of efficiency measurement measured the ratio of higher-order to first-order flux using a single crystal directly exposed to the beam together with the HPGe detector. Assuming the incident spectrum is known and neglecting the small beam divergence, these measurements directly determine the flux throughput of the crystal when exposed to a continuum spectrum. The relative efficiencies of 2nd order ((440) plane) and 3rd order ((333) plane) diffraction was measured, with a flux ratio of 2.4 to 2.6 for the (220) to (440) planes over the energy range of 260 to 410 keV, and a flux ratio of 6.9 for the (111) and (333) planes at 290 keV. The large decrease in flux for the higher order planes is due to the narrower energy bandpass of the higher order reflections, as well as a decrease of the peak efficiency.

The third type of efficiency measurement had a first crystal with a mosaic width of a few arc seconds, and a second crystal with a much larger mosaic width. In this measurement, the angular divergence and the energy spread of the photons diffracted by the first crystal can be assumed to be negligeable, and the rocking curve of the second crystal directly measures the efficiency as a function of angle at a fixed (monochromatic) energy. In this measurement, the peak efficiency and the rocking curve integral were measured over a wide range of mosaic widths. The results agree reasonably well with the calculated curves obtained with the Darwin model. These results give credibility to the simulations of the performance of a balloon-borne and a spaceborne crystal lens telescope, which are based on the Darwin model to determine the crystal efficiencies as a function of the angle and energy of the incoming radiation.

The effect of surface damage on the diffraction efficiency was determined by measuring a topograph of the crystal before and after etching. The mean decrease in rocking curve width due to the etching was 1.7 arc seconds in the center of the crystal and 6.9 arc seconds at the crystal edge.

Finally, rocking curves of a wedged crystal were measured using synchrotron radiation, showing that the increase in count rate seen for a source at finite distance is due to both bending and straining of the crystal.

9 Summary

The work presented in this thesis can be divided into three parts. In the first part, the theory of diffraction of mosaic crystals was used to optimize the crystal lens design and to simulate the performance of a crystal lens telescope in space. Based on these calculations, the scientific potential of such an instrument was discussed.
In the second part, one ring of a prototype tunable lens was realized using picomotors and non-contact eddy-current sensors to orient crystals with sub arc second precision. The possibility of changing energies that the lens focuses was demonstrated by focusing line energies ranging from 276 keV to 662 keV.
In the third part, diffraction efficiencies of crystals with a mosaic width of a few arc seconds were measured at energies ranging from 200 keV to 500 keV using synchrotron radiation. At a fixed energy, the peak and the integral efficiency were measured over a large range of mosaic width. The results were compared with the Darwin model used in the simulations described above, and were in reaonably good agreement with the model.
In the following, the results of the three parts of this thesis are summarized:

9.1 Simulations of the Performance of a Crystal Lens Telescope

The basis of the simulation of the performance of a crystal lens telescope is the calculation of the diffraction behaviour of the crystals. In this thesis, the Darwin mosaic model was used to determine the diffraction efficiency of the crystals as a function of their mosaic width, the crystalline material, and the diffraction planes.
Using the Darwin mosaic model, the effect of the crystal lens design (crystal material, number of rings, crystal mosaic width, crystal thickness) on the telescope performance (working energy range, efficiency, energy bandpass) was discussed. For the configuration of the first prototype lens built prior to this thesis, the off-axis and off-energy response, the angular resolution and the focal plane image were discussed.
In view of the characteristics of a crystal lens telescope, the scientific potential of a crystal lens telescope was discussed. Narrow line sensitivities of $2 \cdot 10^{-7}$ ph/cm^2 s to $1 \cdot 10^{-6}$ ph/cm^2 s over the energy range of 200 keV to 1300 keV seem achievable with a lens of moderate size (a lens area of $\approx$ 2500 cm^2). These sensitivies apply to a lens with an energy bandpass of 2.3 keV at 500 keV, and 11.5 keV at 1250 keV, and an effective lens area of 480 cm^2 at 500 keV and 230 cm^2 at 1250 keV. Line sensitivities for slightly broadened lines range from $3 \cdot 10^{-7}$ ph/cm^2 s to $1 \cdot 10^{-6}$ ph/cm^2 s ($\frac{\Delta E}{E} = 0.007$) and from $5 \cdot 10^{-7}$ ph/cm^2 s to $2 \cdot 10^{-6}$ ph/cm^2 s ($\frac{\Delta E}{E} = 0.017$) over the energy range of 200 keV to 1300 keV. Assuming an optically thin expanding envelope, these widths correspond to expansion velocities of $\pm$1000 km/s and $\pm$2500 km/s. The narrow line sensitivities are a factor of 10 to 100 below existing and next-generation spectrometers, and make the detection of several supernovae of type Ia per year and at least one supernova of type Ib/c during a mission lifetime probable.
The angular resolution of a crystal lens telescope is $<$ 1 minute, compared to $>$ 10 arc minute angular resolution of exisiting and next-generation coded aperture mask detectors working at

several hundred keV. An observation of the Galactic microquasar 1E1740-294 with a crystal lens telescope could clarify if this object is contributing to the 511 keV line flux, and could determine if the emission is coming from the jets seen at radio wavelengths. A crystal lens telescope could also map the ^{44}Ti and perhaps the ^{26}Al emission in young supernova remnants.
Using a focal plane detector with good energy resolution would enable the determination of line profiles. This is particularly interesting for supernova and nova lines, where the line profiles could help to clarify the explosion and ejecta dynamics.
Simulations of a first balloon flight of a crystal lens were carried out. For the observation of the Crab pulsar and nebula at 170 keV, a significant detection of the Crab is to be expected even for short-duration flights. For Ge crystals with 30 (60) arc second mosaic width, an atmospheric depth of 5 g cm^{-2} and a geographic latitude of 45°, using a background estimate based on Monte Carlo simulations carried out by Pierre Jean gives a significance of $\sigma = 5.6 \cdot \sqrt{t[h]}$ ($\sigma = 6.8 \cdot \sqrt{t[h]}$) for an active BGO shield and $\sigma = 3.3 \cdot \sqrt{t[h]}$ ($\sigma = 4.2 \cdot \sqrt{t[h]}$) for a passive BGO shield. For Ge crystals with 30 (60) arc second mosaic width, the energy bandpass of the lens is 1 keV (2 keV), the detected flux around culmination is 40 (55) photons/hour. The ratio of source photons to background counts is 6.3 (8.7) assuming an active BGO shield and 0.7 (1.0) assuming a passive BGO shield. The extent of the nebula will be difficult to determine, due to the large mosaic width of the crystals and the additional angular uncertainty arising from the detector energy resolution as well as limited photon statistics. Using crystals with 30 arc sec mosaic width and assuming a detector resolution of 1.5 keV, the angular uncertainty (FWHM) is 80 arc seconds. The effect of the detector resolution decreases with energy, at 511 keV the angular uncertainty would only be 33 arc seconds.

9.2 Realization of One Ring of a Prototype Tunable Lens

The buildup of one ring of a prototype tuneble lens was motivated by the fact that for a spaceborne crystal lens telescope, it is necessary to be able to change the energy that the instrument focuses. This implies being able to change the orientation of the crystals with a precision and longterm stability of a few arc seconds over a range of 0.5° to 1.5°. Also, the detector lens distance needs to be changed for each energy, and scales linearly with energy.
Preliminary tests with two New Focus picomotor models and two different Kaman non-contact sensors using a theodolyte in autocollimation were carried out. The Kaman 2U sensor and the New Focus 8351 picomotors were chosen for the tunable lens. Multiplexers for the sensors and motors as well as a synchronization circuit for the picomotor driver were designed and built to allow individual crystals to be oriented under computer control.
16 (111) crystals, comprising the innermost ring of a crystal lens, were then motorized using the picomotors and sensors. The picomotor pushed on one side of a plate holding the crystal, and the sensor measured the variable distance to this plate. The calibration results were a picomotor resolution of 7 to 30 nm (0.05 to 0.2 arc seconds) and a sensor resolution of 10 to 20 nm (0.1 to 0.2 arc seconds). The sensor range of 0.5° to 1.0° is sufficient for the inner rings. For the outer rings, where a dynamic range of up to 1.5° is required, the Kaman model 5U sensor could be used.
The prototype crystal lens was tested with a 31.2 mC ^{133}Ba source with line energies at 276, 303,

356, and 383 keV, as well as a 90 mC ^{137}Cs source with a line energy of 662 keV. The sources were at 24.75 m and 24.45 m from the lens. The focused flux was measured with a 6-cm-diameter, p-type coaxial HPGe detector. The detector readout, the translation and the rotation of the lens, as well as the orientation of individual crystals was controlled by a 90-MHz Pentium PC. The data acquisition program was written in the National Instruments LabWindows/CVI environment.

Using this system, scans in energy of a spaceborne instrument were simulated. For these scans, the orientation of all of the crystals were changed in small increments, with the detector count rate being determined at each scan point. The lens position was fixed in space, i.e., the optical axis of the system was fixed. The same scans were performed with slightly "detuned" lens crystals, demonstrating the ability to increase the energy bandpass of the instrument.

By rotating the lens frame about 2 axes, scans of a spaceborne instrument mapping the intensity of a slightly extended source were simulated. For these scans, the orientation of the crystals was fixed, and the optical axis of the lens was moved in space.

The capability to focus a range of energies was demonstrated by changing the orientation of all crystals to focus the Ba and Cs source lines at 276, 303, 356, 383, and 662 keV.

The stability of the sensor calibration and the system stability were demonstrated in a number of measurements. The stability of the sensors was tested by reading out all sensor values every 60 s over a time period of 2 d for a fixed position and a temperature stabilized to better than 0.5 degrees. The standard deviation was about 1 arc second for all of the sensors. A linear fit to the sensor values as a function of time shows a long-term drift of 1 arc second per 12-25 hours. Measurements of the optimal orientation for single crystals showed a stability better than a few arc seconds over a period of 10 days. The system stability was also tested by orienting all crystals to alternately focus the 303 keV and the 356 keV line radiation, and verifying that the detector count rate remains stable with time.

Only the innermost ring of the lens was motorized. A possible scheme to mount picomotors and eddy-current sensors for all eight rings of the lens is shown in [93].

The next step towards a spaceborne tunable lens would be to demonstrate the functioning of at least one ring of motorized crystals during a balloon flight. This could be done without major changes to the laboratory prototype.

For a satellite-based crystal lens telescope, the design would need to be optimized in terms of weight and power consumption, and would need to be ruggidized to withstand launch vibrations. The electronics should be modified in order to minimize the time needed to move from one energy to the next. One could envisage a scheme whereby each ring of crystals is moved simultaneously. The travel is different for each ring, and is largest for the outermost ring. Afterwards, each crystal would be fine-positioned using the sensor. Assuming a 2.5 cm lever, a picomotor step size of 15 nm, and a maximum speed of 1000 steps per second, the outermost (440) ring would need 45 s to move from 200 keV to 1300 keV.

Kaman has proposed the development of a "single-chip" sensor, with the coil and signal conditioning electronics mounted on a single ceramic chip of size $12 \times 45 \times 6$ mm^3. The chip would use a 1 MHz clock and a regulated 5 V signal as inputs, outputs would be analog voltages for the distance and for the temperature. This would facilitate the multiplexing of several hundred sensors.

9.3 Diffraction Efficiency Measurements

The diffraction efficiency of the crystals, i.e., the ratio of diffracted to incident photons as a function of photon angle and energy, is decisive for the performance of a crystal lens telescope. The efficiency determines the effective area, the field-of-view, and the off-axis and off-energy response of the crystal lens.

The efficiencies measured during the crystal lens tests were low, ranging from 3% to 6% over the energy range of 303 keV to 662 keV. This was due to the mismatch between the mosaic width of the crystals (a few arc seconds) and the angle that the source subtends over the face of the crystal (80 to 200 arc seconds). To increase the efficiency for a source at finite distance, the crystals were wedged, i.e., two slots were cut into the crystal, and sheets inserted into these slots to bend and strain the crystals. This makes an extrapolation of the results to an astrophysical point source difficult.

In order to overcome these problems, two experiments were carried out at the Advanced Photon Source (APS) Synchrotron at the Argonne National Laboratory sector 1 bending magnet beamline in April/May 1997 and in September 1997.

Synchrotron radiation has major advantages for the determination of diffraction efficiencies and crystal characteristics. The bending magnet synchrotron radiation is a continuum. Using gamma-ray sources, only the efficiency for line radiation can be determined. Due to the high brilliance and high critical energy, a small beam size with small angular divergence can be used for measurements up to gamma-ray energies. The beam size and divergence can be adjusted with slits. Most measurements were made with a beam divergence of 3 arc seconds full width at half maximum (FWHM). Assuming a 4.2×0.6 mm^2 slit at 30 m from the source and 100 mA beam current, the bending magnet flux is $1.2 \cdot 10^8$ ph/(s 0.1%bw) at 200 keV, falling off by approximately two orders of magnitude per 100 keV increase in energy.

The efficiency measurements were carried out using a double crystal monochromator and an HPGe detector. The width of the energy spectrum of the singly-diffracted and doubly-diffracted flux and a rocking curve of the second crystal were obtained at each energy. As the mosaic width of the two crystals was comparable, the ratio of the doubly-diffracted to singly-diffracted flux measures the acceptance of the 2nd crystal to those photons diffracted by the first crystal. The peak efficiency for photons with zero angular divergence can then be determined with a ray-tracing simulation. The mosaic widths of the crystal are determined by the energy widths of the singly-diffracted and doubly-diffracted energy spectrum. The rocking curve width is the convolution of the beam divergence and the mosaic width of both crystals, and thus provides redundant information.

The ratio of the double-diffracted to single-diffracted flux ranged from 20% and 31% for the Ge (111) and (220) planes from 200 keV to 500 keV. The angular divergence was 3 arc seconds at the height of the first crystal. Neglecting the absorption in the crystal, the ratio of the double-diffracted to single-diffracted flux ranges from 31% to 49%. A ray-tracing Monte Carlo program using the Darwin mosaic model to calculate the diffraction probability was developped. It was possible to simulate the measured efficiencies with reasonable agreement with the data. The simulation gives a peak efficiency of these crystals to monochromatic radiation with no angular divergence ranging from 20% to 43% for the energy range of 200 to 500 keV.

Relative efficiencies of second and third order diffraction compared to first order diffraction were measured using a crystal that was directly exposed to the beam and comparing the flux measured with the HPGe detector. Assuming the incident spectrum is known and neglecting the small beam divergence, these measurements directly determine the flux throughput of the crystal when exposed to a continuum spectrum from an astrophysical point source. The relative efficiencies of second order ((440) plane) to first order ((220) plane) diffraction was 2.4 to 2.6 over the energy range of 260 keV to 410 keV. The relative efficiencies of third order ((333) plane) to first order ((111) plane) diffraction was 6.9 at 410 keV. The large decrease in flux for the higher order planes is due to the narrower energy bandpass of the higher order reflections, as well as a decrease of the peak efficiency. For monochromatic incident radiation, the flux decrease is smaller, as the diffracted flux is independent of the energy bandpass.

Efficiencies were also measured over a wide range of mosaic width by measuring 72 rocking curves evenly spaced over the face of a 10×10 mm^2 crystal which had been heated and squeezed to increase the mosaic width. The beamsize was 0.4×0.4 mm^2. The measurement was performed with a double crystal setup, with a first crystal with a few arc seconds mosaic width. The mosaic width of the sample, mounted as the second crystal, varied as a function of position, and the rocking curves were mostly non-Gaussian. As the mosaic width of the sample was for the most part much larger than the mosaic width of the first crystal, the angular divergence and the energy spread of the photons diffracted by the first crystal can be assumed to be negligeable, and the rocking curve of the second crystal directly measures the efficiency as a function of angle at a fixed (monochromatic) energy. The data was used to determine the peak efficiency and the integrated efficiciency as a function of mosaic width. The peak efficiency decreases with increasing width, whereas the integrated efficiency increases with increasing mosaic width. The data points agree reasonably well with the curves calculated using the Darwin mosaic model. These results give credibility to the simulations of the performance of a balloon-borne and a spaceborne crystal lens telescope, which are based on the Darwin model to determine the crystal efficiencies as a function of the angle and energy of the incoming radiation.

Rocking curves of a wedged crystal were measured using synchrotron radiation, showing that the increase in count rate seen for a source at finite distance is due to both bending and straining of the crystal.

In summary, the synchrotron measurements demonstrated that high diffraction efficiencies can be obtained for incident radiation with low angular divergence. The results confirm the Darwin model as a basis for calculations of the performance of a crystal lens telescope.

10 Bibliography

References

[1] B.L.Brown and M.Leventhal, ApJ, 319, 637 (1987)

[2] N.Prantzos, A & A Suppl. Series, 120, 303 (1996)

[3] P.V. Ramana Murphy and A.W. Wolfendale, "Gamma-Ray Astronomy", Cambridge University Press, 1986, p.4

[4] L.Bouchet et al., ApJ, 383, L45 (1991)

[5] G.V.Jung et al, A & A, 295, 2, L23 (1995)

[6] D.M.Smith et al., ApJ, 414, 165 (1993)

[7] B.Cordier et al., A & A, 275, L1 (1993)

[8] A.Goldwurm, ApJ, 389, L79 (1992)

[9] E.Massaro, G.Matt, M.Salvati, E.Costa, P.Mandrou, M.Niel, J.F.Olive, T.Mineo, B.Sacco, L.Scarsi, G.Gerardi, B.Agrinier, E.Barouch, R.Comte, B.Parlier, J.L.Masnou, ApJ, 376, L11, (1991)

[10] R.L.Kinzer, W.R.Purcell, W.N.Johnson, J.D.Kurfess, G.Jung and J.Skibo A & A Suppl. Series, 120, 317 (1996)

[11] W.N.Johnson, F.R.Harnden and R.C.Haymes, ApJ, 172, L1 (1972)

[12] W.N.Johnson and R.C.Haymes, ApJ, 184, 103 (1973)

[13] R.C.Haymes, G.D.Walraven, C.A.Meegan, R.D.Hall, F.T.Djuth, D.H.Shelton, ApJ, 201, 593 (1975)

[14] M.Leventhal, C.J.MacCallum, P.D.Stang, ApJ, 225, L11 (1978)

[15] B.J.Teegarden Proc. "The Gamma Ray Sky with Compton GRO and SIGMA", Kluwer Press, 1995, p.255

[16] R.E.Lingenfelter and R.Ramaty, ApJ, 343, 686 (1989)

[17] W.R.Purcell et al., ApJ, 491, 725 (1997)

[18] W.Mahoney, J.Ling, A.Jacobsen and R.Lingenfelter, ApJ, 262, 742 (1982)

[19] J.Tueller, Proc. "Gamma-Ray Line Astrophysics", Editors P.Durouchoux, N.Prantzos, AIP Press, 1991, p.199

[20] J.Tueller et al., ApJ, 351, L41 (1990)

[21] J.D.Kurfess et al., ApJ, 399, L137 (1992)

[22] M.D.Leising et al., ApJ, 450, 805 (1995)

[23] G.G.Lichti et al., A&A 292, 569 (1994)

[24] D.J.Morris et al., Proc. "17th Texas Symposium on Relativistic Astrophyics" 396, (1995)

[25] S.M.Matz, G.H.Share, M.D.Leising, E.L.Chupp, W.T.Vestrand, W.R.Purcell, M.S.Strickman and C.Reppin, Nature, 331, 416 (1988)

[26] A.F.Iyudin et al., A & A, 284, L1 (1994)

[27] A.F.Iyudin et al., Proc. "2nd INTEGRAL Workshop", Sept. 17-20th 1996, St. Malo, France, 37

[28] E.B.Norman, E.Browne, Y.D.Chan, I.D.Goldman, R.M.Larimer, K.T.Lesko, M.Nelson, F.E.Wietfeldt, and I.Zlimen, Nucl. Phys. A, 621, 92 (1997)

[29] H.Bloemen et al., ApJ, L475, 25 (1997)

[30] R.J.Murphy et al., ApJ, 358, 298 (1990)

[31] W.A.Mahoney, J.C.Ling, A.S.Jacobson, R.E.Lingenfelter, ApJ, 262, 742 (1982)

[32] W.A.Mahoney, J.C.Ling, W.A.Wheaton and A.S.Jacobson, ApJ, 286, 578 (1984)

[33] P.von Ballmoos, R.Diehl and V.Schoenfelder, ApJ, 318, 654 (1987)

[34] R.Diehl et al., A & A, 298, 445 (1995)

[35] U.Oberlack et al., A & A Suppl. Series, 120, 311 (1996)

[36] R.Diehl et al., A & A, 298, L25 (1995)

[37] J.Knödlseder, PhD thesis, Université Paul Sabatier de Toulouse (1997)

[38] J.E.Naya, S.D.Barthelmy, L.M.Bartlett, N.Gehrels, M.Leventhal, A.Parsons, B.J.Teegarden and J.Tueller, Nature, 384, 44 (1996)

[39] W.A.Mahoney, J.C.Ling, W.A.Wheaton, A.S.Jacobson, ApJ, 286, 578 (1984)

[40] J.Trümper, W.Pietsch, C.Reppin, W.Voges, R.Staubert and E.Kendziorra, ApJ, 219, L105 (1978)

[41] T.Mihara et al., Nature, 346, 250 (1990)

[42] A.Parmar, Proc. "The Evolution of X-ray Binaries", College Park MD 1993, Edt. S.S.Holt and C.S.Day AIP Press, p.415 (1994)

[43] A.Yoshida, T.Murakami, J.Nishimura, I.Kondo, E.E.Fenimore, Proc. Los Alamos Worshop on Gamma-Ray Bursts, Taos, New Mexico, July 29-August 3 1990 Editors C.Ho, R.I.Epstein, E.E.Fenimore, Cambridge University Press, 1992, p.399

[44] A.Yoshida, T.Murakami, J.Nishimura, I.Kondo, E.E.Fenimore, Proc. "Los Alamos Worshop on Gamma-Ray Bursts", Taos, New Mexico, July 29-August 3 1990 Editors C.Ho, R.I.Epstein, E.E.Fenimore, Cambridge University Press, 1992, p.443

[45] D.M.Palmer, B.J.Teegarden, B.E.Schaefer et al., ApJ, 433, L77 (1994)

[46] D.L.Band, L.A.Ford, J.L.Matteson et al., ApJ, 485, 747 (1997)

[47] M.S.Briggs, D.L.Band, R.D.Preece, G.N.Pendleton, W.S.Paciesas and J.L.Matteson, to appear in the "4th Huntsville Symposium", ed. C.Meegan, R.Preece, and T.Koshut

[48] K.C.Sahu et al., Nature, 387, 476 (1997)

[49] P.Meszaros and M.Rees, ApJ, 476, 232 (1997)

[50] E.Koch, "Handbook on Synchrotron Radiation", Volume 1A, North-Holland Publishing Company 1983

[51] B.D.Ramsey, R.A.Austin, R.Decher, Space Science Reviews, 69, 139 (1994)

[52] J.K.Davies, "Astronomy fron Space", Wiley & Sons Ltd., 1997

[53] D.H.Bilderback, B.M.Lairson, T.W.Barbee, G.E.Ice, and C.J.Sparks Jr., NIMA, 208, 251 (1983)

[54] B.E.Warren, "X-ray Diffraction", Dover Pub., 1990, p.253

[55] P.Gorenstein and K.Joensen, Exp. Astronomy, 6, 109, (1995)

[56] K.Tamura et al., Proc. SPIE, 3113, 285 (1997)

[57] K.D.Joensen et al., Proc. SPIE, 1736, 239 (1992)

[58] F.Frontera and G.Pareschi, Exp. Astronomy, 6, 25 (1995)

[59] P.Jean, A & A Suppl. Series, 120, 673 (1996)

[60] E.Aprile et al., SPIE Proc., 2806, 341 (1996)

[61] A.Zych et al., Proc. "2nd INTEGRAL Workshop" St. Malo France Sept. 16-20 1996 p.367

[62] T.J.O'Neill et al.,A & A Suppl. Series, 120, 673 (1996)

[63] W.N.Johnson, C.Dermer, R.A. Kroeger, J.D.Kurfess, N.Gehrels, J.Grindlay, M.D.Leising, T.Prince, W.Purcell, J.Ryan, and T.Tumer, Proc. SPIE, 2518, 74, (1995)

[64] E.Caroli, J.B.Stephen, G.Di Cocco, L.Natalucci, and A.Spizzichino, Space Science Reviews, 45, 349 (1987)

[65] E.E.Fenimore, Applied Optics, 17, 3562 (1978)

[66] A.P.Willmore, G.K.Skinner, C.J.Eyles, and B.R.Ramsey, NIMA, 221, 284 (1984)

[67] J.Paul et al., Adv. Space Res. 11, 8, 289 (1991)

[68] B.J.Teegarden et al., Proc "2nd INTEGRAL Workshop", 16-20 Sept. 1996, 495

[69] T.O.Tümer et al., Proc "2nd INTEGRAL Workshop", 16-20 Sept. 1996, 361

[70] P.Ubertini et al., Proc "2nd INTEGRAL Workshop", 16-20 Sept. 1996, 599

[71] P.Mandrou et al., Proc "2nd INTEGRAL Workshop", 16-20 Sept. 1996, 591

[72] N.Gehrels, E.Chipman and D.A.Kniffen, A & A Suppl. Series, 97, 5 (1993)

[73] P.F.Michelson et al., Proc. SPIE, 2806, 31 (1996)

[74] J.E.Naya, P.Jean, P.von Ballmoos, F.Albernhe, J.Bockholt, Experimental Astronomy, 6, 357 (1995)

[75] P.Jean, J.E.Naya, J.F.Olive, P.von Ballmoos, A & A Suppl. Series, 120, 673 (1996)

[76] N.Gehrels, C.J.Crannell, D.J.Forrest, R.P.Lin, L.E. Orwig, R. Starr, Solar Physics, 118, 233 (1988)

[77] B.E.Warren, "X-Ray Diffraction", Dover Publications, 1990, p.329

[78] C.G.Darwin, Phil. Mag, 27, 315 (1914)
C.G.Darwin, Phil. Mag, 27, 657 (1914)

[79] W.H. Zachariasen, "Theory of X-Ray Diffraction in Crystals", Wiley & Sons, 1946

[80] J.R. Schneider, Acta. Cryst., A33, 235 (1977)

[81] K. Kleinknecht, "Detectors for Particle Radiation", Cambridge University Press, 1986

[82] International Tables for X-Ray Crystallography, Vol III, 1962

[83] C. Kittel, "Introduction to Solid State Physics", Wiley & Sons, Inc., 1986, p.45

[84] A. Freund, A. Munkholm, S. Brennan, SPIE Proc., 2856, 68 (1992)

[85] A. Freund, A. Munkholm, S.R. Stock, Z.U. Rek, SPIE Proc., 3151 (1997)

[86] S.Keitel, C.C.Retsch, T.Niemoeller, J.R.Schneider, N.V.Abrosimov, S.N.Rossolenko, and H.Riemann, NIMA, in press

[87] J.R. Schneider, H. Nagasawa, L.E. Berman, J.B. Hastings, D.P. Siddons, W. Zulehner, NIMA, 276, 636 (1989)

[88] J.R. Schneider, J. Appl. Cryst., 8, 195 (1975)

[89] R. Staubert, "19th Intl. Cosmic Ray Conf.", 3, 477 (1985)

[90] R.K.Smither, P.B.Fernandez, T.Graber, P.von Ballmoos, J.Naya, F.Albernhe, G.Vedrenne, Experimental Astronomy, 6, 47 (1995)

[91] J.E.Naya, P.von Ballmoos, F.Albernhe, G.Vedrenne, R.K.Smither, M.Faiz, P.B.Fernandez, T.Graber, Proc. "Imaging in High Energy Astronomy", 313 (1995)

[92] J.E.Naya, P.von Ballmoos, R.K.Smither, M.Faiz, P.B.Fernandez, T.Graber, F.Albernhe, G.Vedrenne NIMA, 373, 159 (1996)

[93] R.K.Smither, P.B.Fernandez, T.Graber, P.von Ballmoos, J.E.Naya, F.Albernhe, G.Vedrenne, M.Faiz, Proc. SPIE 96, 2806, 509 (1996)

[94] N.Lund, Experimental Astronomy, 2, 259 (1992)

[95] S.Melone, O.Francescangeli, R.Caciuffo, Rev.Sci.Instrum., 64, 3467 (1993)

[96] F.X.Timmes and S.E.Woosley, ApJ, 489, 160 (1997)

[97] J.Gomez-Gomar, J.Isern and P.Jean, MNRAS, Vol. 295, No.1, p.1 (1998)

[98] M.Della Valle and M.Livie, A & A, 286, 786 (1994)

[99] J.C. Higden and W.A. Fowler, ApJ, 317, 710 (1987)

[100] K.Hatano, D.Branch, A.Fisher and S.Starrfield, MNRAS, 290, 113 (1997)

[101] P.Jean, manuscript in preparation

[102] I.F.Mirabel, L.F.Rodriguez, B.Cordier, J.Paul and F.Lebrun, Nature, 358, 215 (1992)

[103] I.F.Mirabel, ApJ Suppl. Series, 92, 369 (1994)

[104] R.Ramaty, M.Leventhal, K.W.Chan and R.E.Lingenfelter, ApJ, 392, L63 (1992)

[105] E.Churazov, M.Gilfanov, and R.Sunyaev, ApJ, 464, L71 (1996)

[106] F.Lei, J.Dean, and G.L.Hills, Space Science Reviews, 82, 309 (1997)

[107] P.De Chiara and F.Frontera, Applied Optics, Vol. 31, No. 10, 1361 (1992)

[108] F.Frontera, P.De Chiara, G.Pareschi and G.Pasqualini, Proc. SPIE, 2283, 85 (1994)

[109] E.Aprile, A.Bolotnikov, D.Chen, R.Mukherjee, and F.Xu, ApJ Suppl. Series, 92, 689 (1994)

[110] K.R.Lang, "Astrophysical Formulae", Springer-Verlag, 1980

[111] L.M.Bartlett, PhD thesis, University of Maryland College Park (1994)

[112] A.F.Iyudin et al.,Proc. "2nd Integral Workshop", St-Malo, France, 16-20 Sept. 1996

[113] J.E. Naya Ariste, Dissertation, Universite Paul Sabatier de Toulouse, France (1995)

[114] B.Aschenbach, Zeiss Info, Jenaer Rundschau, 1, 6 (1992)

[115] W.Ku et al., ApJ, 204, L77 (1976)

[116] R.M.Pelling et al., ApJ, 319, 416 (1987)

[117] B.Aschenbach and W.Brinkmann, A & A, 41, 147 (1975)

[118] P.von Ballmoos and R.K.Smither, ApJ Suppl. Series, 92, 663 (1994)

[119] P.von Ballmoos, J.E.Naya, F.Albernhe, G.Vedrenne, R.K.Smither, M.Faiz, P.B.Fernandez, T.Graber, proc. "Imaging in High Energy Astronomy", 1995, p.239

[120] Technical Bulletin ANL/APS/TB-26, "The Advanced Photon Source List of Parameters", compiled by H.M.Bizek (July 1996)

11 Acknowledgements

First and foremost, I would like to thank my thesis advisor Peter von Ballmoos for the interesting thesis topic, and for helping me throughout my thesis.
I also want to thank Robert Smither for his interest in my work, his ideas, many useful discussions, and his enthusiasm during my stay at APS.
I thank Tim Graber for helping me to get my feet on the ground in the US and for his help in all aspects of the crystal lens project and the synchrotron tests.
I thank Dennis Mills for his interest in the crystal lens project and for making the synchrotron experiments at APS possible.
I wish to thank all of the sector 1 personnel, without which it would not have been possible to carry out the synchrotron experiments, in particular George Srajer, Jonathan Lang, Dean Haeffner, Sarvjit Shastri, Bill McHargue and Mark Keefe. I thank Dennis Mills, Shawn Rogers and Lahsen Assoufid for their help during the synchrotron experiments.
I also thank Dennis Mills and the rest of the High Heat Load Optics group for making my stay at the APS so enjoyable, and for their support.
I thank Al Paugys for his technical support throughout my stay at APS, for building the rail system to move the detector for the crystal lens tests, and for help during the synchrotron experiment. I thank Tim Mooney for his help with EPICS, for being willing to help at all hours of the day. I thank Patricia Fernandez for her help with the anticoincidence shield and her help during the synchrotron runs. I thank Pam Dalman for her competence and professionalism in organizing my stay at APS. I thank Ruben Khachatryan and Ron Hopf for their help with crystal etching, and Frank Bittles at the APS Optics Shop. Also, I thank the Central Shops personnel for their friendliness and their efficiency. I thank Doug Horan for his help with the broadband rf-amplifier. I thank Frank Bromwell at IPNS for being so supportive of the crystal lens project. I thank Karl Rehm, Irshad Ahmad, John Schiffer, and Boris Harss at the ANL Physics Division for making it possible to neutron-irradiate crystals.
At the CESR, I thank Jean-Francois Olive, Juergen Knoedlseder, Philippe Laporte, and Pierre Jean for their help and for useful discussions. I also thank Eliane Delmas, Monique Meric, Pascale Ramon, Dorine Roma, Annie Liaut, Anne-Marie Moly and Marie-Claude Cathala for their administrative support.
I thank Jean-Francois Olive and Juergen Knoedlseder for proof-reading the manuscript of this thesis, and for their helpful comments and ideas. I thank Gerry Skinner, Pierre Bastie, and Paul Siffert for being willing to be rapporteurs of this work.
I thank the CNES for their financial support of this work and of the crystal lens project.
Finally, and most importantly, I thank my family for their encouragement and their caring support throughout my thesis.